Dissipation in superconducting quantum circuits

Karthik Srikanth Bharadwaj

THÈSE

Pour obtenir le grade de

DOCTEUR DE L'UNIVERSITÉ GRENOBLE ALPES

Spécialité : Physique de la Matière Condensée et du Rayonnement

Arrêté ministériel : 25 mai 2016

Présentée par

KARTHIK SRIKANTH BHARADWAJ

Thèse dirigée par **Wiebke GUICHARD**, Université Grenoble Alpes

préparée au sein du **Laboratoire Institut Néel**
dans **l'École Doctorale Physique**

Dissipation dans les circuits quantiques supraconducteurs

Dissipation in superconducting quantum circuits

Thèse soutenue publiquement le **11 octobre 2021**,
devant le jury composé de :

Monsieur MARCO APRILI
DIRECTEUR DE RECHERCHE, CNRS DELEGATION ILE-DE-FRANCE SUD, Rapporteur
Monsieur IOAN MIHAI POP
PROFESSEUR ASSOCIE, Karlsruhe Institut für Technologie, Rapporteur
Monsieur DAVID B HAVILAND
PROFESSEUR, KTH Royal Institute of Technology, Examinateur
Madame FLORENCE LEVY-BERTRAND
CHARGE DE RECHERCHE, CNRS DELEGATION ALPES, Examinatrice
Monsieur LAURENT SAMINADAYAR
PROFESSEUR DES UNIVERSITES, UNIVERSITE GRENOBLE ALPES, Président

To the sculptor of my life

Ma

Acknowledgment

Having spent more than three years at Neel Institute as a PhD student, I have received a lot of guidance and coaching from many people. I wish to take this opportunity to thank each one of them. This manuscript is an outcome of my PhD work done at QUANTECA group at Centre national de la recherche scientifique in Grenoble France surrounded by amazing researchers and technicians and I am lucky to be a PhD student in this organization.

Firstly, I wish to thank my supervisor Wiebke-Hasch Guichard wholeheartedly for her encouragement throughout the PhD. She has guided me in right direction even during her difficult times. I deeply admire her for her dedication.

Secondly, I would like to acknowledge the help of my Co-supervisor Olivier Buisson who was also my Masters internship supervisor and an extraordinary researcher who gave me his full support all the time. During any technical difficulties he was happy to help me. I thank Nicolas Roch who was an inspiration during my Masters and also during my PhD. He taught me quantum engineering and inspired me to pursue this research topic. I thank Farshad Foroughi who helped me to conduct research independently by teaching me the research work during my initial endeavours and gave me moral support during hard times of my PhD. I thank Cecile Naud for helping me whenever it was possible.

I would also take this chance to thank European Union's Horizon 2020 research and innovation programme under the Marie Sklodowska-Curie grant agreement No 754303 for providing my PhD grant. My greatest thanks goes to Florence Pois a wonderful person with a dedicated mindset who took care of all my administration procedure and was very helpful throughout my stay in Grenoble reducing any burden of bureaucratic complications.

I would like to extend my thanks to the members of the thesis committee: Dr. Marco Aprili and Prof. Ioan Mihai Pop for accepting being the rapporteurs and providing all the encouraging words to defend this thesis successfully. I thank Prof. David B. Haviland and Dr. Florence Levy-Bertrand for being examinateurs of my thesis. I also thank Prof. Laurent Saminadayar for accepting to be in the committee in such short notice and to be the president of the Jury.

I thank Bruno Fernandez, Theirry Crozes, Latifa Abbassi and Gwénaëlle Julie from the Nanofab team and Nora Dempsey and Thibaut Devillers from Micro and nanomagnetism group, from the bottom of my heart for helping and teaching me each step of fabrication process without any hindrance. I also thank André Dias for teaching the Sputtering process and all the fruitful discussions we had. I thank the collaborators Eduard Driessen

and Arnaud Barbier for providing the thick film samples. It would have been very difficult to realize the samples without their support. I thank again Florence Levy-Bertrand for patiently guiding me on theoretical understanding of the electrodynamics of superconductors.

And it's never a good place to work without good colleagues. I had the opportunity to share the work space with very funny and friendly people like Sebastian Leger, Luca Planat, Remy Dassonnville, Vladimir. I also like to thank my other labmates Jovian Delaforce, Arpit Ranadive, Martina Esposito, Thibault Charpentier, Dorian and others for all the good times we spent in our labs and coffee place. I wish them all the best for their future. I thank my best friend AnnaLisa for her moral support during my PhD. I thank all the people who have worked directly or indirectly in making the life and research easier for the PhD students.

Finally I thank my mother for investing her most precious resources on me and my education and for always providing the support and the advice I needed.

Contents

Glossary

Abbreviation or acronym	Definition
AC	Alternating current
ADC	Analog to Digital Converter
AFM	Atomic Force Microscopy
AWG	Arbitrary Waveform Generator
BCS	Bardeen-Cooper-Schrieffer
CPMG	Carr-Purcell-Meiboom-Gill
DAC	Data Acquisition Card
DC	Direct current
DI	Deionized
DOS	Density of states
DPEL	Densely packed energy levels
EM	Electromagnetic
EDX	Energy-Dispersive X-ray
FWHM	Full Width at Half Maximum
GDS	Graphic Design System
HEMT	High Electron Mobility Transistor
HFSS	High-Frequency Structure Simulator
HMDS	Hexamethyldisilazane
ICP	Inductively Coupled Plasma
IF	Intermediate Frequency
IPA	Isopropanol
IV	current-voltage
JJ	Josephson Junction
LO	Local Oscillator
LOR	Lift-off resist
LPF	Low Pass Filter
MIBK	Methyl Isobutyl Ketone
KID	Kinetic Inductance Detectors
MAA	Methacrylic acid
NMP	N-Methyl-2-pyrrolidone
PCB	Printed Circuit Board
PMMA	Poly(methyl methacrylate)
PPMS	Physical property measurement system
PVD	Physical Vapor Deposition

Q	Quality factor
QND	Quantum Non-Demolition
RBS	Detergent
RF	Radio Frequency
RIE	Reactive Ion Etching
RRR	Residual Resistance Ratio
S1818	Photoresist
SEM	Scanning Electron Microscopy
SNR	Signal to Noise Ratio
TLS	Two Level Systems
VNA	Vector Network Analyzer

List of Figures

List of Tables

Chapter 1

Introduction

In classical computers, information is carried by electrical signals of high or low voltage representing 1 or 0 bit. In quantum computers the carrier of information is the energy and phase of a particle in the two distinguishable quantum state called the qubit. These computers have various sources of noise which result in errors. In classical computers, the error probability is 10^{-25} per bit per second. In quantum computers these error rates are as high as 10^{-3} at the present. With such high error rates quantum computation at large scale is impossible. Hence, it is important for engineers and physicists to strive to work towards improving the quantum system properties.
We live in an era where individual quantum systems are controlled. This is also known as the era of second quantum revolution. Presently, quantum systems can be realized by different technologies. The qubits made from NV centers [2] or molecules or ion traps [3] can provide long time of few seconds to few tens of minutes for storage of quantum information which is called the coherence time. However, these qubits couple weakly to the environment and to other qubits making them hard to manipulate to perform operations. Superconducting qubits on the other hand are easy to manipulate even though there coherence time are currently not very long. Hence, the superconducting qubits are at the forefront of the second quantum revolution. In order to improve their coherence time further, one needs to study their limiting factors.
My PhD research activity concentrates on understanding losses in superconducting quantum systems. In particular, two paths were followed. Firstly, I studied the losses in superconducting resonators. Secondly, I studied the losses in a superconducting qubit called the Fluxonium.

1.1 Motivation

In this blooming era of quantum technologies, work done to date by groups around the world has shown that microwave superconducting circuits demonstrate a wide area of applications. It covers the domains such as astronomy, superconducting cavities, resonators, amplifiers and qubits. Below are some details on these applications, and the reason to study loss in these circuits.
1. In Astronomy, photons from cosmic sources are detected using superconducting resonators called the Kinetic Inductance Detectors (KIDs) [4][5][6]. The energy of cosmic

rays breaks the Cooper pairs in a superconductor into quasiparticles. Inductance hence increases with increasing quasiparticle density, causing a change in resonant frequency of KIDs. High quality factor (low loss) KIDs are required to detect any small shifts in frequency.
2. In superconducting cavities, the photons are stored for long time inside a 3D geometry. The large volume helps in enhanced storage of the photons. However, the dissipation in the cavity needs to be reduced to store the photon for longer time [7]. The cavities are also used in classical limit where they are used in particle accelerators to generate fields to accelerate and deflect charged particles. These accelerators need large amplitude of fields. One needs very high quality factor cavities to avoid loss of energy in such cavities [8].
3. In superconducting qubits, the quantum nature of the superconducting circuit elements are exploited to obtain a qubit. The losses in such elements needs to be reduced to achieve long lifetime of the qubit [9][10].
4. In superconducting resonators, low loss or high quality factor resonators can be used as narrow bandwidth filters. These are also called as Purcell filters [11][12]. High quality factor resonant filters reduces unwanted coupling of qubits to the environment.
5. In quantum noise limit amplifiers, nonlinear superconducting circuits can amplify a low amplitude signal with large gain in the quantum noise limit [13][14]. In order to improve the noise properties of such amplifier the lossy medium which increases fluctuation needs to studied.

1.2 Overview: Superconductivity for quantum systems

A small overview of superconductivity is necessary to see the evolution of quantum technologies with superconductors. Since the discovery of superconductors in 1911 by H. Kamerlingh Onnes there has been a lot of progress in the field of superconductivity. More than two decades later, in 1935, London brothers explained the phenomenological theory of superconductivity as a macroscopic quantum phenomena [15].
It was in 1950, the Ginzburg–Landau theory [16] used a macroscopic wavefunction to describe the superconductors. The macroscopic wavefunction for a superconductor is a complex number Ψ, defined by the superconducting gap Δ and a phase ϕ_S such that $\Psi = \Delta e^{i\phi_S}$.
In 1957, a mean field microscopic theory of superconductivity was proposed by Bardeen, Cooper and Schrieffer [17] using which the electrodynamics in superconducting electrodes were studied [18] a year later by Mattis and Bardeen. In 1962 B.D.Josephson predicted the effects of superconductive tunneling of Cooper pairs across a junction[19] which was realized a year later by P.W.Anderson and J.M.Rowell [20].

Such junction which is named Josephson junction is realized by sandwiching an oxide layer between two superconducting electrodes. In such junctions, when there is a phase difference ϕ between the macroscopic wavefunctions of the two electrodes, the current flowing through the junction is given by:

$$I = I_C sin\phi \tag{1.1}$$

where I_C is the critical current which is the maximum current flowing through the junction without any voltage drop across the junction. The second effect predicted by Josephson was the relationship between voltage drop across junction and the phase difference:

$$V = \frac{\Phi_0}{2\pi}\frac{d\phi}{dt} \tag{1.2}$$

where $\Phi_0 = h/2e$ is the quantum of flux where h is the Planck constant and e is the electron charge.

Solid state quantum computing owes a debt of gratitude to the single most important unit which started the quantum computing revolution, "the Josephson junction," since it forms the primary circuit element of the present day superconducting qubits. This is because of the nonlinear superconducting current which is required for qubit operation.

From the above Equations 1.1 and 1.2, energy stored in a Josephson junction is obtained to be $E_J(1 - cos\phi)$ where $E_J = \Phi_0 I_C$. Since the junction has an oxide in between the electrodes, a self capacitance C_J can be assigned to the junction whose energy is given as E_C. These two energy scales define the properties of the superconducting qubits.

The first qubit was realized by a "Cooper pair box" with two Josephson junction in a loop[21]. By increasing the E_J/E_C ratio of such qubits, the charge noise in the qubit was reduced and it was named as phase qubit [22][23]. In order to change the mentioned ratio while keeping the junction size small, a capacitor is added in parallel to the junction to reduce E_C leading to the qubit named "Transmon"[24]. The other flavor of superconducting qubit arise from considering inductance in parallel with the Josephson junction. These qubits are called the "Flux"[25] and "Fluxonium"[26] qubit depending on the inductive energy.

The study of losses originating due to the electrodynamics and other losses in quantum systems including surface effects is carried out in the first part of the thesis. This is studied in the context of Aluminum resonators. In this second part, more details on the Fluxonium qubit and the loss in such architecture is given.

1.3 Dissipation and dephasing

It is important to understand intuitively the dissipation and decoherence in quantum circuits before a detailed study is done. The origin of study of dissipation and dephasing started with the study of internal dynamics at a microscopic scale of nuclear magnetic resonance. Here, the spin dynamics of the nuclear spin magnetic moments in presence of magnetic materials or external field were studied. F.Bloch, first tried to explain such behaviour of nuclear induction in the year 1946[27]. There he studied the relaxation mechanisms of magnetic moments. The characteristic time taken for the polarized nuclear spin to reach its equilibrium state was called the longitudinal relaxation time T_1. The loss of polarization of spin due to inhomogeneities in the transverse polarizing field without loss of its energy was called the transverse relaxation time T_2.
Over the years, this theory was refined such that the loss of polarization also was dependent on relaxation time hence the polarization loss without loss of energy was termed dephasing time T_ϕ such that [28]:

$$\frac{1}{T_2} = \frac{1}{2T_1} + \frac{1}{T_\phi} \tag{1.3}$$

For the qubits, the spin polarization can be replaced by the excitation of the qubit from the ground to the excited state. The dissipation in a qubit or a resonator can be understood in terms of two level systems(TLS) coupled to a bath of densely packed fluctuating energy levels. This is represented in Figure 1.1.

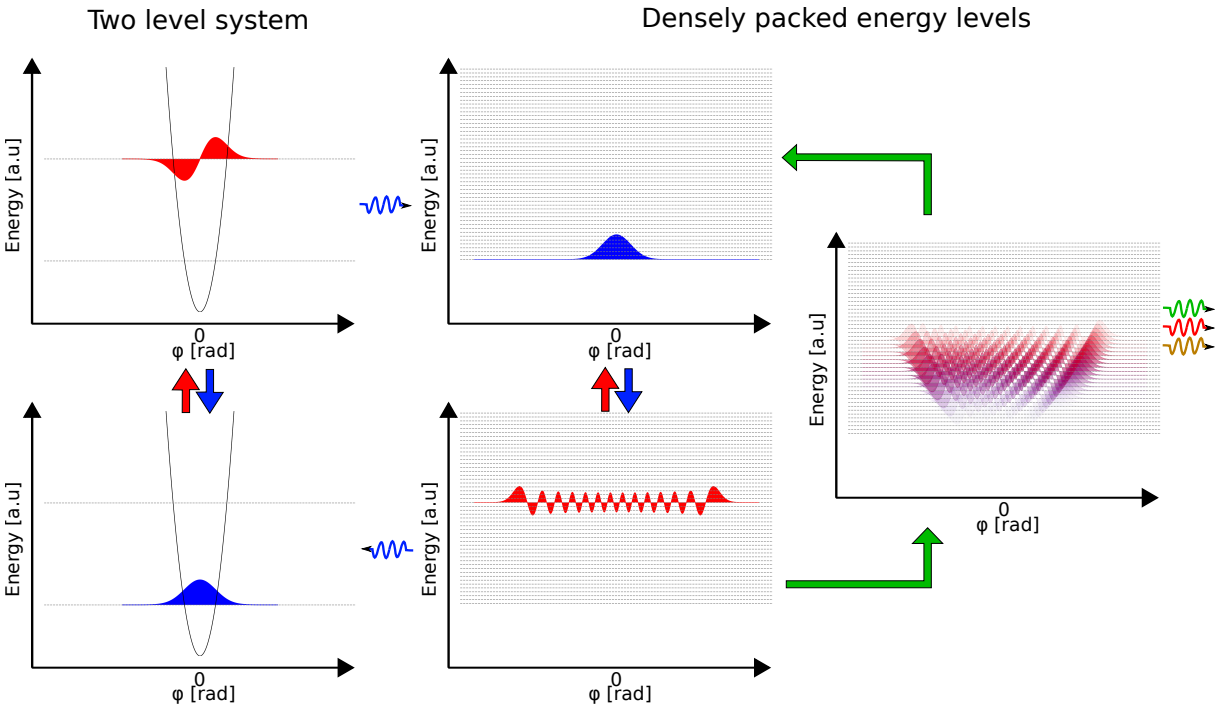

Figure 1.1: Excitation and decay of states in two level system coupled to a densely packed fluctuating energy level

The TLS in ground and excited state is shown on left side of the figure represented by blue and red colors. The densely packed energy levels (DPEL) are shown on the right side of the figure. When a TLS emits a photon to a DPEL, the system absorbs the energy and gets excited and the TLS relaxes to the ground state. These are shown by the blue arrows. Similarly when a DPEL emits photons with the frequency of the TLS, the TLS excites to the excited state and DPEL relaxes to ground state. This is a coherent process. However, when the DPEL fluctuates, the excited state of the DPEL relaxes by emitting photons are different frequencies compared to the TLS frequency. In other words, this fluctuation decreases the rate of emitting photons at TLS frequency. Additionally, these emitting photons are lost in the bath of energy levels. A representation of such fluctuation is shown in the right most figure where fluctuation is causing several levels to occupy with different probabilities. Over time the DPEL relaxes to the ground state given by green arrow. The DPEL could be modelled as an infinite number of harmonic oscillators[29][30] where fluctuations create an irreversible process.

Smaller the fluctuation in the DPEL, smaller is the energy relaxation and consequently larger is the coherent process of emitting photons back to the TLS. The time taken for the TLS to irreversibly relax to the ground state due to the DPEL fluctuation is known as relaxation time T_1.

To understand the dephasing mechanism, the TLS can be prepared in a superposed state as shown in Figure 1.2a with both states populated with equal probability. The phase of the system is given by $\Delta_0 t/\hbar$, where Δ_0 is the TLS energy. This can be seen in the Bloch sphere, which represents the Hilbert space of the TLS in rotating frame, as the vector shown in 1.2b. The rainbow color on the equator of the Bloch sphere represents the different phases varying from 0 to 2π.

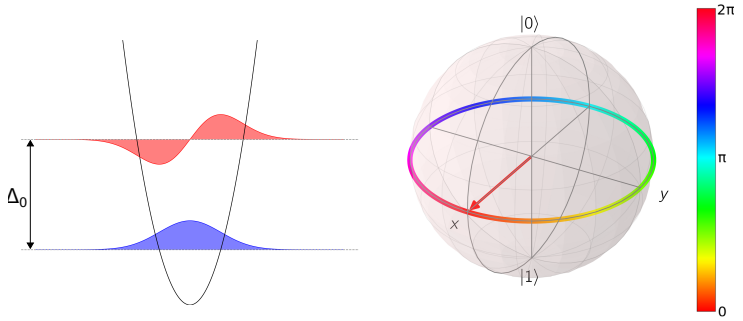

(a) (b)

Figure 1.2: (a) Two level system in a superposed state. (b) Representation of superposed state using Bloch sphere.

When there is no change in the TLS energy, there is no additional phase. But when the energy changes from its mean value Δ_0, system acquires additional phase. Hence any fluctuation in the energy levels changes the phase. An example of a random distribution of fluctuation of TLS energy is considered to exemplify the dephasing behaviour. The

histogram of the fluctuation given in terms of standard deviation of the energy is shown on the left side of Figure 1.3. The time evolution of the energy levels fluctuation is represented by black line on right side plot of the figure. For the considered example, between each point in the time series, the phase changes by $\pi/5$ if the TLS energy change by 4σ from the mean value Δ_0. Hence the dots on the time series change color with time. It can be observed that initially the additional phase of the system is close to zero given by red color but as time progress, an additional phase accumulates represented by change in color of dots. When such measurements are averaged over several runs, the phase is undefined over time. The time scale in which the phase is undefined is called the dephasing time T_Φ. The theoretical treatment of noise in the qubit is given in the measurement and analysis chapter of Fluxonium.

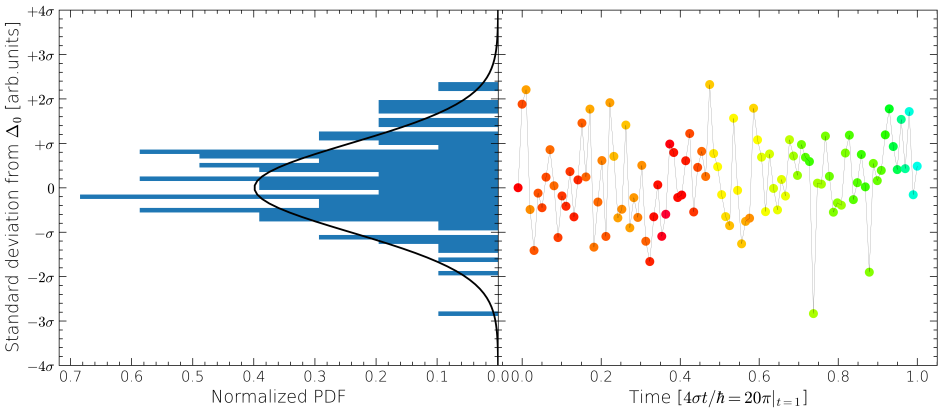

Figure 1.3: Histogram of fluctuations of TLS energy levels on left side with fluctuation shown as a function of time on the right side. The colored dots after each instance of time is the cumulative phase of the TLS.

The dissipation and decoherence in superconducting qubits is been studied for more than two decades. In this period, the relaxation and coherence times of the qubits have improved by 7 orders of magnitude. Figure 1.4 shows the increase in T_1 and T_2^* over the past two decades. It is hence important to study the losses in the state of the art qubits to achieve higher lifetimes.

1.4 Thesis overview

In this thesis, I try to qualitatively and quantitatively understand the reasons for losses based on theoretical studies done over the past four decades. This thesis is divided into two parts. First part is specifically concentrating on resonators. Second part describes the work done in understanding losses in the Fluxonium qubit. Each part consists of three chapters describing the theory, the design and the measurements performed respectively. Chapter 2 begins with theoretical description of the resonators and the modelling of losses

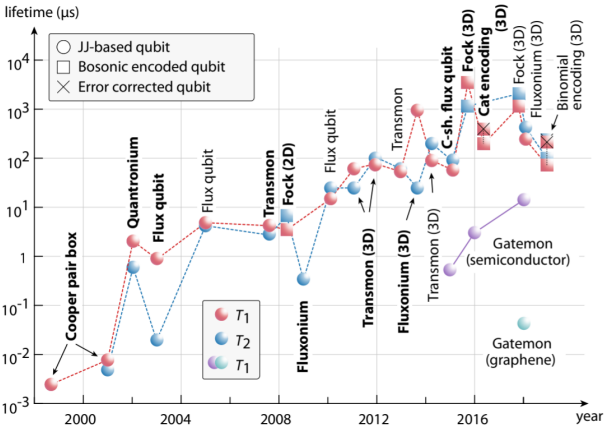

Figure 1.4: Graph showing year on year improvement in the relaxation and decoherence times [1].

with circuit elements where the term quality factor is defined. The numerical simulations on electrodynamics of the superconductors are performed to theoretically predict the behaviour of equilibrium quasiparticles as a function of temperature in 2D resonators.
The other losses important for the samples measured in this work are briefly explained. A review of the model used to explain parasitic TLS behaviour is carried out and possible sources of parasitic TLSs are shown. Next focal points which are the losses due to conductivity in ground plane and substrate are discussed. The model used to explain excess quasiparticles by subgap states in superconductors is briefly explained.
Chapter 3 demonstrates the design of the resonators and waveguide in HFSS software where the electric field distribution in resonators and waveguide are shown and the properties of the waveguide are discussed. This is followed by the detailed discussion on the fabrication of resonators which involves different techniques and recipes. Their structural properties characterized using AFM to obtain accurate results on the dimensions of the resonators are shown in the chapter. For instance, the SEM image of a resonator and the picture of the waveguide with sample is shown in Figure 1.5.

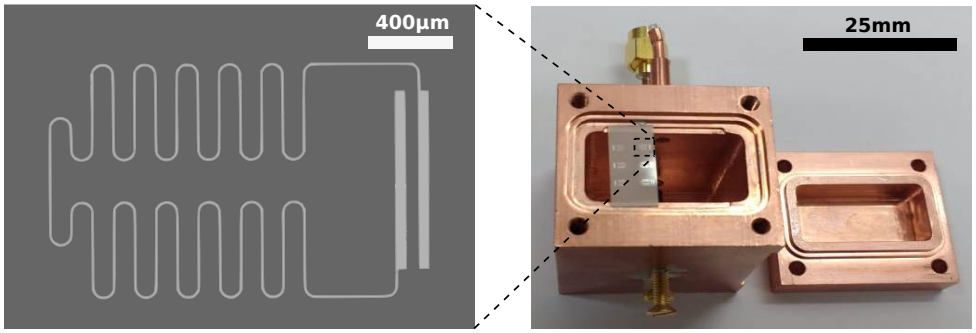

Figure 1.5: The SEM image of a resonator in the inset of the waveguide with sample

Chapter 4 presents the results of DC and RF measurements of the films and 2D resonators, respectively. The various properties of the samples obtained from DC measurements are discussed with their implications. This is followed with the presentation of the RF mea-

surements with VNA and the circle fitting of data to obtain the internal quality factor. The photon number and temperature dependence of the quality factor is demonstrated and the effective change in the kinetic inductance ratio with respect to the mean free path is discussed. The data about quality factor is later used to discuss the losses observed in this work. A detailed discussion on thermal quasiparticle loss, ground plane loss, TLS loss and AC loss in the resonators is given in this chapter.
From the chapter 5, the thesis concentrates on 2D Fluxonium qubit. In this PhD thesis, I consider a novel design based on a full 2D Fluxonium with resonators and transmission line integrated on the same chip as the qubit. This chapter dedicates to the discussion on the theory of Fluxonium from circuit modelling to the numerical calculation of the energy spectrum and wavefunctions. It also focuses on the advantages of using JJ chains as an inductor for realizing the qubit. The modes of the JJ chains calculated considering ground capacitance is briefly discussed. The concept of phase slips and its variation with E_J/E_C is explained. The coupling of the qubit with the environment and the readout is studied in detail. The parameters responsible for controlling coupling strength is shown.
In the chapter 6, the simulations of the resonators of the readout to optimize the design is presented from which coupling capacitance and resonator capacitance are estimated. The realized fabrication steps are thoroughly explained and the recipe is given for the samples fabricated. The SEM image of the qubit and the picture of the sample holder is shown in Figure 1.6. The DC measurement of test junctions to calculate E_J is briefly mentioned in the chapter.

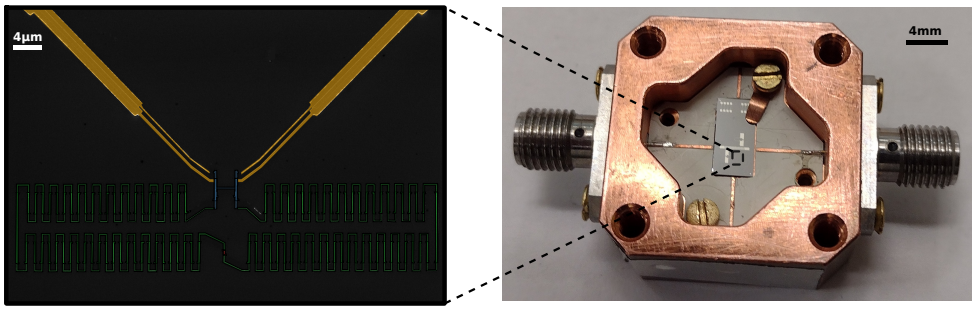

Figure 1.6: The SEM image of a qubit in the inset of the RF box with sample

Chapter 7 consists of the measurement setup details including spectroscopy and time domain measurements of the qubit. A detailed explanation of spectroscopy is given with the data. Different time domain measurements are explained intuitively using Bloch sphere and derived mathematically and the data of the measurements are shown. The discussion on loss mechanisms for relaxation is provided. The loss limits in the samples are shown and are compared to the state of the art. The decoherence mechanism is also explained in detail. The data of decoherence is shown and the potential reasons are discussed.

Part I

Resonators

Chapter 2

Theoretical background

This chapter is divided into two parts. Firstly the theory of LC resonator is presented considering an ideal case. Nevertheless, in this kind of system, there are losses which needs to be taken into account. Hence these losses are briefly explained using circuit elements. This work involves having superconducting LC resonator inside a waveguide. In the second part, a detailed explanation of the dominating losses in such resonators are provided.

2.1 LC resonator

An LC resonator is a simplest linear electrical circuit which can be described as an inductor in parallel with a capacitor. In this section, a quantum mechanical illustration of the LC resonator is provided in order to stipulate its importance in quantum systems. Additionally, the circuit element description of the losses in such resonators are provided.

2.1.1 An ideal quantum harmonic oscillator

In circuit quantum electrodynamics, the LC resonator can be represented as a quantum harmonic oscillator. Hence the resonator can be described as an oscillator with a harmonic potential. The admitted energy values of such a system are discrete and are equally spaced in energy scale. An LC resonator is shown in Figure 2.1a, where L is the inductance and C is the capacitance.
In classical mechanics, Hamiltonian of the LC circuit can be written as

$$H = \frac{\Phi^2}{2L} + \frac{Q^2}{2C} \tag{2.1}$$

where Φ is the flux through the inductor and Q is the charge across the capacitance. Therefore, the first term on the right side of the equation corresponds to the magnetic energy stored in the inductor while the second term is the electric energy stored in the capacitor.
The above Hamiltonian can be described quantum mechanically as [31].

$$\hat{H} = \hbar\omega_0 \left(\hat{a}^\dagger \hat{a} + \frac{1}{2}\right) \text{ where } \omega_0 = \frac{1}{\sqrt{LC}} \tag{2.2}$$

where ω_0 is known as the eigen frequency of the resonator and $\hat{a}^\dagger$ and $\hat{a}$ are respectively the creation and annihilation operators defined as follows:

$$\hat{a}^\dagger = \frac{1}{\sqrt{2}}(\hat{q} + i\hat{\phi}), \quad \hat{a} = \frac{1}{\sqrt{2}}(\hat{q} - i\hat{\phi}) \tag{2.3}$$

In this relation, q and ϕ represent the normalized charge and flux operators which are quantum mechanical equivalents of the classical circuit variables Q and Φ. The correspondence between variable and quantum mechanical operators is given by:

$$\hat{q} \to \sqrt{\frac{L\omega_0}{\hbar}}Q, \quad \hat{\phi} \to \frac{\Phi}{\sqrt{\hbar\omega_0 L}} \tag{2.4}$$

The creation and annihilation operators follow the commutation relation defined as:

$$\left[\hat{a}, \hat{a}^\dagger\right] = 1 \tag{2.5}$$

Furthermore, they can be used to define the number of discrete energy levels (n) since

$$\hat{a}^\dagger\hat{a} = n \tag{2.6}$$

Such discrete energy levels are generally represented on a potential energy diagram as shown in Figure 2.1b. It is important to notice that this simple linear circuit can be subjected to different kind of losses, which will be discussed more in details in the next session.

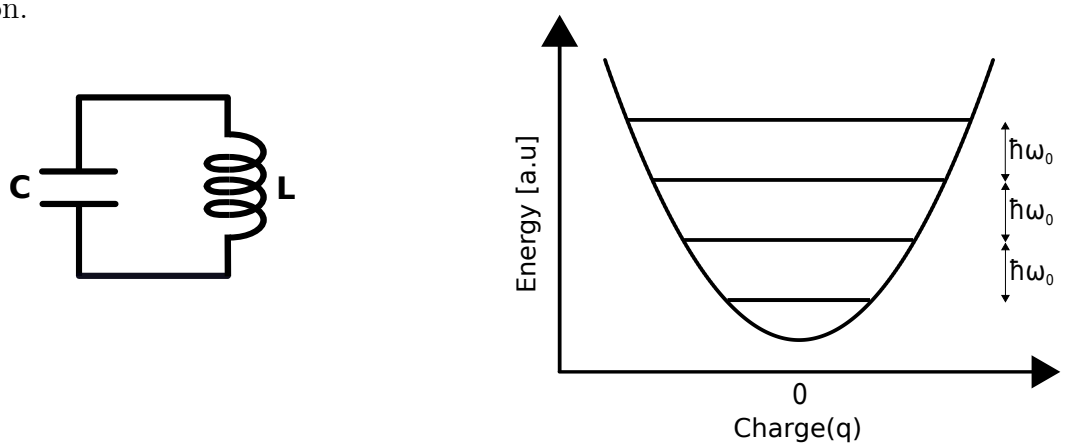

(a) (b)

Figure 2.1: (a) Circuit representation of an LC oscillator. (b) Representation of potential energy and energy levels of a quantum harmonic oscillator.

2.1.2 Resonators with losses

The common way to model the losses taking place in an LC circuit involves the addition of an effective resistance $R_{eff}(n)$ in series to the inductor and a conductive loss channel G(n)

in parallel to the capacitor. Both the conductive and resistive losses have dependence on n which is the number of photons of frequency ω_0 in the resonator. The model circuit is shown in Figure 2.2.

This model is close to the reality since G(n) accounts for the dielectric loss or the TLS

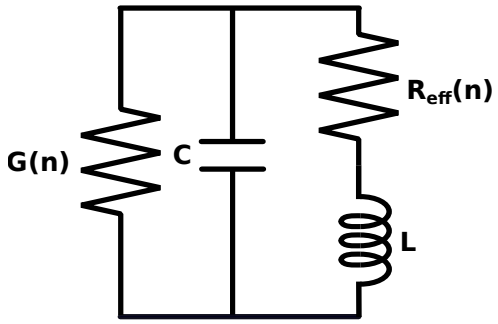

Figure 2.2: The LC resonator with losses given by resistance $R_{eff}(n)$ and conductance G(n).

loss in the capacitor and $R_{eff}(n)$ includes a combination of losses such as quasiparticle loss, AC loss and ground plane loss whose information is provided in the next section.
The losses or dissipation in the resonators are quantified by a parameter called quality factor. It can be defined as the ratio of the energy stored in the resonator to the energy dissipated per cycle by the lossy channels. By simplification it can be expressed as the ratio of resonant frequency f_r to the bandwidth of the resonator Δf.

$$Q = 2\pi \frac{\text{Energy stored}}{\text{Energy dissipated per cycle}} = \frac{f_r}{\Delta f} \tag{2.7}$$

A detailed derivation of the quality factor associated to the circuit modeled in this work is reported in the appendix A. The final result is reported in the following equation:

$$Q = \frac{\sqrt{\frac{1+R_{eff}(n)G(n)}{LC} - \left(\frac{G(n)}{2C} + \frac{R_{eff}(n)}{2L}\right)^2}}{\left(\frac{G(n)}{C} + \frac{R_{eff}(n)}{L}\right)} \tag{2.8}$$

Depending on the dominant losses, the quality factor can be expressed as follows:

$$\begin{aligned} Q &= \frac{\omega L}{R_{eff}(n)} \text{ when } G(n) << \frac{C}{L} R_{eff}(n) \\ Q &= \frac{\omega C}{G(n)} \text{ when } G(n) >> \frac{C}{L} R_{eff}(n) \end{aligned} \tag{2.9}$$

Therefore, any change in the photon number will turn in different values for both G and R_{eff}, which changes the quality factor. The dependence of quality factor on photon number is discussed in more details in the TLS and AC loss sections of the chapter.

2.1.3 Coupling to environment

The resonator is excited by an AC source in a Vector network analyzer (VNA). Since the resonator is coupled to the waveguide port, the circuit schematic is as shown in the Figure 2.3 where the resonator with impedance Z_R is coupled capacitively with capacitance C_C to transmission line whose characteristic impedance is given by Z_0. Resonator coupling to the environment introduces additional loss. The total loss observed in hence the sum of resonator loss and coupling loss. This is given as $1/Q_L = 1/Q_C + 1/Q_i$ where Q_i is internal quality factor of the resonator and Q_C is the coupling quality factor and Q_L is the total quality factor.

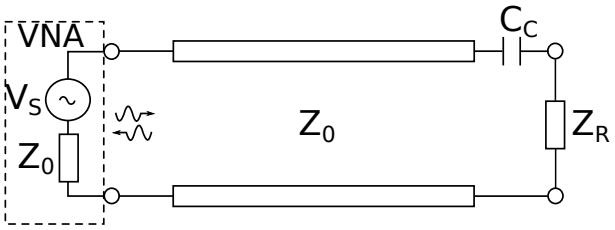

Figure 2.3: Schematic of resonator with impedance Z_R coupled capacitively to a source through the transmission line with impedance Z_0

For such a circuit, the measurements are performed in reflection. The reflection coefficient as a function of frequency f for such circuit was shown to be [32]:

$$S_{11}(f) = \Gamma_d \left[\frac{(1-\kappa)/(1+\kappa) + i2Q_L\delta(f)}{1 + i2Q_L\delta(f)} \right] \tag{2.10}$$

where $\kappa = Q_i/Q_L - 1$, $\delta(f) = (f - f_0)/f_0$, $f_0 = \omega_0/2\pi$ and Γ_d is the added phase due to impedance mismatch. The program for fitting the measurements obtained is given by Probst [33], which uses the well described circle fit of the reflected signal. By the fitting of the measurements, the losses originating within the resonator can be distinguished from losses introduced by coupling. From here on, losses intrinsic to resonator are discussed in this part of the thesis.

2.2 Superconducting resonator losses at high temperatures

The first dominating loss mechanism as the temperature of the resonator starts to decrease below critical temperature of the superconductor comes from the thermal quasiparticles. Quasiparticles are the single electrons in a superconductor whose motion induces losses. Losses due to thermal quasiparticles is studied in detail in 3D cavities [34]. This work aims to study the effect of thermal quasiparticles in resonators of 2D geometry. Hence one

needs to understand on relationship between the thermal quasiparticles and the effective resistance discussed in section 2.1.2.

2.2.1 Superconductor length scales

The definition of superconductor length scales are of importance while studying the losses originating from the electrodynamics in a superconducting resonator. The length scales that define the electrodynamics of a superconductor are:

- **the residual electron mean free path (l)** which is the distance between two consecutive collisions of an electron with a defect or an impurity of a metal.
- **the intrinsic coherence length (ξ_0)** which represents the maximum spatial distance between a Cooper pair. The intrinsic coherence length can be expressed as:

$$\xi_0 = \frac{\hbar v_F}{\pi \Delta(0)} \tag{2.11}$$

  with $\Delta(0) = 1.764 k_B T_C$, the superconducting gap at 0K, T_C the critical temperature and v_F the Fermi velocity of the electrons.
- **the London penetration depth (λ_L)** which represents the distance over which the magnetic field entering the surface of the superconductors exponentially decays. It is given by:

$$\lambda_L = \sqrt{\frac{m}{\mu_0 n_S e^2}} \tag{2.12}$$

  where e is the electron charge, m is the mass of electron, n_S is the density of superconducting electrons and μ_0 is the free space permeability.

In the year 1955, Pippard defined a coherence length taking into account the electron scattering as an additional contribution to the ξ_0. Therefore, Pippard coherence length ξ_P is defined [35]:

$$\frac{1}{\xi_P} = \frac{1}{\xi_0} + \frac{1}{l} \tag{2.13}$$

By further modifications, the effective coherence length and penetration depth when $l << \xi_0$ is given as:

$$\begin{aligned} \xi &= \sqrt{\xi_0 \xi_P} \approx \sqrt{\xi_0 l} \\ \lambda &= \lambda_L \sqrt{\frac{\xi_0}{\xi_P}} = \lambda_L \sqrt{1 + \frac{\xi_0}{l}} \end{aligned} \tag{2.14}$$

These effective length scales are used to obtain the intrinsic coherence length and London penetration depth in the results and analysis chapter.
The intrinsic length scales defined above can be used to classify superconductors into four

regimes as shown in Figure 2.4. When the residual mean free path (l) of the superconducting film is larger than its intrinsic coherence length (ξ_0), the superconductor is said to be in the clean limit, or else, it is in the dirty limit. Similarly, when the effective penetration depth (λ) is larger than the intrinsic coherence length (ξ_0) the superconductor is said to be in the local limit, and in the non-local limit otherwise.

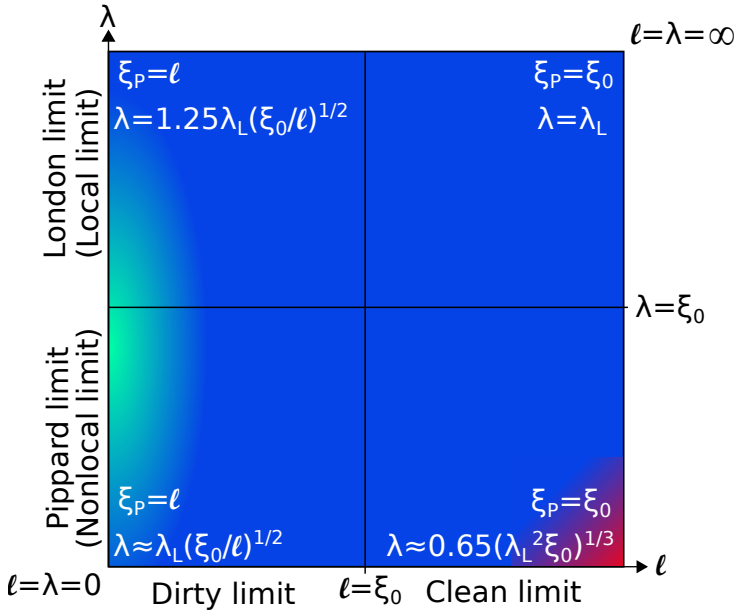

Figure 2.4: Superconductor classification based on superconducting length scales (l, λ and ξ_0.) The green shaded area denotes the region in which the majority of superconducting quantum circuits belong. Red region is the extreme anomalous limit.

In order to understand the effect of quasiparticles in the resonators, it is important to study how the device behaves in different regimes presented in the figure. Indeed, all the study up to now on superconducting resonators are focused on thin films of Aluminum (Al) [36][37] or Niobium nitride (NbN) [38], NbTiN [39] etc. While thin films of Al with small mean free path are in the dirty local limit, bulk Al with large mean free path is reported to be in the clean non-local limit [40][41]. Hence in order to study different regimes this work considers Al as a material of choice. For this purpose, different thickness of the material are considered since mean free path is limited by the thickness of the material.

2.2.2 Electrodynamics and kernel

The study of effects of electric or magnetic field on superconductor is important to know the origin of microscopic losses such as quasiparticle loss. The current density is said to be directly proportional to the average of the field over a region comparable to the coherence length of the superconductor. Phenomenologically, these equations are given as [42]:

$$\vec{J}_s(\vec{r}) = -\frac{3}{4\pi\xi_0\lambda_L^2}\int_V \frac{\vec{R}[\vec{R}.\vec{A}(\vec{r'})]}{R^4} e^{-R/\xi_P} d\vec{r'} \tag{2.15}$$

where $J_s(\vec{r})$ is the current density of superconductor at position $\vec{r}$ and $\vec{A}(\vec{r'})$ is the vector potential at position $\vec{r'}$. $\vec{R}$ is the distance between the field at position $\vec{r'}$ and point of consideration for the current density at $\vec{r}$. The Equation 2.15 is also known as the non-local current density equation.

When $\xi_P \to 0$ or $\xi_P << \lambda$, the vector potential $\vec{A}(\vec{r'})$ is constant over the distance ξ_P in the superconductor. The exponential in Equation 2.15 can be treated as a delta function such that

$$\vec{J_s}(\vec{r}) = -\frac{3}{4\pi\xi_0\lambda_L^2}\int_0^R\int_0^{2\pi}\int_0^{\pi}\frac{\vec{R}[\vec{R}.\vec{A}(\vec{r'})]}{R^4}\xi_P\delta(R)R^2 sin\theta d\theta d\phi dR = -\frac{\vec{A}(\vec{r})}{\lambda^2} \tag{2.16}$$

When above mentioned limiting case is considered non-local current density reduces to the well known London limit [15] where current density is no more an average of the vector potential.

The above Equation 2.15 for superconductor was further refined by Mattis and Bardeen who included the microscopic effects such as the density of states and the electron energy distribution [18], as a function of frequency and temperature from BCS theory. The current density hence changes to [43]:

$$\begin{aligned}
\vec{J}(\vec{r}) &= -\frac{3}{4\pi^2\hbar v_F\lambda_L^2}\int_V\frac{\vec{R}[\vec{R}.\vec{A}(\vec{r'})]}{R^4}I(\omega,R,T)e^{-R/l}d\vec{r'} \\
I(\omega,R,T) &= -j\pi\int_{\Delta-\hbar\omega}^{\Delta}[1-2f(E+\hbar\omega)][g(E)cos\alpha\Delta_2 - jsin\alpha\Delta_2]e^{j\alpha\Delta_1}dE \\
&\quad -j\pi\int_{\Delta}^{\infty}[1-2f(E+\hbar\omega)][g(E)cos\alpha\Delta_2 - jsin\alpha\Delta_2]e^{j\alpha\Delta_1}dE \\
&\quad +j\pi\int_{\Delta}^{\infty}[1-2f(E)][g(E)cos\alpha\Delta_1 - jsin\alpha\Delta_1]e^{j\alpha\Delta_2}dE
\end{aligned} \tag{2.17}$$

where

$$\begin{aligned}
\Delta_1 = \sqrt{E^2-\Delta^2},\ \Delta_2 = \sqrt{(E+\hbar\omega)^2-\Delta^2} \\
g(E) = \frac{E^2+\Delta^2+\hbar\omega E}{\Delta_1\Delta_2}\ \text{and}\ \alpha = \frac{R}{\hbar v_F}
\end{aligned} \tag{2.18}$$

where $f(E)$ is the Fermi-Dirac distribution and E is the energy of the electrons in the superconductor.

The current density can be rewritten in short as $\vec{J}(\vec{r}) = \int_V K(\vec{R})\vec{A}(\vec{r'})d\vec{r'}$, where $K(\vec{R})$ is called the kernel in spatial domain. In order to calculate the quasiparticle dependent conductivity in superconductor, one needs to calculate the kernel.

By following the same lines of Popel and Gao [44], it is possible to express the kernel in the wavevector domain as K(q) by taking the Fourier transform of current density. This

helps in solving the above equation as follows:

$$\begin{aligned} J(q) &= -K(q)A(q) \text{ where} \\ K(q) &= -\int_{-\infty}^{\infty} K(\vec{R})e^{jqR} \end{aligned} \tag{2.19}$$

and by solving the Equation 2.19 the kernel can be expressed as:

$$\begin{aligned} K(q) = -\frac{3}{\pi\hbar v_F \lambda_L^2 q}\int_0^{\infty}\left(\frac{sinx}{x^3}-\frac{cosx}{x^2}\right)I(\omega, x/q, T)e^{-x/ql}dx \\ \text{and } x = qR \end{aligned} \tag{2.20}$$

where q and R are conjugate variables in space-wavevector domain, hence when $q \to 0$, $R \to \infty$ and vice-versa. The detailed derivation of the kernel is given in Appendix A of Gao's thesis [44].
When the London limit valid for $\xi_0 << \lambda$ is considered, the Fourier transform of current density given in Equation 2.16, defines the London kernel K_L

$$\begin{aligned} FT(\vec{J}(\vec{r})) = -FT\left(\frac{\vec{A}(\vec{r})}{\lambda^2}\right) \text{ or } J(q) = -K_L A(q) \text{ hence} \\ K_L = \frac{1}{\lambda^2} \end{aligned} \tag{2.21}$$

K_L is independent of q.
The theoretical values λ_L, ξ_0 and v_F of Al is given in Table 2.1. They are used for the evaluation of the kernel.
Figure 2.5 reports the variation of kernel as a function of q for Al characterized by

Values	$\lambda_L[nm]$	$\xi_0[nm]$	$v_F[ms^{-1}]$
Theoretical	16	1600	1.23×10^6

Table 2.1: Materials properties of superconducting Al

different mean free paths. The kernel can be divided into three regimes based on the values of the wavevector q:

- $q << max\left(\frac{1}{\xi_0}, \frac{1}{l}\right)$, where the kernel is a constant $K(l, q \to 0)$.
- The second regime is when K(q) has a transition. It happens at $q \approx max\left(\frac{1}{\xi_0}, \frac{1}{l}\right)$ shown in Figure 2.5 by the ticks.
- In the third regime, K(q) reduces as 1/q for large wavevectors i.e. $q >> max\left(\frac{1}{\xi_0}, \frac{1}{l}\right)$.

To understand this better, firstly the extreme case is considered where $l \to \infty$ and $\xi >> \lambda$ which is called the extreme anomalous limit by Mattis and Bardeen. In this

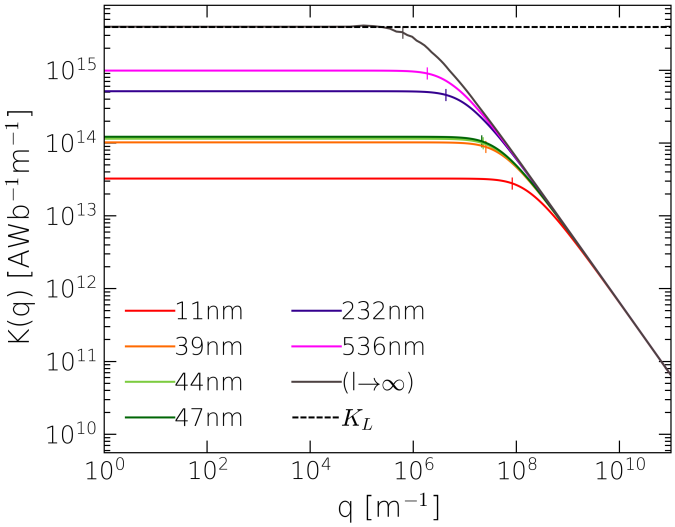

Figure 2.5: Superconductor kernel as a function of wavevector given for different mean free paths at T=0.3K and $\omega = 5GHz$. The dashed line represents the London kernel value. The ticks on the graphs represent the positions of q where $q = max(\xi_0^{-1}, l^{-1})$.

extreme anomalous limit, $R = 0$ in spatial domain and Equation 2.17 becomes

$$\begin{aligned} I(\omega,0,T) = -j\pi \int_{\Delta-\hbar\omega}^{\Delta} [1-2f(E+\hbar\omega)]g(E)dE \\ -j2\pi \int_{\Delta}^{\infty} [f(E)-f(E+\hbar\omega)]g(E)dE \end{aligned} \tag{2.22}$$

When $E < \Delta$, Δ_1 in Equation 2.18 becomes complex, giving raise to real and imaginary part for $I(\omega,0,T)$. Glover and Tinkham [45] had introduced complex conductivity and from Mattis-Bardeen theory by taking the ratio of current density in superconducting state and the normal state, the conductivity ratio is defined as:

$$\begin{aligned} \frac{J}{J_n} = \frac{\sigma_1 - j\sigma_2}{\sigma_n} = \frac{I(\omega,0,T)}{I(\omega,0,T_C)} \text{ where } I(\omega,0,T_C) = -j\pi\hbar\omega \\ \text{Hence } I(\omega,0,T) = -j\pi\hbar\omega \left(\frac{\sigma_1 - j\sigma_2}{\sigma_n}\right) \end{aligned} \tag{2.23}$$

where $\sigma_1 - j\sigma_2$ is the complex conductivity.
Hence the kernel of the extreme anomalous limit in the third regime i.e. $K(l \to \infty, q \to \infty)$ is given from Equations 2.20 and 2.23 as

$$\begin{aligned} K(l\to\infty, q\to\infty) = -\frac{3I(\omega,0,T)}{\pi\hbar v_F \lambda_L^2 q} \int_0^{\infty} \left(\frac{sinx}{x^3} - \frac{cosx}{x^2}\right) dx = \frac{3\pi\omega}{4v_F\lambda_L^2 q}\left(\frac{\sigma_2 + j\sigma_1}{\sigma_n}\right) \\ \text{since } \int_0^{\infty} \left(\frac{sinx}{x^3} - \frac{cosx}{x^2}\right) dx = \left.\frac{x^2 sincx - sinx + xcosx}{x^2}\right|_0^{\infty} = \frac{\pi}{4} \end{aligned} \tag{2.24}$$

When one assumes $R >> \xi$ i.e. $R \to \infty$ or $q \to 0$ in Equation 2.17, then the situation is similar to the Local limit. The exponential can be treated as a delta function and the current density reduces to Equation 2.16 where $\lambda = \lambda_L$ since $\xi_P = \xi_0$. The kernel $K(l \to \infty, q \to 0)$ becomes K_L which is the London kernel as shown in the numerically calculated Figure 2.5. Therefore in the extreme case, Kernel goes from London limit for $q \to 0$ to $1/q$ dependence for $q \to \infty$ with transition at $q = 1/\xi_0$.
For finite mean free path l when $l < \xi_0$, $K(l, q \to 0)$ is smaller than the London kernel as it can be seen by computing in Figure 2.5. Numerically, these values can be obtained can be replacing $q \approx 3\pi/4l$ in Equation 2.24:

$$K(l, q \to 0) \approx \frac{l\omega}{v_F \lambda_L^2} \left(\frac{\sigma_2 + j\sigma_1}{\sigma_n} \right) \tag{2.25}$$

2.2.3 Complex conductivity of superconductors

The conductivity of superconductors has been studied even before the establishment of the microscopic theory of superconductivity [46, 47]. In this section, the microscopic theory is used to understand the conductivity due to charge carriers.
Electrical conductivity of a metal defines the ease of flow of charge carriers. In a normal state metal the charge carriers are electrons. Instead, in a superconductor there are two different carriers. The two carriers are the quasiparticles and the Cooper pairs.
It gives raise to complex conductivity as seen in Equation 2.23. The real part of the conductivity (σ_1) is due to quasiparticles and the imaginary part (σ_2) is due to Cooper pairs. Since $K(l \to 0, q \to 0) = K(l \to \infty, q \to \infty)$, the conductivity in extreme anomalous limit can be used to extract conductivity in extreme dirty limit. In particular, by substituting Equation 2.22 into 2.23 results in:

$$\begin{aligned} \frac{\sigma_1}{\sigma_n} &= \frac{2}{\hbar\omega} \int_{\Delta}^{\infty} [f(E) - f(E + \hbar\omega)] g(E) dE \\ &\quad + \frac{1}{\hbar\omega} \int_{\Delta - \hbar\omega}^{-\Delta} [1 - 2f(E + \hbar\omega)] g(E) dE \\ \frac{\sigma_2}{\sigma_n} &= \frac{1}{\hbar\omega} \int_{(\Delta - \hbar\omega, -\Delta)}^{\Delta} [1 - 2f(E + \hbar\omega)] \frac{E^2 + \Delta^2 + \hbar\omega E}{\sqrt{\Delta^2 - E^2}\sqrt{(E + \hbar\omega)^2 - \Delta^2}} dE \end{aligned} \tag{2.26}$$

where $g(E)$ is the normalized density of states (DOS). This above equation for conductivity is famously known as the Mattis-Bardeen equation.
The normalized DOS of the normal state metal is shown in Figure 2.6 by orange dashed lines. As temperature is reduced below T_C, the superconducting gap opens and the states within the gap region gets redistributed both above and below the gap. Therefore, the DOS increases above and below the gap in the superconductor as temperature further reduces as shown by red and blue bold lines in the Figure 2.6a and 2.6b.

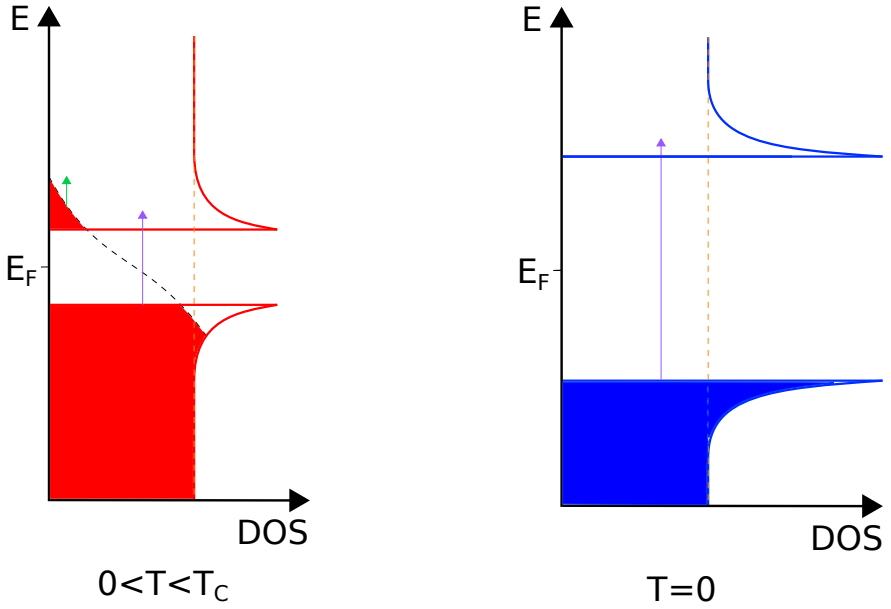

Figure 2.6: Normalized density of states of quasiparticles for (a) $0 < T < T_C$ and (b) T=0K. Black dashed lines shows the Fermi-Dirac distribution of single electrons. Red and blue shaded area represents the states filled with electrons. The green and purple arrow shows excitation of quasiparticles by photon below and above the gap energy.

In Figure 2.7a, the conductivity ratio σ_1/σ_{nDC} as a function of temperature is shown for different mean free path. The conductivity of quasiparticles is governed by the movement of single electrons from occupied states to empty states. The addition of states above and below the gap results in increases of σ_1. However, as the temperature decreases the partially filled states above and below the gap reduces, decreasing the density of the free moving quasiparticles available for conduction. The product of the two counteracting factors (i.e. Fermi-Dirac distribution and density of states) in Equation 2.26 is responsible for the peak in σ_1/σ_{nDC} close to T_C as shown in Figure 2.7a and it is called as coherence peak.

The coherence peak reduces with increasing mean free path. This is explained by the increased amount of states the electrons can access due to reduced scattering in longer mean free path systems. For longer mean free path samples, the quasiparticle conductivity ratio reduces rapidly below 1 for temperature smaller than T_C. Therefore, equilibrium quasiparticle density reduces for samples having longer mean free path.

In Figure 2.7b, the Cooper pair conductivity ratio σ_2/σ_{nDC} as a function of temperature is shown for different mean free paths. The electrons within the gap form Cooper pairs. They are responsible for the resistance free motion of electrons. As temperature reduces, the density of Cooper pair increases due to the increase in the gap giving raise to an increase of conductivity.

Even though, the Cooper pair density is large for longer mean free path samples, the ratio

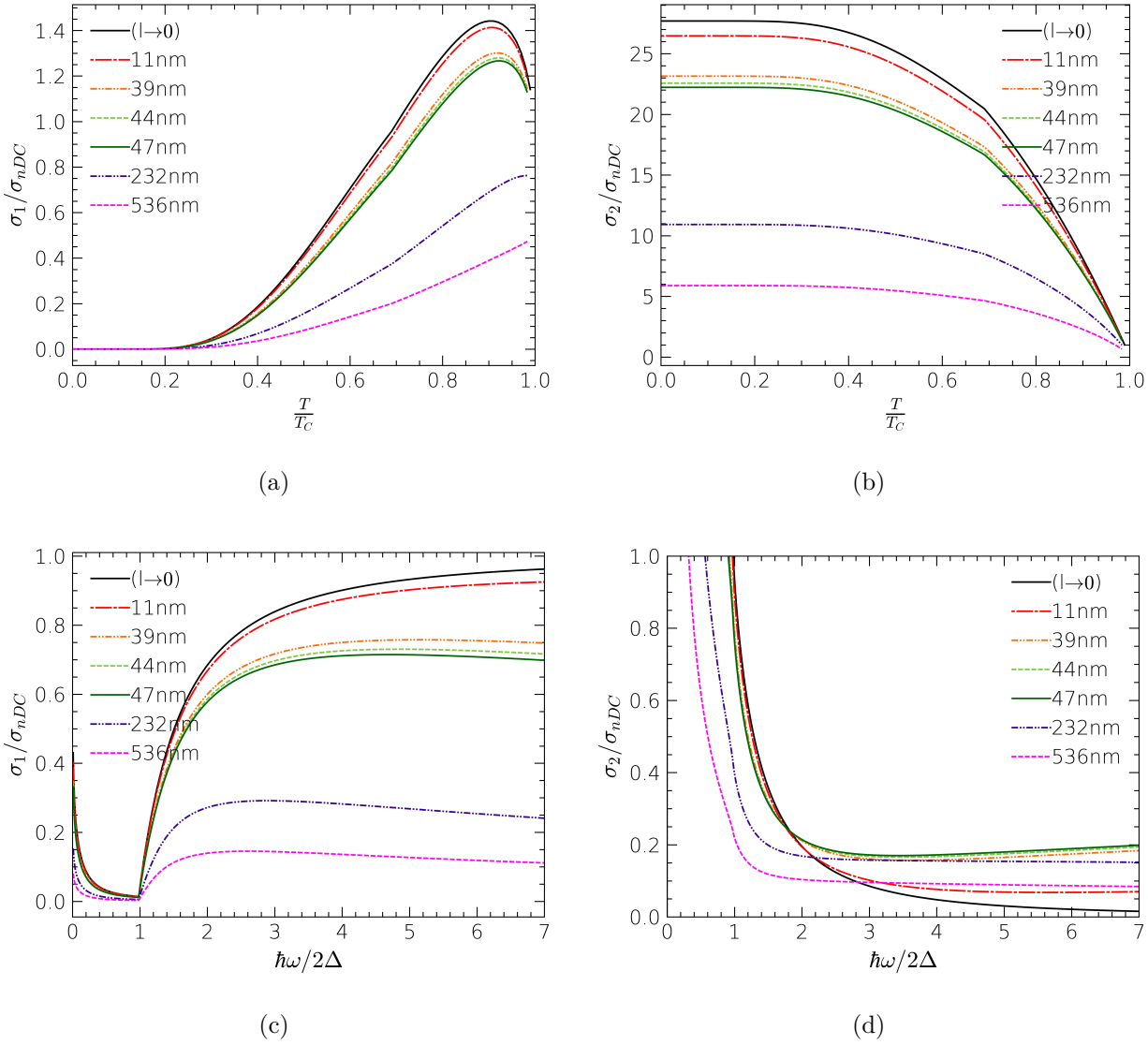

Figure 2.7: Conductivity ratio as a function of temperature from 0 to T/T_C at $\omega = 5GHz$ for different mean free paths for (a) quasiparticles and (b) Cooper pairs.
Conductivity ratio as a function of frequency with photon energy from 0 to 7 times the superconducting gap at T=0.5K for different mean free paths for (c) quasiparticles and (d) Cooper pairs.

of their conductivity with respect to normal state metal is smaller than short mean free path samples. It is because, the normal conductivity of long mean free path samples is large.

The conduction of quasiparticles and Cooper pairs is regulated by thermal energy which is dominated by Fermi-Dirac distribution as just discussed. These quantities are also influenced by incident photons of energy $\hbar\omega$. In Figure 2.7c σ_1/σ_{nDC} is shown as a function of applied frequency. For a given temperature, when the frequency increases until $\hbar\omega = 2\Delta$, the conductivity due to quasiparticles reduces. This is explained by reduction of DOS available for conduction away from the edge of the superconducting gap. This can be seen

by the green arrow in Figure 2.6a.
When $\hbar\omega > 2\Delta$, the quasiparticle conductivity increases again since quasiparticles below the superconducting gap get excited to states above the gap shown by purple arrows in Figure 2.6 and hence the conductivity smoothly increases. For large frequencies, the larger mean free path samples have a smaller conductivity ratio since at high frequencies the superconductors behave as an anomalous metal.
The conductivity of Cooper pairs are said to be like a Dirac-delta function in-terms of energy, with a peak at $\omega = 0$. As frequency increases, the Cooper pairs gain momentum and their conductivity decreases as shown in Figure 2.7d.
The conductivity ratio of superconductor described in Equation 2.26 is limited to the dirty limit. Nevertheless, for finite mean free paths the conductivity differs. Therefore, in order to evaluate the conductivity for different mean free paths, it is important to calculate the surface impedance first.

2.2.4 Surface impedance and electron mean free path

The surface impedance Z_S is defined as the ratio of the parallel electric field $E_{||}$ to the parallel magnetic field $H_{||}$ of an electromagnetic (EM) wave impinging on the surface of a superconductor as shown in Figure 2.8. It is expressed as:

$$Z_S = \frac{E_{||}}{H_{||}} \tag{2.27}$$

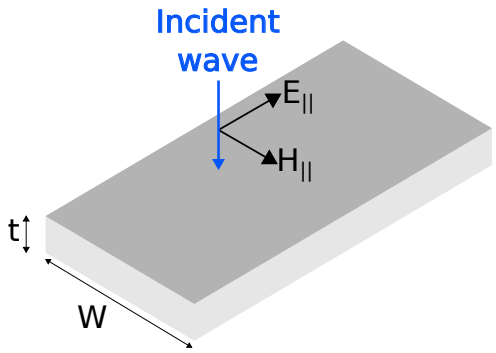

Figure 2.8: A conducting film with thickness(t) and width(W) where an EM wave is normally incident.

Using the kernel discussed previously in Equation 2.20, surface impedance is calculated based on the Reuters and Sondheimer's work [48] for an infinitely thick film given by:

$$Z_S = \frac{j\mu_0\omega\pi}{\int_0^\infty ln\left(1 + \frac{K(q)}{q^2}\right) dq} \tag{2.28}$$

The surface impedance in terms of conductivity is defined by [49]:

$$Z_S = \sqrt{\frac{j\omega\mu_0}{\sigma}} \tag{2.29}$$

where σ in this case is the complex conductivity of the superconductor. From the above Equations 2.28 and 2.29, a general relationship between kernel and conductivity is established.

Furthermore, the surface impedance Z_S has a real part which is the surface resistance due to equilibrium quasiparticles and imaginary part coming from inductive part due to Cooper pairs since σ is complex. From the impedance the surface resistance R_S and penetration depth λ is deduced to be:

$$Z_S = R_S + j\omega\mu_0\lambda \tag{2.30}$$

These quantities are a function of mean free path is shown in Figure 2.9a and 2.9b respectively. The numerical calculations shown in the figure are obtained by considering superconducting gap to be $1.764k_BT_C$ with $T_C = 1.2K$, frequency $\omega/2\pi = 5GHz$ and temperature $T = 0.3K$.

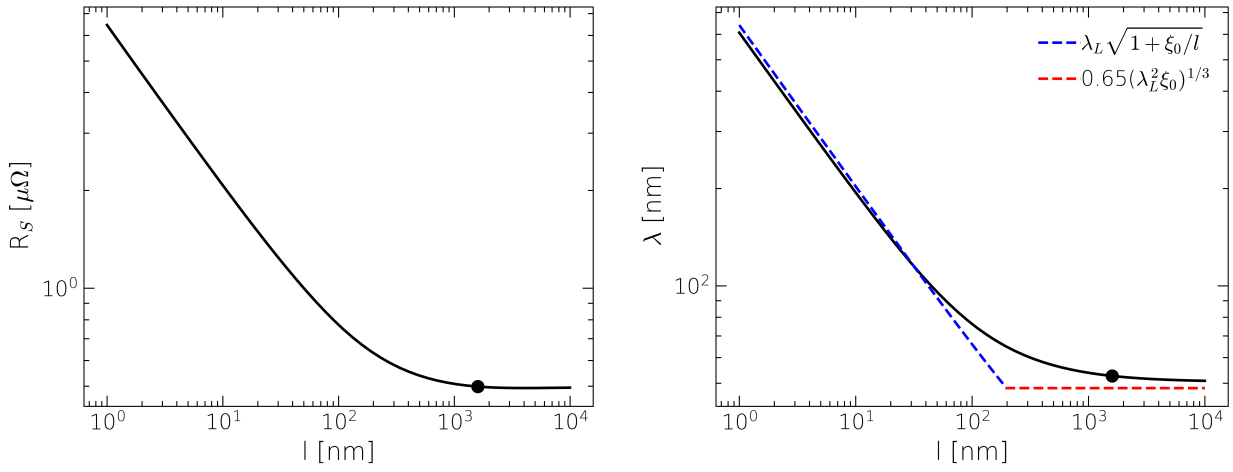

(a) (b)

Figure 2.9: (a) The surface resistance and (b) the effective penetration depth as a function of mean free path of bulk Al at 300mK and 5GHz. The dashed lines are the empirical values of penetration depth for dirty(blue) and clean(red) limit as shown in Figure 2.4. The dot represents the values at intrinsic coherence length.

The figure shows that the resistance R_S decreases with increasing mean free path up to $l \approx \xi_0$, which is shown in figures as dot, and remains constant for higher mean free paths. However, when higher temperatures and frequencies are considering it can be shown that R_S increases linearly with l above $l \approx \xi_0$. Similarly, the penetration depth is shown to

decreases with increasing l and aligns well with the theoretical calculation of dirty limit penetration depth and reaches the minimum bulk value $\lambda = 0.65(\lambda_L^2 \xi_0)^{1/3}$ given by the red dashed lines.

The previous considerations of impedance were for infinitely thick films. It is important to also consider the effect of film thickness when practical applications are considered. For finite thickness and when the EM wave is incident only on one surface of the film, as shown in Figure 2.8, the surface impedance can be calculated using Maxwell's equation as [50]:

$$Z_S = \sqrt{\frac{j\omega\mu_0}{\sigma}} coth(\sqrt{j\omega\mu_0\sigma}t) \tag{2.31}$$

where t is the thickness of the film. This is valid for circuits like wide parallel-plate transmission lines, microstrip lines, waveguide or cavity walls and ground planes. For very thick film, one retrieves the Equation 2.29. On the other hand, when $t << \lambda$ the impedance is expressed as:

$$Z_S \simeq \frac{1}{\sigma t} \tag{2.32}$$

For a circuits inside a waveguide, cavities or striplines etc. the EM wave can incident on both surfaces of superconductor. Here the surface impedance changes to:

$$Z_S = \sqrt{\frac{j\omega\mu_0}{\sigma}} \left(coth(\sqrt{j\omega\mu_0\sigma}t) \pm cosech(\sqrt{j\omega\mu_0\sigma}t) \right) \tag{2.33}$$

When the incident field on both sides of the superconductor has same phase, then the terms in Equation 2.33 are additive and when the fields have opposite phase, the terms are subtractive.

All of these equations are calculated without considering the effects of the substrate [49]. Since the effect of EM wave on the substrate is negligible, the substrate contribution to surface impedance is neglected.

The loss treated in this section corresponds to the thermal quasiparticle loss in the electrodes of resonators. Therefore, the quality factor due to thermal quasiparticles will be:

$$Q_i = \frac{\omega L}{R_{\text{eff}}} = \frac{\omega L}{Re[Z_S] l_r / W} \tag{2.34}$$

where l_r and W are respectively the length and width of the resonator.

2.3 Superconducting resonator losses at low temperatures

The contribution of the thermal quasiparticles to the overall losses of a superconducting resonator becomes negligible when the temperature of the system becomes smaller than

$100mK$. Therefore, this section is dedicated to the understanding of losses in resonators at low temperatures.

2.3.1 Two level system loss

Two level systems (TLSs) are quantum mechanical systems with two discrete energy states. Physically, the parasitic TLSs responsible for loss originate from an ensemble of defects and adsorbents giving raise to absorption and dissipation of energy at the resonator frequency, due to their electric dipole interactions. The possible TLSs are the water molecules absorbed on surfaces, defects, dangling bonds, adatoms or kinks on the metal or substrate surfaces as represented in Figure 2.10a. It could also be inside the bulk of the materials like dislocations in crystals or nanovoids and defects in amorphous solids as shown in Figure 2.10b. Since more TLSs are present at the substrate interfaces as mentioned, Sapphire is the choice of substrate in this work because of its very low loss tangent ($10^{-4} - 10^{-9}$) [51].

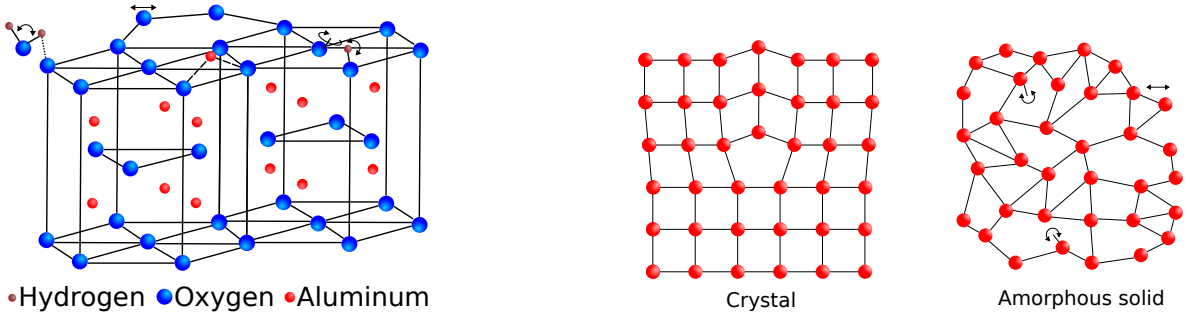

(a) (b)

Figure 2.10: Source of TLS (a) on a Sapphire substrate (from left to right: adsorbed water molecule, crystal defects or kinks, adatoms, dangling bonds and hydrogen atoms) and (b) in a crystalline (dislocation) or amorphous metal (dangling bonds, voids and loosely bound atoms shown by arrows).

The TLS can exist in two nearly degenerate configurations which are modelled by a double well potential separated by a barrier in Figure 2.11. In general, the energy landscape of any surface or bulk of a material with aperiodic lattice, are characterized by the variations of energy with uneven local minimas and barriers. When such systems have barriers which are large and have non-degenerate minimas, the tunneling of any spurious particles are severely hindered. Close to the minimas, the energy potential can be treated as isolated harmonic oscillator potentials shown V_1 and V_2 in the figure and the difference between the minimas of two potentials is given as ϵ.
But when the distance between the oscillators (d) is small and the wells are nearly degenerate with small barrier (V_0) the system can be treated as a double well with potential V. It can be seen by the bold lines in the figure. The energy associated with tunneling of

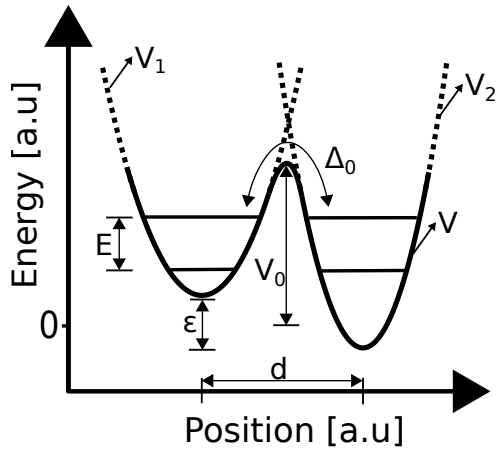

Figure 2.11: TLS model with two harmonic potentials V_1 and V_2 given in dotted lines with minimas separated by distance d and barrier V_0. With the effective potential V and the tunneling amplitude Δ_0.

the particle between the two wells is given by WKB approximation as [52]:

$$\Delta_0 = \hbar\Omega_0 e^{-kd} \text{ where } k = \sqrt{\frac{2mV_0}{\hbar^2}} \tag{2.35}$$

where m is the effective mass of the tunneling particle. By considering the tunneling of particles between the wells, the energy of the TLS is given by

$$E = \sqrt{\epsilon^2 + \Delta_0^2} \tag{2.36}$$

For a resonator with frequency ω_r, only TLSs with frequency close to the resonator frequency are excited, hence $E = \hbar\omega_r$. This phenomenon can be explained by quantum mechanics as follows:
When a photon interacts with TLS, the spurious particle (usually a polarized atom) is excited from the ground state to the excited state by changing its physical configuration. An additional photon would bring back the particle to the ground state. And as this repeats several times, the TLS looses its quantum nature since the particle occupies excited state and ground state half the time each respectively. In this case TLSs are supposedly saturated, and the number of photons required for achieving this saturation is called the critical photon number n_c.
When the TLSs are not completely saturated they also under go dissipation due to fluctuating environment around them. Therefore the dielectric carrying such TLSs are lossy. And the loss depends on the number of photons interacting with the TLS. Hence the resonators dielectric loss G is said to be dependent on the photon number. The quality

factor of resonators, considering the photon numbers is hence described as [53][54]:

$$\frac{1}{Q_i} = \frac{1}{Q_{0TLS}} \frac{tanh\left(\frac{\hbar\omega_r}{2k_bT}\right)}{\sqrt{1+(\frac{n}{n_c})^{\beta}}} + \frac{1}{Q_{other}} \tag{2.37}$$

where Q_{0TLS} is the intrinsic TLS quality factor of the resonator which is operating at temperature T, n is the applied photon number and β is the fit parameter. Q_{other} is the quality factor due to other non-TLS losses.
The theoretical graph for Q_i as a function of n and T is given in Figure 2.12 for $Q_{0TLS} = 10^4$, $f_r = 5GHz$, $n_c = 100$, $\beta = 0.5$ and $Q_{other} = 10^6$.

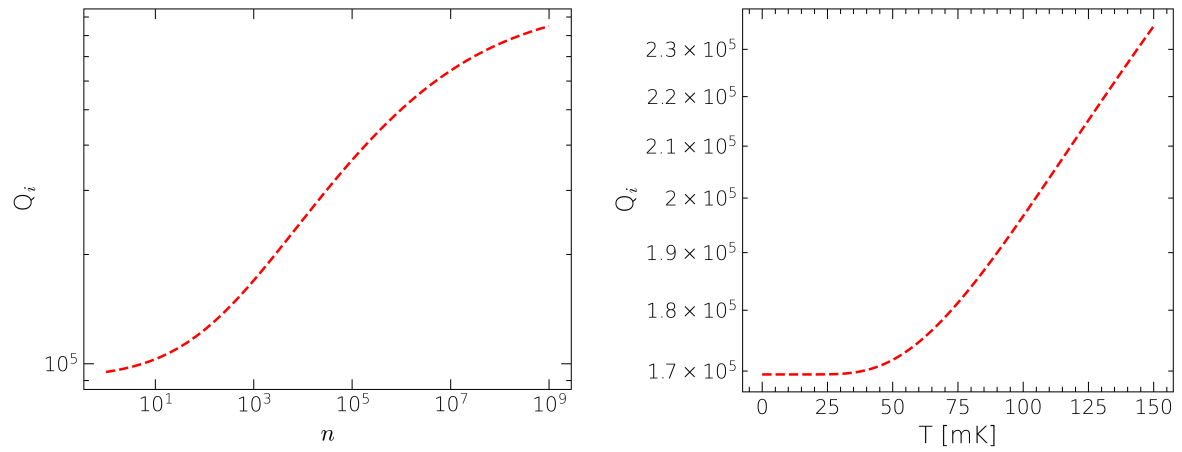

(a) (b)

Figure 2.12: TLS limited internal Quality factor (a) as a function of photon number n at temperature of $20mK$ and (b) as a function of temperature for a photon number of 1000.

When only few photons are in the resonator, the quality factor Q_i is close to the intrinsic TLS limited quality factor. With more and more photons applied, the quality factor increases. Once the photon number gets larger than critical photon number, the quality factor exponentially increases until Q_i is limited by new losses accounted in the term Q_{other}.
Q_i as a function of temperature is shown in Figure 2.12b. When temperature T is below $\hbar\omega_r/k_B$, Q_i remains constant and when $T > \hbar\omega_r/k_B$, Q_i starts to increase until contribution due to other losses such as thermal quasiparticles dominate. The increase of quality factor of resonators can be explained by the saturation of the TLSs by thermal photons.
Additionally, due to the use of waveguide, the TLS loss in resonator is reduced. This can be explained by the fact that in a 3D environment, the distribution of electric field reduces the concentration of the field close to the substrate where TLSs reside. To quantify the effects of TLS loss, LC resonators with varying capacitance are studied.

2.3.2 Ground plane loss

The resonators generally involve a ground plane. The ground planes can generate losses which reduces the quality factor of the resonator. In this section the loss originating from ground plane is discussed.

A plane EM wave enters the ground plane from the vacuum. The propagation of such waves is governed by Maxwell's equation given by:

$$\nabla^2 \vec{H} = \mu\epsilon\frac{\partial^2 \vec{H}}{\partial t^2} + \mu\sigma\frac{\partial \vec{H}}{\partial t} \text{ where } \vec{H} = \vec{H}_0 e^{-j\omega t - kz} \tag{2.38}$$

and $\vec{H}$ is the magnetic field component of the EM wave. By solving the equation, the propagation constant k is given to be:

$$k = \sqrt{j\omega\mu\sigma - \omega^2\mu\epsilon} \tag{2.39}$$

For a good metallic conductor operating in a low frequency regime (usually up to few tens of GHz) where $\sigma >> \omega\epsilon$, the second term on the right side of the above equation can be neglected and

$$k = \sqrt{j\omega\mu\sigma} = \frac{1+j}{\delta} \text{ where } \delta = \sqrt{\frac{2}{\omega\mu\sigma}} \tag{2.40}$$

where δ is called the skin depth of the conductor. It represents the distance from the surface of the metal where the EM wave amplitude exponentially decreases since $\vec{H} = \vec{H}_0 e^{-i(\omega t - z/\delta)} e^{-z/\delta}$ by substituting for k in the magnetic field. The representation of the field propagating in the metal is shown in Figure 2.13a.

For a superconductor, the propagation of magnetic field is governed by the same Maxwell's Equation 2.38 with the same propagation constant given in Equation 2.39. However, the conductivity is complex for the superconductor as it is discussed in the previous section. Hence for a superconductor operating at low frequencies in the GHz regime, the propagation constant is given by:

$$k = \sqrt{j\omega\mu(\sigma_1 - j\sigma_2)} \tag{2.41}$$

At low temperatures the conductivity due to quasiparticles is negligible i.e. $\sigma_1 \simeq 0$. By solving for σ in equation 2.29 and 2.30 one obtains $\sigma_2 = 1/\omega\mu\lambda^2$ and substituting σ_2 in 2.41 gives

$$k = \frac{1}{\lambda} \tag{2.42}$$

Therefore the field inside the superconductor is $\vec{H} = \vec{H}_0 e^{-i\omega t} e^{-z/\lambda}$. The representation of the field inside the ground plane materials is shown in Figure 2.13b.

The surface resistance R_{gnd} due to the bulk ground plane is governed by Equation 2.27,

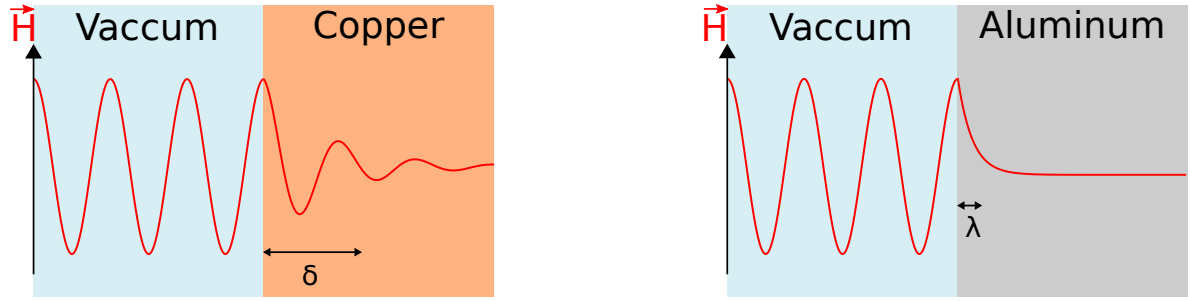

(a) (b)

Figure 2.13: EM wave propagation (a) in a metal like Copper with skin depth δ and (b) in a superconductor like Aluminum with penetration depth (λ).

and is given as

$$\begin{aligned} R_{gnd} &= \frac{1}{\sigma\delta} \text{ for a metal} \\ &= Re\left[\frac{1}{\sigma\lambda}\right] \simeq \frac{\sigma_1}{\sigma_2^2\lambda} \text{ for a superconductor} \end{aligned} \tag{2.43}$$

Therefore, the quality factor due to ground plane is given by

$$Q_i = \frac{\omega L}{R_{gnd}} \tag{2.44}$$

Hence to comparatively study the effect of ground plane loss two waveguides are used for the resonators measurement.

2.3.3 Excess quasiparticle loss

Along with the equilibrium quasiparticles explored before, there might exist out of equilibrium quasiparticles which are not taken into account by the Mattis Bardeen theory. The origin of such excess quasiparticles is still debatable. Their density is large in superconductors with rough surfaces, localized surface states and smaller grain size [55] which could be attributed to potential barriers at surface edges which enhances creation of quasiparticles.

These defects could introduce non-zero subgap states. This was explained first by Dynes [56]. The equation of density of states for the quasiparticles is given as

$$\frac{N_S(0)}{N} = \frac{(E - j\Gamma)}{\sqrt{(E - j\Gamma)^2 - \Delta^2}} \tag{2.45}$$

This is called the Dynes formula and Γ is the Dynes parameter defined as the inverse quasiparticle lifetime. When this parameter is zero, there are no states within the superconducting gap, however superconductors could have subgap states observed by a finite Dynes parameter in the literature [57][58]. Figure 2.14 shows the residual subgap density

of states for an example where Γ is 5% of the superconducting gap Δ.

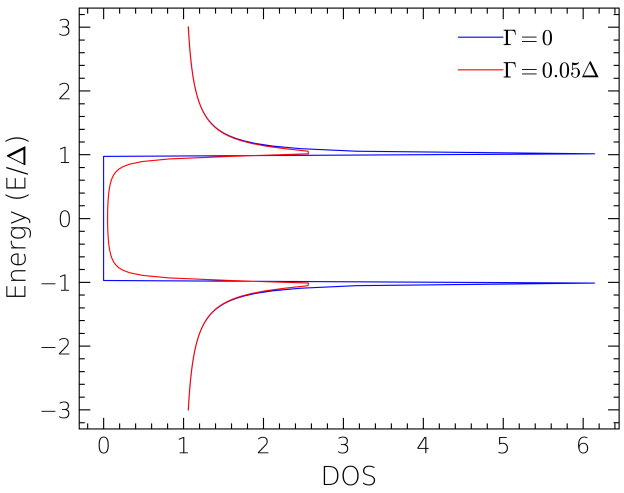

Figure 2.14: Normalized DOS for Dynes superconductor where the blue curves is for a normal superconductor and the red curves is for a Dynes superconductor with $\Gamma = 0.05\Delta$.

The surface resistance due to excess quasiparticle in an infinitely thick film is given by [55]:

$$R_{excess} \simeq \frac{\mu_0^2 \omega^2 \lambda^3 \sigma_n \Gamma}{\Delta} \tag{2.46}$$

Excess quasiparticle study involves interactions between TLS of the dielectrics with electrons in superconductors [59]. It is also shown to be generated by Cosmic rays [60].

2.3.4 Radiation loss

Any device which interacts with EM waves can under go radiation loss. A resonator can act like a source of radiation when the phase velocity in the resonator exceeds the phase velocity in the substrate or vaccum. The difference in velocity creates shockwaves of radiation in a slow velocity medium. In other words, the radiation diffuses as refracted waves into the smaller refractive index medium. The phase velocity of the EM wave in a medium is given by:

$$v_P = \omega/k \tag{2.47}$$

For low frequencies, the propagation constant for a superconductor is given by $k = 1/\lambda$. The quantity for a dielectric is given to be $k = \omega\sqrt{\epsilon_{eff}}/c$ since $\epsilon = \epsilon_0\epsilon_{eff}$. The phase velocity in a superconducting medium is given as:

$$v_{PS} = \omega\lambda \text{ for Superconductor} \tag{2.48}$$

Similarly, the phase velocity of EM wave in a dielectric is given by:

$$v_{PD} = \frac{1}{\sqrt{\mu\epsilon}} = \frac{c}{\sqrt{\epsilon_{eff}}} \text{ for Dielectric} \tag{2.49}$$

For a resonator in a waveguide $\epsilon_{eff} \approx 1$. The phase velocity in the superconductor ($\sim 10ms^{-1}$) is much smaller than the one of the substrate ($\sim 10^6 ms^{-1}$), hence radiation loss from the superconductor is negligible. Since the frequency of the resonators are in GHz regime in this work, the radiation loss is insignificant.

2.3.5 AC heat loss

The next important loss originates from the alternating EM field. This is dominating when the field amplitude is high. There are multiple reasons given for this occurrence. Firstly, with strong EM field, the peak amplitude of magnetic field of the signal could be larger than the critical magnetic field of the superconductor [61] creating superconducting state to stay in Meissner state with heat generating vortices.
Secondly, the surface temperature increases due to RF heating even below the critical field, causing thermal feedback due to heat radiation further increasing the surface temperature of the superconductor [62]. This is another source of quasiparticles. Hence the resistance R_{eff} depends on photon number in the large field limit as mentioned in the beginning of the chapter.

Chapter 3

Design, Fabrication and Setup

The chapter is composed of three parts. The first part discusses the design of the resonators and the waveguide. It is followed by the fabrication processes of the resonators of different thicknesses. Finally, the setup used for the measurements of the resonators at low temperatures is explained.

3.1 Device design

The device under consideration involves superconducting Al half-wavelength transmission line resonator fabricated on a Sapphire substrate. However, the resonator in this work is not truly half-wavelength transmission line due to additional capacitance and meander lines (which provide additional mutual inductance.) The SEM image of the resonator is shown in Figure 3.1a.

The resonators are excited by coupling them to a waveguide port. Waveguide is a device that confines the propagation of EM waves in a particular direction. In this case, a rectangular waveguide is considered for the propagation of the waves. The waveguide terminates in a short circuit, making it a single port device. There are six resonators with various capacitances on the substrate. This sample is placed within the waveguide as seen in Figure 3.1b, together with the waveguide's lid. The lid acts as the short circuit termination.

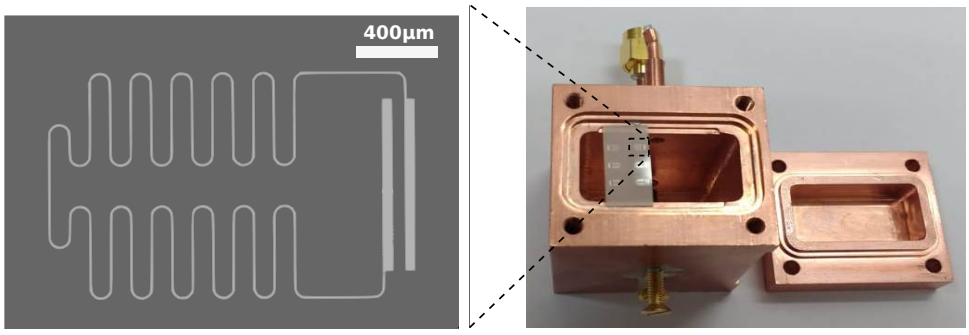

(a) (b)

Figure 3.1: (a) SEM image of a resonator of Sample A. (b) Sample picture with six resonators in a Copper waveguide.

3.1.1 Waveguide simulation with HFSS

Waveguides are realized with the help of simulations. The modes of the waveguide are analytically defined by its dimensions. The dominant mode of wave propagation is TE_{10}. The cut-off frequency of the waveguide is given as $f = 1/(2a\sqrt{\mu\epsilon})$ where a is the width of the waveguide. However, for better estimates of the modes and cut-off frequency of the waveguide simulation using HFSS software is performed. HFSS follows finite element modelling for Maxwells equation where the eigenmodes and excitation of a structure can be simulated.

Figures 3.2a and 3.2b, shows the side and front view of the waveguide designed respectively. Waveguide is excited by transmitting signal to the Port. The signal then propagates within the waveguide. The waveguide has double screws which can be tuned to change the effective capacitance. As a consequence, any impedance mismatch and hence return loss can be tuned.

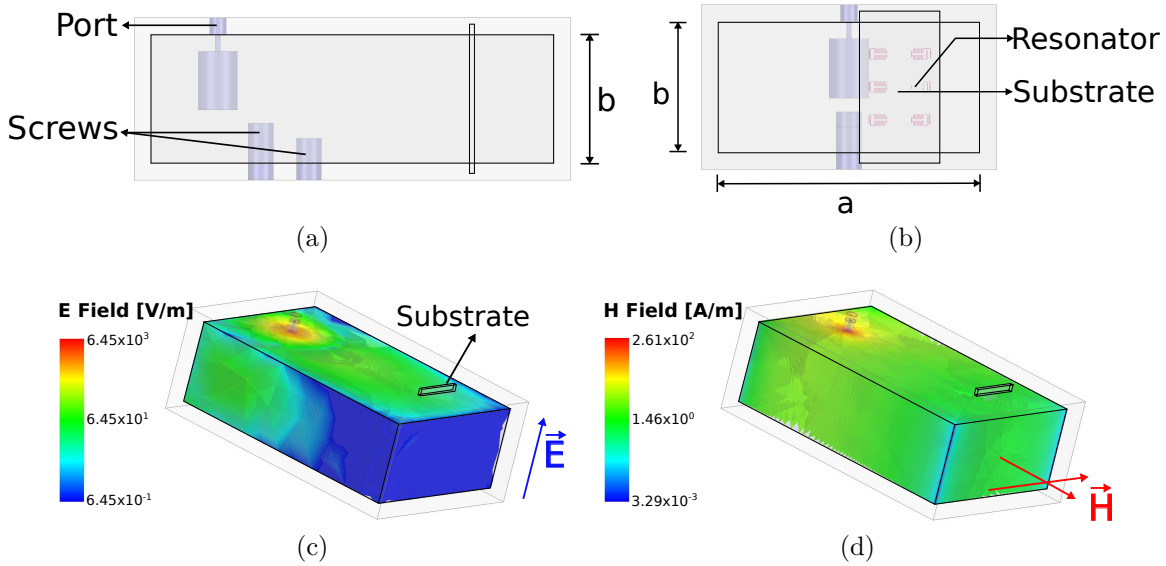

Figure 3.2: (a) Side view and (b) Front view of simulated waveguide design with the positions of stub to excite the waveguide and impedance tuning screws and substrate with resonators are shown. (c) Electric and (d) magnetic field distribution inside waveguide simulated at 5GHz. The direction of fields on the substrate is given by blue and red arrows.

The field distribution of EM waves inside the waveguide is shown by simulated field amplitudes in Figure 3.2c and 3.2d for a frequency of 5GHz. The colours in figures represents the amplitude of the electric and magnetic fields. This simulation shows that the signal amplitude is larger close to the port and that it drops exponentially away from it. These are known as the evanescent waves.

The position of the substrate with resonators is approximately 1cm away from the far end of the waveguide as shown in Figure 3.2a. The substrate is close to the node of the

evanescent waves. Therefore the coupling of the resonator to the waveguide is weak. The cut-off frequency from the simulation was found to be $6.2GHz$.
Above this frequency the signal inside the waveguide is transmitted to the short circuit load. In other words, the EM wavepropagates through the waveguide. This creates the resonators with frequencies larger than cut-off frequency to be overcoupled to the waveguide. Secondly, above the cut-off frequency, the reflected signal drops significantly making the measurement of the resonators harder.

3.1.2 Resonator design and Inductance calculation

The resonators are designed with frequencies below $6.2GHz$ using HFSS software. The resonators chosen is a meandered half wavelength transmission line resonator. There are six resonators designed with different capacitance gaps in order to understand the effect of dielectric loss. The frequency of the resonators are obtained by eigenmode simulation with HFSS. The electric field distribution in one of the resonators simulated is shown in Figure 3.3. The amplitude of the field is high close to the capacitor edges of the resonators.

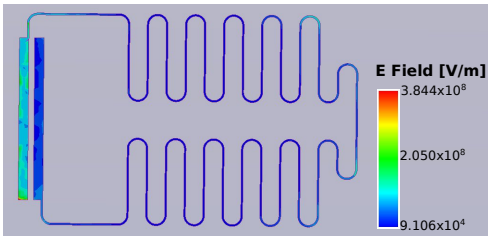

Figure 3.3: Simulation of electric field distribution inside a $30\mu m$ capacitance gap resonator

Capacitance gap [μm]	Frequency [GHz]
30	4.665
60	4.951
90	5.117
140	5.263
210	5.374
300	5.536

Table 3.1: Values of capacitance gaps and resonator frequency

The results of simulated resonances of a perfectly conducting resonator with different capacitance gaps is given in the Table 3.1. The resonances of the resonators are achieved to be below the cut-off frequency.
On a side note, instead of a perfectly conducting surface, if one considers an impedance in the simulation of the resonator, the eigenfrequency of the resonators change. By tuning the impedance in the simulation, the frequency is changed to the frequency of the resonators measured during the experiments. This impedance can be considered to recognize the value of kinetic inductance of the superconductor used.

3.1.3 Properties of waveguide realized

Two waveguides are manufactured by machining technique in Neel Institute. One is made out of Cooper and the other is made out of Aluminum. These waveguides are used for

comparative study of the ground plane loss. In Figure 3.4a, these two waveguides without their respective covering lids are attached. In this configuration, a microwave signal is sent through the ports of waveguides. The corresponding measurements of the waveguides forward transmission coefficient (S_{21}) and input reflection coefficient (S_{11}) as a function of frequency are shown in Figure 3.4b by red and blue colors respectively.

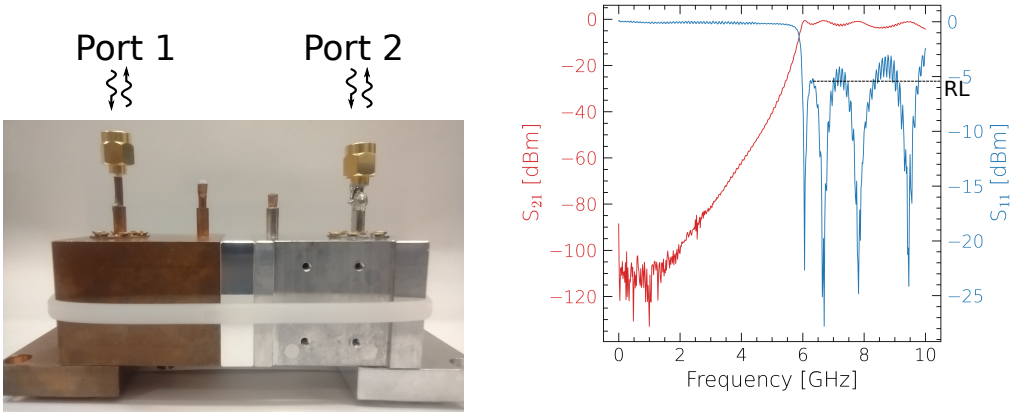

(a) (b)

Figure 3.4: (a) Picture of two waveguides connected together to perform transmission and reflection measurements and (b) the transmission (red) and reflection (blue) coefficient measurements as a function of frequency at room temperature and RL is the return loss of the waveguide.

By sweeping the frequency of the VNA, the cut-off frequency of the waveguide is obtained to be around $5.9GHz$ from the transmission coefficient measurements. Below the cut-off frequency, the transmission in the waveguide reduces exponentially. The waveguide reflects most of the signal back below the cut-off frequency. This can be seen in above Figure 3.4b where S_{11} is $0dBm$ in the blue curve below $6GHz$. The resonators are hence designed in this frequency region.
Above $5.9GHz$, the transmission coefficient is close to $0dBm$ and the reflection coefficient reduces to about $-5dBm$ to $-6dBm$ close to $6GHz$. It shows four inverted peaks between 6 and $10GHz$. These are the hybridized resonance peaks of the two waveguides connected together. Due to hybridization the dominant mode frequency is not exactly $6.2GHz$, but 5.9 and $6.6GHz$. Similarly for the higher mode instead of $8.6GHz$ there are two inverted peaks. The return loss is labelled as RL in the figure. The reflection coefficient which defines the return loss can be reduced to further by fine tuning of the screws.

3.2 Fabrication of resonators

Resonators are fabricated after the characterization of the waveguide. To understand the effect of electron mean free path on the quality factor one has to make samples of different

thicknesses and with different qualities. To achieve this, the fabrication is done with two different methods of the so called top-down approach. One is the lift-off method and the other one is the etching method. The recipe and details of fabrication is given in the next sub-sections. There are six samples fabricated and measured. So the naming convention chosen is by alphabets i.e. A to F.

3.2.1 Fabrication by lift-off method

In this technique, a pattern is designed on a photoresist deposited on the substrate. After making the pattern, metal deposition is performed. As a rule of thumb, this technique is suitable for depositions with thickness less than five times the resist thickness. Before describing the recipes, the processes used in this method are explained.
There are four samples (A, B, D and F) made by this approach. The process used for fabricating the four samples are the same except when specified explicitly. The recipes of all samples made by lift-off method are given in the Table 3.2. The details of the processes are listed below:

1. **Cleaning**: The Sapphire substrate chip is cleaned by placing the substrate in a solution with RBS-10% and deionized (DI) water with 1:10 ratio in ultrasonic bath for 10 minutes to remove dirt. Any grease or glue residues are removed by cleaning in acetone for 5 minutes in ultrasonic bath, followed by 5 minutes in ethanol and a rinse in IPA. Then the substrate is blow dried with N_2 gas.

2. **Spin coating**: The photoresist is deposited on the substrate by spin coating. The spin coater used is SPIN150 Polos. The thickness of the photoresist depends on the viscosity of the resist and the speed and time of spin. Different resists and spin speed have been used to achieve required thickness. The schematic is given in Figure 3.5a where the grey region is the Sapphire substrate and red region is the photoresist. Spin coating produces edge beads which refer to an increase in the resist thickness on the edges of the substrate. Hence resonator pattern needs to be situated away from the edges of the substrate. This condition is satisfied in the fabrication of the sample since the substrate has an area of $15\times15\text{mm}^2$ and the pattern covers an area smaller than $10\times10\text{mm}^2$.

3. **Exposure**: This is a process of exposing resist to light (in this work) or electrons or ions with or without mask to make a pattern. The resist is exposed to light of certain wavelength to change resist properties chemically to react with developers (bases or solvents). In this work, LASER is used as the light source for patterning. The pattern is designed with KLayout, a GDS design software and the pattern file is fed to the lithography machine. In the schematic 3.5b, the LASER is represented by blue color. The LASER is turned on in the region which needs to be patterned.

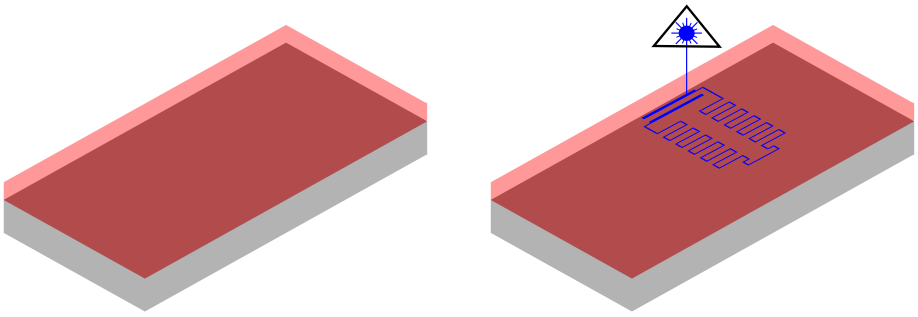

(a) (b)

Figure 3.5: (a)Spin coating and (b) LASER lithography where the dark grey layer represents the Sapphire substrate and the the red layer is the photoresist.

The lithography machine used is from Heidelberg DWL66FS with the LASER of 405nm wavelength.

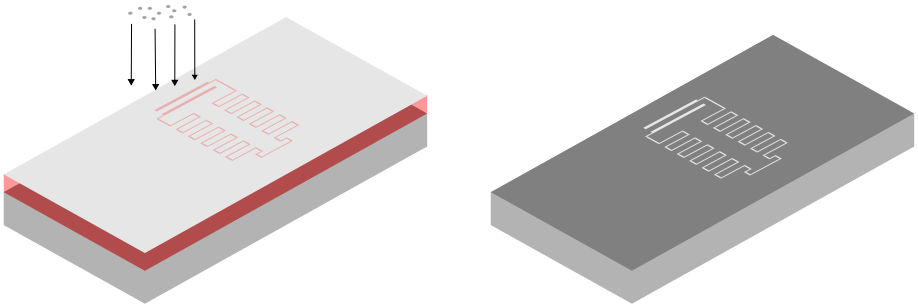

(a) (b)

Figure 3.6: (a)Evaporation and (b) lift off where the light grey layer represents evaporated Aluminum.

4. **Development**: This is a process of removing the exposed pattern. When a positive photoresist is used, as in this case, the region exposed to light will get dissolved. Otherwise, when a negative photoresist is considered, it remains inherent to the radiation.
   The sample later is cleaned with running DI water to remove residue of developers, followed by blow dry with N_2. The sample is cleaned in O_2 plasma with 20W RF power for 2 minutes to remove any residue of resist on the substrate before the next process.

5. **Evaporation**: This is a Physical vapour deposition(PVD) mechanism for metal deposition. Metal is heated to vapor phase by e-beam leading to its deposition on the substrate. For the four samples, four different conditions are used. The chamber pressure is maintained below 10^{-6}mbar so that the distance between collisions of atoms in the chamber is large in this case $\sim$ 10km [63]. Therefore the chances of collision of atoms coming from the crucible with the gas atoms in the chamber is

very low. On the other hand, if the chamber is not pumped for longer duration or the substrate is not heated, the gaseous atoms on the substrate are not pumped out of the chamber. Hence, metal atoms increasingly interact with the atoms of gases on the surface of substrate. This changes the quality and hence the mean free path of the material.

The schematic of evaporation is shown in Figure 3.6a. The atoms represented as grey dots travel in straight lines from crucible to sample shown by arrows. The evaporations are done at PTA and Neel Institute in Plassys evaporators.

6. **Lift-off**: This is a process of removing all the metal deposited on the resist. After lift-off only the metal deposited on the substrate remains, leading to the final circuit pattern. The sample after evaporation is put in a solvent bath which dissolves the resist. The metal on top of the resist is lifted off from the sample substrate ending with only pattern left on the substrate as shown in Figure 3.6b. The sample is then cleaned with IPA and blow dry with N_2 gas. The sample is also cleaned with O_2 plasma in RIE with 10W power for 2 minutes.

There are two sub methods used for fabrication in lift-off technique as shown in Figure 3.7. Sample A and B are prepared with one layer of resist represented as a red layer in Figure 3.7a. The grey color represents Al and dark grey region is the Sapphire substrate. Sample D and F are made with two layers of resist as reported in Figure 3.7b where the bottom Lift-off resist(LOR) is shown in green. The details are given in the recipe.

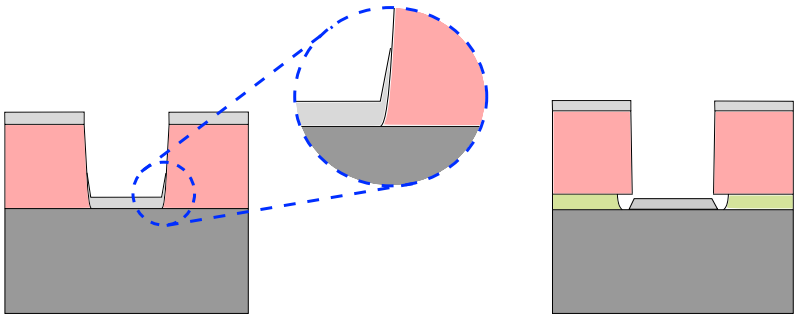

Figure 3.7: Representation of sample after evaporation of Al films (a) without and (b) with Lift off resist (LOR) shown as green layer. Films are deposited on the resist walls shown as red layer in sample without LOR.

When a positive resist is exposed to the LASER, there would be an underexposure at the lower part of the resist which results in not having a straight pattern or an undercut. The atoms when evaporated will deposit on the walls of the resist as highlighted in the Figure 3.7a which is connected to the film on the substrate. However when the LOR is used, the resist creates an undercut breaking the deposition of atoms on the wall and film on the substrate. The AFM images later shown will detail these phenomena.

Process name	Sample	Equipment	Precision
Substrate bake	A	Hot plate	200°C, 4minutes
	B		
	D		
	F		
Spin coating 1	A	S1818	4000rpm, 30s (Achieved thickness:1.5μm)
	B		
	D	LOR-3A	4000rpm, 30s (Achieved thickness:0.2μm)
	F		1000rpm, 30s (Achieved thickness:0.6μm)
Bake 1	A	Hot plate	115°C, 1 minute
	B		
	D		200°C, 2 minutes
	F		200°C, 2 minutes 30 seconds
Spin coating 2	A	-	-
	B		
	D	S1818	4000rpm, 30s (Achieved thickness:1.5μm)
	F	AZ4562	4000rpm, 30s (Achieved thickness:6μm)
Bake 2	A	-	-
	B		
	D	Hot plate	115°C, 1 minute
	F		100°C, 1 minute 30 seconds
Lithography	A	DWL66FS	72% of 30% filtered LASER source
	B		
	D		
	F		
Development	A	Developer	Microposit developer and DI water with 1:1 ratio for 1minute
	B		
	D		Microposit developer for 1minute
	F		MF826 developer for 1minute
Evaporation	A	Plassys MEB550	59nm at 0.1nms^{-1} with 5×10^{-7}mbar
	B		52nm at 0.1nms^{-1} with 3.5×10^{-8}mbar
	D	Plassys Suprafab	68nm at 0.1nms^{-1} with 3.5×10^{-8}mbar
	F		588nm at 0.5nm^{-1} with 3.5×10^{-8}mbar
Lift off	A	Solvents	10minutes in acetone
	B		
	D		
	F		

Table 3.2: Recipe for resonators with lift-off method

3.2.2 Fabrication by etching method

Fabrication can be done also by carving out a pattern from an extended film deposited on the substrate. This is also known as etching. Etching can be done by reactive ions created by plasma, this process is known as reactive ion etching (RIE). When it is be performed by acids and bases, it is instead called wet etching. The two samples C and E, are fabricated by wet etching.

1. The substrate is cleaned as described in the previous section.

2. **Deposition**: Sample C, is evaporated and sample E, is sputter deposited. The evaporation process was already discussed in the previous section. Therefore, only the sputtering process is discussed here.
   The sputtering is done by Ar^+ ion plasma hitting the metal target with energy greater than disassociation energy of the metal atoms. The disassociated metal atoms moves outwards and condensates on substrate as shown schematically in Figure 3.8. The sputtering is isotropic and this is schematically shown by the direction of arrows representing the motion of atoms given as grey dots in the figure.

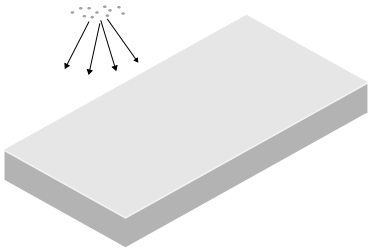

Figure 3.8: Sputtering of Al represented by light grey where motion of atoms are shown by the arrows.

Sample E is sputtered because the thickness achievable by sputtering is large. In evaporation as a rule of thumb the thickness allowed is 600nm. This is because of the heating of the crucible with time. Longer the crucible is heated, larger is the chance of damaging the evaporator machine.
Sputtering was done initially in Neel Institute, CNRS in a chamber which was meant for magnetic material sputtering. But due to magnetic impurities, the samples were obtained from IRAM from Eduard Driessen's group, where there are no other materials sputtered apart from Al and Titanium (Ti) in the chamber.
The purity of the two sputtered samples were determined by Energy-Dispersive X-ray spectroscopy (EDX). EDX is a technique used for characterizing the elements present in a sample. The film is exposed to high energy of electron beam which creates a vacancy in the inner shells of the atoms for a higher shell electron to occupy. The maximum energy of electron beam applied is 20keV. This generates X-ray radiation at energies less than 20keV depending on the elements and shells of the atoms. The number of counts of such radiation per second per eV of energy as a function of energy of radiation is shown in Figure 3.9. The table in the inset of the figures reflects the contents of the elements present in the particular film.
The sputtering chamber in Neel Institute was covered with magnetic materials which could decrease the purity of Al. Hence, precaution was taken to cover the chamber by sputtering 10μm of Al before beginning deposition on the sample. As it can be seen in the table of Figure 3.9a, even after covering chamber with Al before

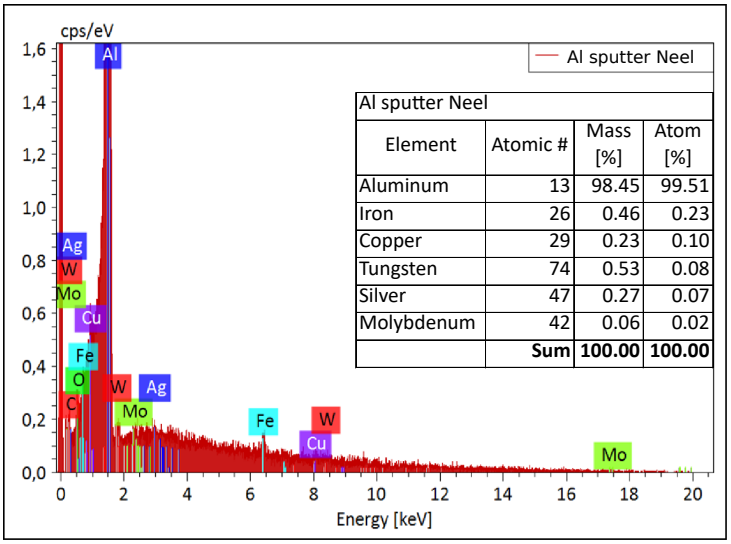

Al sputter Neel

Element	Atomic #	Mass [%]	Atom [%]
Aluminum	13	98.45	99.51
Iron	26	0.46	0.23
Copper	29	0.23	0.10
Tungsten	74	0.53	0.08
Silver	47	0.27	0.07
Molybdenum	42	0.06	0.02
	Sum	**100.00**	**100.00**

(a)

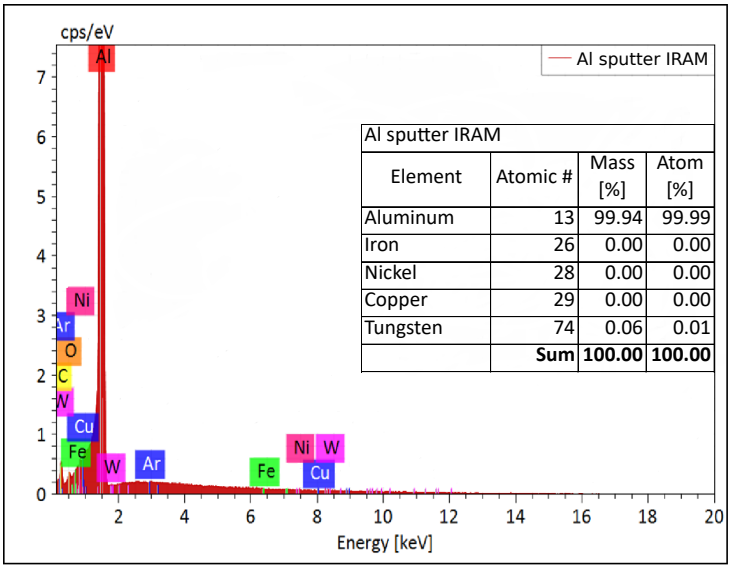

Al sputter IRAM

Element	Atomic #	Mass [%]	Atom [%]
Aluminum	13	99.94	99.99
Iron	26	0.00	0.00
Nickel	28	0.00	0.00
Copper	29	0.00	0.00
Tungsten	74	0.06	0.01
	Sum	**100.00**	**100.00**

(b)

Figure 3.9: EDX graphs of sputtered films and element table for sample from (a) Neel Institute and (b) IRAM

the deposition, there is still significant amount of impurities such as Iron, Copper and Silver. On the other hand, in the IRAM sample there are no other materials reducing the purity of Al deposited apart from a small amount of Tungsten as seen in table of Figure 3.9b reulting 99.99% pure Al.

3. **Spin coating**: The sample is spincoated with photoresist. The main purpose of the resist is to mask the metal from being etched. The red layer in Figure 3.10a represent the photoresist spin coated on substrate with Al film.

4. **Exposure**: Exposure is performed in inverted mode since positive resist is used. This is achieved by exposing all the regions on the sample except the pattern as

shown in Figure 3.10b where blue color on the sample represents the area of sample exposed to LASER.

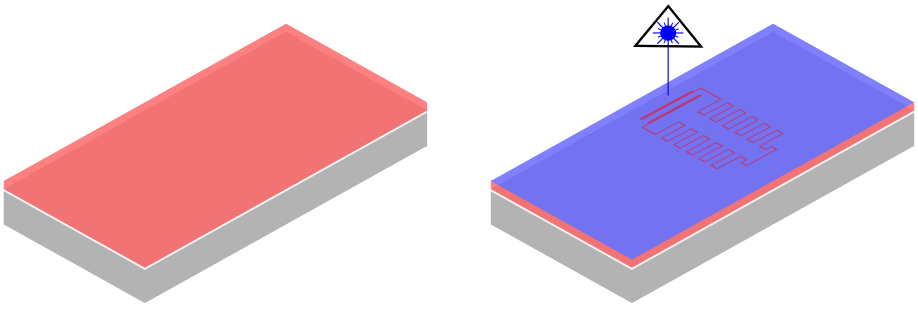

(a) (b)

Figure 3.10: Representation of (a) spin coating and (b) lithography process where the dark grey layer is the Sapphire substrate, the red layer is the photoresist, light grey layer represents Al and blue color represents the light exposed region.

5. **Development**: This procedure remains the same as before. The pictorial representation after development is shown in Figure 3.11a.

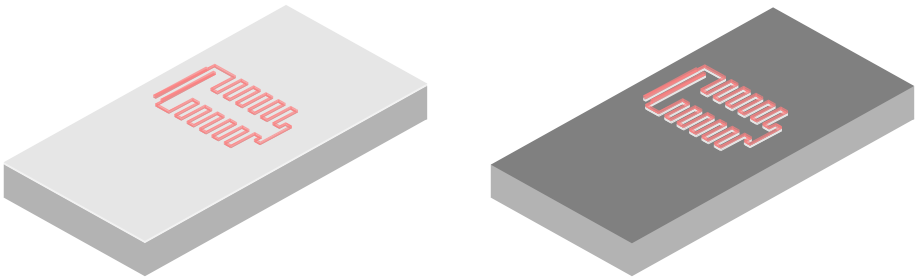

(a) (b)

Figure 3.11: Representation of (a) development and (b) etching process.

6. **Etching**: This is the process of removing unprotected material. In wet etching, unprotected region of metal is dissolved by etchants. In this case the etchant is a commercially available Aluminum etchant Type D which is an acid mixture with an etch rate of $4nm.s^{-1}$. After the etching process, the samples are cleaned with DI water and blow dried with N_2 gas.

7. **Cleaning**: It is done by acetone which removes resist mask. Later, the sample is rinsed in IPA and blow dried with N_2. To remove any resist residues, the sample is cleaned with O_2 plasma with 10W power in RIE for 2minutes.

The recipes of samples made by etching method are given in the Table 3.3 below.
It is observed that, the etching takes longer time than the calculated time. This is most probably due to presence of native oxide, which is etched at much slower rate.

Process name	Sample	Equipment	Precision
Deposition	C	Plassys MEB550	Evaporation: 53nm at 0.1nms^{-1} with 3.5×10^{-8}mbar
	E	IRAM	Sputtering: 2.7μm at 0.5nms^{-1} with 2.3×10^{-7}mbar
Spin coating	C	S1818	4000rpm, 30s (Achieved thickness:1.5μm)
	E		
Bake	C	Hot plate	115°C, 1min
	E		
Lithography	C	DWL66FS	72% of 30% filtered LASER source
	E		
Development	C	Developer	Microposit developer and DI water with 1:1 ratio for 1minute
	E		
Etching	C	Al etchant Type D	etch time: 18-20 minutes
	E		etch time: 50-55 minutes
Resist removal	C	Solvent	2minutes in acetone
	E		

Table 3.3: Recipe for resonators with etching method

I also tried dry etching on some thick film samples of 2.7μm with ICP-RIE using Cl_2 and HBr gases. This is a process of both reactive chemical and physical etching. The sample is bombarded with high energy ions due to inductively coupling of plasma to physically etch the material and the ions also react with the material to be etched. But due to time constrain the recipe could not be optimized and hence there is no sample made from dry etching.

3.2.3 Characterization

The samples are characterized by Atomic Force Microscopy (AFM) in non-contact mode with help from Simon Le Denmat of Neel Institute. The thickness and surface morphology is measured with high resolution in an area of $20 \times 10\mu m^2$ of each resonator film.
The AFM image of the samples A and B are given in Figure 3.12. The images are color

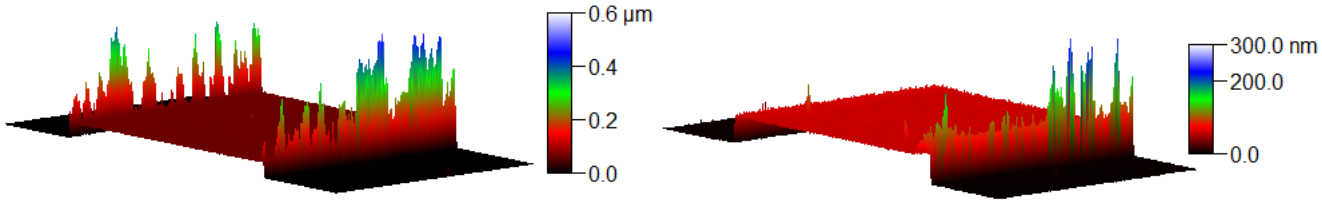

(a) (b)

Figure 3.12: The AFM images of sample (a) A and (b) B. The thickness is color coded with black is 0nm and white is the corresponding highest value of the scale.

scaled and the thickness is calculated by taking the average height of the resonator. Sam-

ple A has a thickness of 59nm and on the edges it has whiskers of Al with a height of about 450nm. The whiskers are present on both edges of the resonator. Sample B has a thickness of 52nm and has whiskers only on one edge of the resonator with a heightof less than 200nm. This could create additional losses as it will be discussed in chapter 4. The presence of the whiskers are attributed to the single layered resist process.

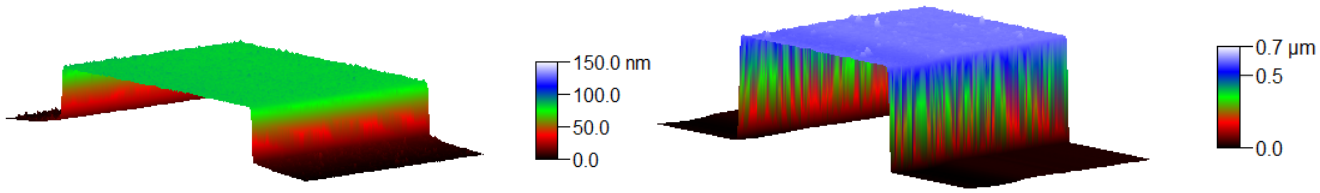

(a) (b)

Figure 3.13: The AFM images of sample (a) D and (b) F. The thickness is color coded with black is 0nm and white is the corresponding highest value of the scale.

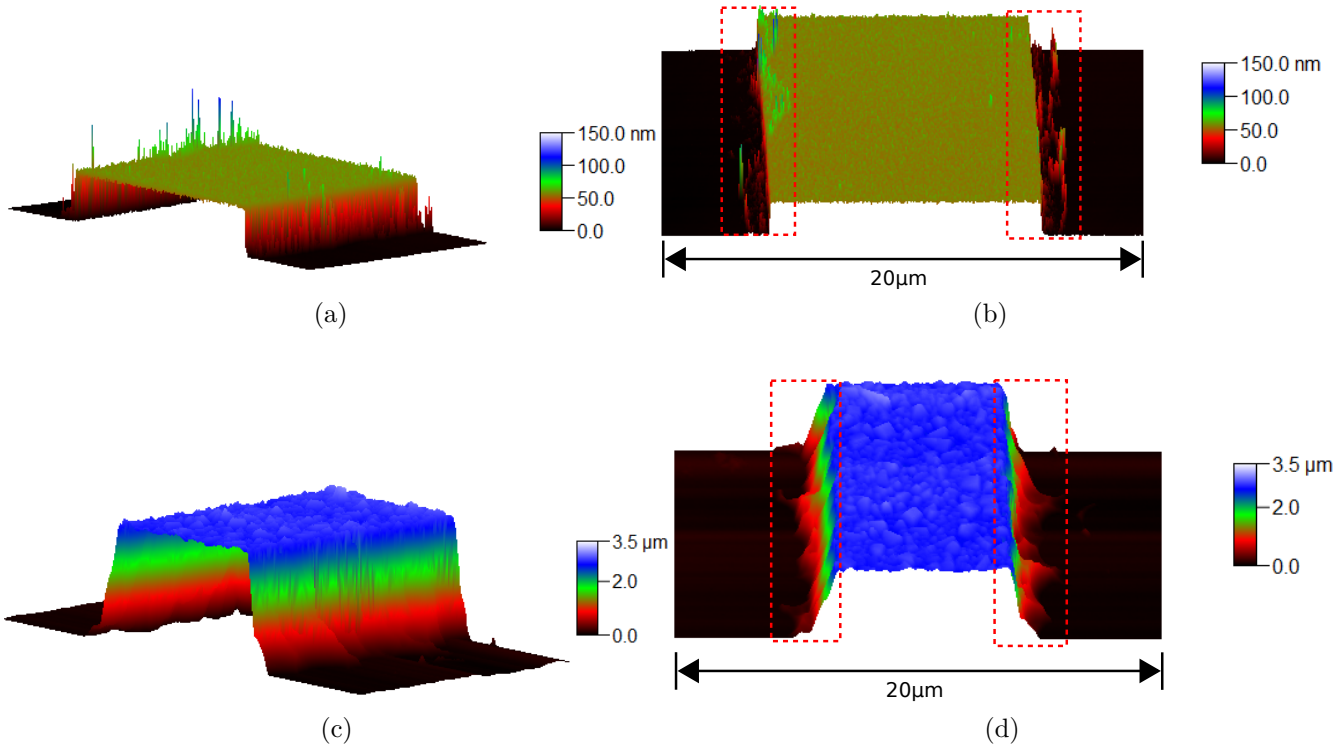

(a) (b)

(c) (d)

Figure 3.14: The AFM images of samples angular and top rotated view of (a), (b) sample C and (c), (d) sample E respectively.

Instead, sample D and F are made with two layers of resist. The thickness of the samples are 68nm and 588nm respectively. It can be seen in Figure 3.13 that there are no more whiskers in such resonator films. This is the first time a bilayer resist is used for fabricating a thick film in my group. Furthermore, there are no whiskers observed from the

AFM measurements. Therefore, it can be concluded that bilayer resists are good to avoid whiskers.
Sample C and E were fabricated by wet etching process. The thickness of sample C ad E are 53nm and 2705nm respectively. Residues from chemical reaction between Al and etchants on the edges of the film in Figure 3.14b are highlighted by dotted red boxes. This causes large losses in resonators as it will be seen in the chapter 4. The rough sides due to uneven etching of Al in sample E is observed in Figure 3.14d.
The average width of Sample E is $9\mu m$ which is smaller compared to other films with the width of $\simeq 11\mu m$. This change in the width is due to isotropic etching of the acid. Hence the top surface width is smaller than the bottom surface width.
In conclusion, different methods were used in fabricating the samples. A novel method of obtaining thick film using bilayer resist is shown and the etching process for thick film pattern realization is discussed.

3.2.4 Surface roughness

Roughness of a metal reportedly influences the quality of the film. Therefore the samples are also scanned for roughness in an area of $2 \times 2\mu m^2$ on the top surface of the resonators in the non-contact mode with higher resolution. Gwyddion software is used to analyze the data of roughness obtained from the measurements. The surfaces of all samples are shown in Figure 3.15.
For thin films with low deposition rate, the grain size is small. For thick films with large deposition rate, the grain size is large. The sputtered sample has the largest grain size of about 600nm and hence the largest roughness. The thin films roughness range from 1-3nm which could reduce diffuse scattering of quasiparticles. The roughness of the samples along with their thicknesses, deposition rate and fabrication methods are given in the Table 3.4.

Sample name	Fabrication	Thickness [nm]	Deposition rate [nms^{-1}]	Roughness [nm]
A	Lift-off	59	0.1	1.13
B	Lift-off	52	0.1	1.81
C	Etching	53	0.1	2.6
D	Lift-off	68	0.1	0.97
E	Etching	2705	0.5	47
F	Lift-off	588	0.5	3.13

Table 3.4: Table summarizing different sample thickness and their roughness

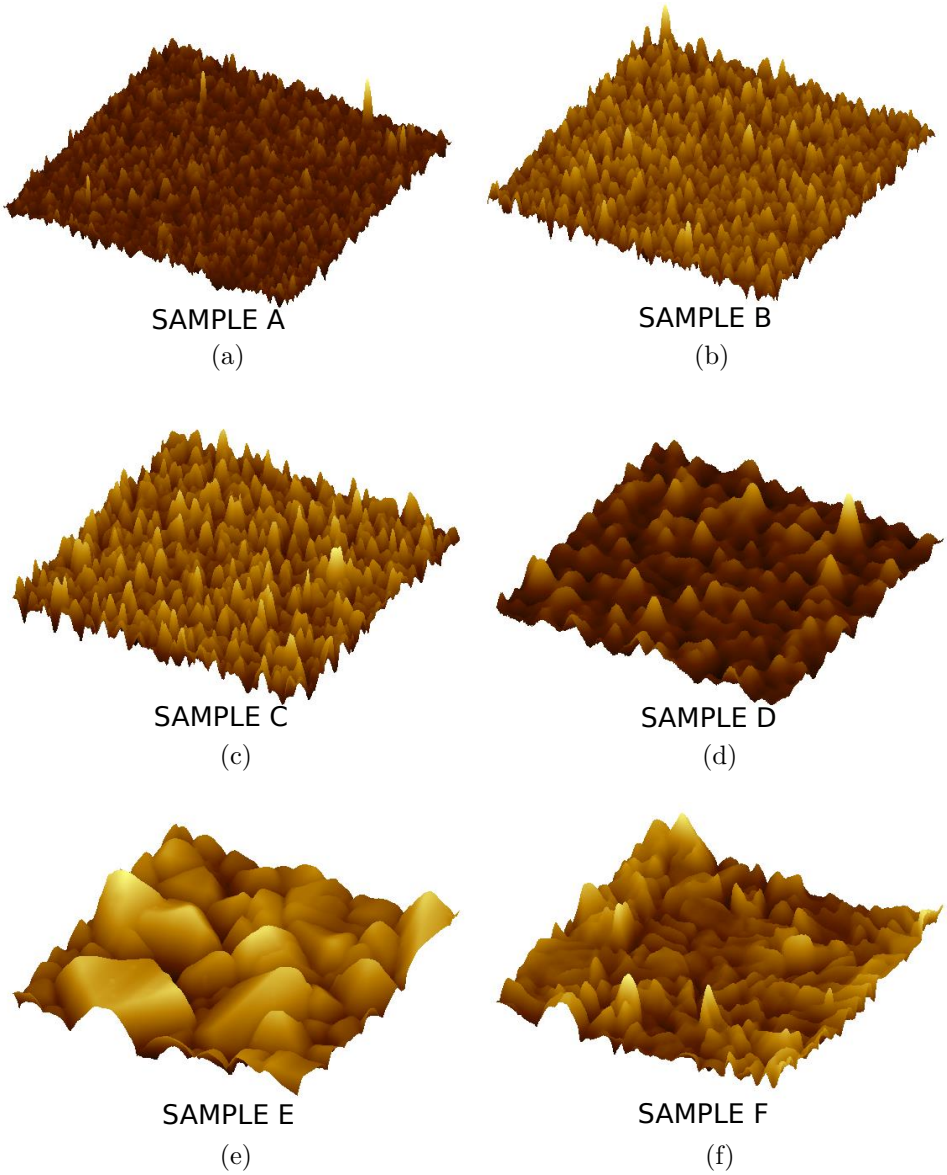

Figure 3.15: The AFM images of all sample surfaces. The dark shade of gold represents troughs and bright shade of gold represents crests.

Chapter 4

Results and analysis

In this chapter, details of the DC resistive measurements are provided. The properties hence retrieved on all the Al films fabricated are presented. The RF measurement setup and the results obtained from measurements of the resonators are explained and the quality factor of the resonators are extracted. Finally, the interpretations of the results are explained in detail in terms of the models discussed in the theory chapter.

4.1 Properties of film by DC measurements

A pattern for the four probe measurement is fabricated on each chip along with the resonators. This helps with characterizing the film properties of the resonators. The chip is diced to separate the resonator sample from the four probe measurement sample. The false colored SEM image of four probe system is shown in Figure 4.1. Two measurements are done on the sample: 1. Resistance measurement and 2. Critical field measurement.

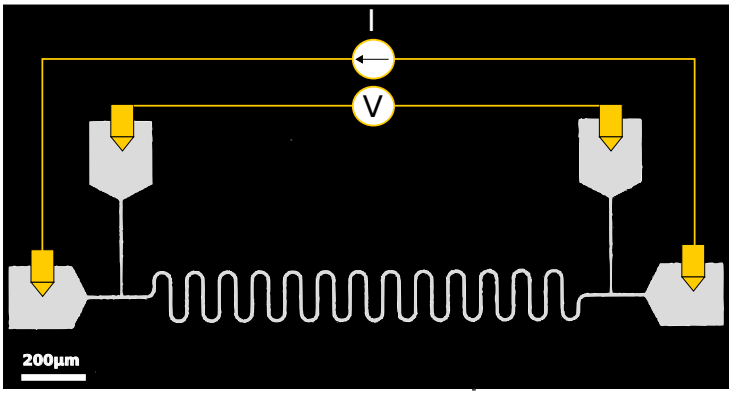

Figure 4.1: Representation of 4 Probe DC measurement shown with the false colored SEM image of a sample.

4.1.1 Resistance measurement

The resistance is measured by applying current through outer pads of the pattern and the voltage drop is measured across the inner pads as shown in the figure. The resistance is measured for temperatures from $340K$ to $600mK$. Temperature sweep measurement provides film properties such as residual resistance ratio (RRR), critical temperature

(T_C) and residual electron mean free path (l).
RRR is defined as the ratio of resistance at 300K and 4K and it informs about the electronic transport properties of the film. When the RRR is high, the density of defects and impurities in the sample is low. The temperature at which a metal transition from its normal state to its superconducting state, also known as the critical temperature can be extracted. The most important information obtained is the residual electron mean free path which is necessary to understand the relationship between losses in the resonators and their electron mean free path.
The length of the wires of four probe measurements is arbitrarily chosen to be 4820μm. This length is sufficiently long to measure a quantifiable resistance. The width of the patterns are chosen to be the same as that of the resonators. Having same cross sectional dimension helps in assigning the properties such as T_C and l from the measurements of the pattern of the films to the resonators, since these properties depend on the cross sectional dimensions of the samples.
The measurements are done with physical property measurement system (PPMS) by Quantum design with ^3He cryo fridge to reach a minimum temperature of $415mK$, much below the transition temperature of bulk Al of 1.2K.
The minimum resistance measurable by the PPMS is (3.81nV/5mA=0.762$\mu\Omega$) which is governed by the resolution of Analog to Digital converter (ADC) of the measurement system. But for a superconducting wire, current of 5mA cannot be applied due to two reasons. Firstly, there is the critical current limitation on the superconductor and secondly, critical temperature reduces as current through the wire increases. Hence it is ideal to send as low current as possible to avoid perturbing the critical temperature measurements. The minimum current that can be applied through the current source of PPMS is 10nA. However, the disadvantage of applying small current arises from the noise error due to measurement of very low voltages drop across the wire. Therefore, care is taken to have reliable measurement of critical temperature as well as enough resolution to obtain the residual resistance. Therefore for samples A, B C and D below 4K, 20nA of current is applied and, for samples E and F it is 50nA. These values were adjusted by observing the data in order to have enough signal to noise ratio (SNR).
The resistance of the wire of length L, width W and thickness t is given as

$$R = \frac{\rho L}{Wt} \tag{4.1}$$

where ρ is the resistivity of the film. The resistivity is extracted from the above equation since the dimensions of the patterns are known from the AFM measurements. The resistivity and mean free path of a film are inversely proportional. The relationship between

resistivity (ρ) and mean free path (l) for Al [64] is

$$\rho l = 0.501 \times 10^{-11} \Omega.cm^2 \tag{4.2}$$

The resistivity is given for all six samples in Figure 4.2 calculated using Equation 4.1.

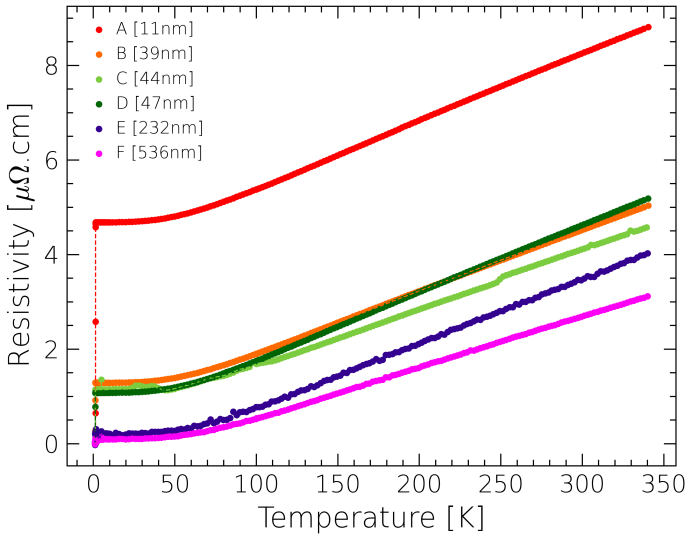

Figure 4.2: Resistivity as a function of temperature where legends show the sample names and deduced mean free paths.

The mean free paths is later deduced from Equation 4.2.
As temperature decreases, the resistivity decreases since the scattering of electrons due to thermal phonons decreases. Below certain temperature, for metals like Al, the resistivity remains constant. At low temperatures, there are no more thermal phonons contributing to the scattering of electrons. Scattering at lower temperatures is hence governed only by impurities and defects.
From analyzing the resistivity measurements, several conclusions can be drawn. Firstly, sample A which is a thin film of 59nm thickness, deposited in chamber pressure of 5×10^{-7}mbar has the smallest mean free path and smallest RRR among the samples measured. The samples B,C and D are deposited with an overnight pumping in a chamber pressure of 3.5×10^{-8}mbar.
Sample E and F which are thick films have larger mean free paths and larger RRR than thin films. This might be explained by their reduced surface scattering. Sample E with thickness of 2.7μm has smaller RRR and mean free path than sample F of 588nm thickness because of sputtering at high pressure 2.3×10^{-7}mbar without overnight pumping.
According to the results, the mean free path in films fabricated under high chamber pressure is small and the sample thickness affects the mean free path. The Table 4.1 shows the mean free path, RRR and T_C of the samples.

4.1.2 Critical field calculations

Critical magnetic field is the magnetic field above which a superconductor becomes a normal state metal. Various critical field equations depending on the type of superconductor are discussed here.

In the theory chapter, the effective coherence length and effective penetration depth were defined for 0K. The temperature dependence of these parameters are given below:

$$\begin{aligned} \lambda(T) &= \lambda(0)(1-(T/T_C)^4)^{-1/2} \\ \xi(T) &= \xi(0)\left(\frac{1+(T/T_C)^2}{1-(T/T_C)^2}\right)^{1/2} \end{aligned} \tag{4.3}$$

where formulae for $\lambda(0)$ and $\xi(0)$ which are functions of mean free path are given in Equation 2.14. The critical field for a bulk Type-1 superconductor by substituting Equation 4.3 is:

$$H_C(T) = \frac{\Phi_0}{2\pi\sqrt{2}\lambda(T)\xi(T)} = \frac{\Phi_0}{2\pi\sqrt{2}\lambda(0)\xi(0)}\left(1-\left(\frac{T}{T_C}\right)^2\right) \tag{4.4}$$

But, for finite thickness due to the non-zero demagnetizing factor, Type-1 superconductors enter into an intermediate state. In intermediate state, the critical field can be lower than the value of the bulk Type-1 superconductor. The intermediate state critical field is given as:

$$H_{CI}(T) = H_C(T)\left[\left(1+\frac{4\delta}{t}\right)^{1/2} - \left(\frac{4\delta}{t}\right)^{1/2}\right] \tag{4.5}$$

where t is the thickness of the film and $\delta = \xi(T) - \lambda(T)$. Finally, for Type-2 superconductor, the critical field is given as

$$H_{C2}(T) = \sqrt{2}\kappa H_C(T) = \frac{\Phi_0}{2\pi\xi^2(T)} = \frac{\Phi_0}{2\pi\xi^2(0)}\frac{1-\left(\frac{T}{T_C}\right)^2}{1+\left(\frac{T}{T_C}\right)^2} \tag{4.6}$$

4.1.3 Critical field measurement

Critical field is extracted by measuring resistance of the sample while sweeping the magnetic field perpendicular to the sample. The field at which the resistance of the sample is half of its maximum value is considered as the critical field. These measurements are repeated for different temperatures below T_C.

The step size of the magnetic sweep is 0.1 or 0.2mT. The resistance as a function of field sweep for sample E at 1K is reported in Figure 4.3. The blue arrow shows the superconducting to normal state transition and red arrow shows the normal state to superconducting state transition.

The sample passes from superconducting to normal state at 1.7mT which is the consid-

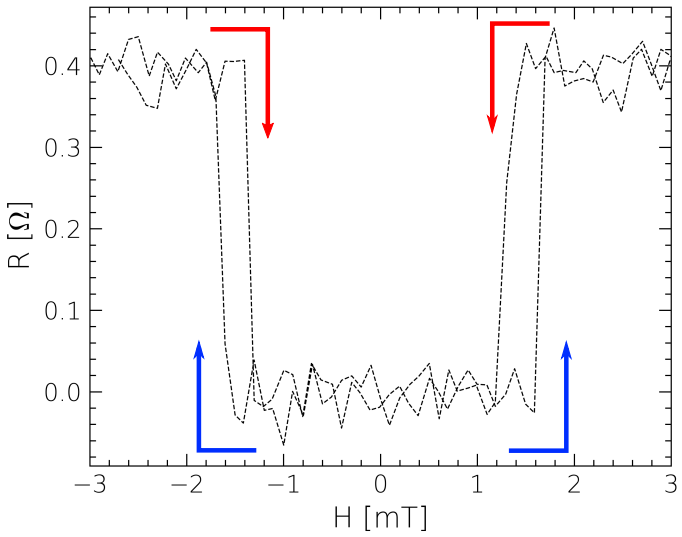

Figure 4.3: Resistance as a function of magnetic field sweep for sample E at 1K.

ered critical field of the sample at 1K. However, when the field is reduced, the samples does not transition to the superconducting state at the critical field. The transition occurs for a smaller field, in this case 1.3mT. This hysteresis occurs in Type-1 superconducting samples due to a phenomenon known as the supercooling effect. Supercooling effect is a phenomenon where Type-1 superconductors stays in normal state below their accepted critical field value. This occurs due to the energy barriers for the superconducting state nucleation in the metal. In a Type-2 superconductor there is no hysteresis.

The critical field extracted for each sample (except sample A) as a function of temperature normalized by T_C is shown in Figure 4.4 by dots. The dashed lines represent the fitting using Equation 4.5 and 4.6 with intrinsic coherence length and London penetration depth as fitting parameters. The critical magnetic field is maximum when the temperature is 0K and decreases with temperature. At $T = T_C$, the critical magnetic field becomes 0T and the superconductor becomes a normal state metal.

For Sample A, the magnetic field was not measured, since this was the first measurement and I was not aware of the ways to do magnetic field sweep. For the samples B and C, the best fit is obtained by the critical field of Type-2 superconductor given in Equation 4.6 with intrinsic coherence length as a fitting parameter.

The magnetic field sweep for samples E and F demonstrates hysteresis, and the critical field is less than the bulk value (bulk value of critical field of Al is 10mT [65]). Type-1 intermediate state critical field given in Equation 4.5 provides a good fit for the measured data. For sample D, the magnetic field sweep does not show hysteresis but the critical field is slightly smaller than the bulk value and the best fit is given by considering the Type-1 intermediate state critical field. For samples D, E and F, intrinsic coherence length and

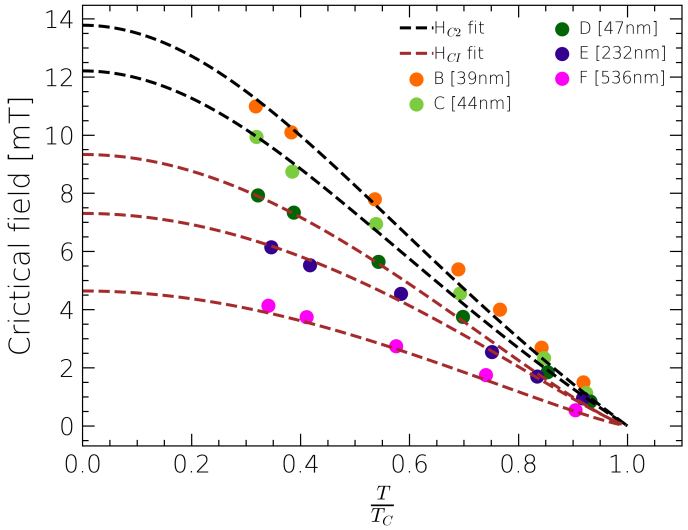

Figure 4.4: Critical field as a function of temperature of all the samples except sample A where legends show the sample names and mean free paths.

London penetration depth are the fitting parameters.

4.1.4 DC measurement summary

In Table 4.1 all the properties of Al films that are extracted are summarized. From the table, it can be observed that, the critical temperature of Al approaches the bulk value of 1.2K [66] as the mean free path increases.

The London penetration depth retrieved from the fit is similar to the predicted value of

Sample name	l [nm]	RRR	T_C [K]	ξ_0 (fit) [nm]	λ_L (fit) [nm]
A	10.9	1.76	1.43	-	-
B	39.6	3.5	1.3	648	-
C	44.6	3.58	1.29	642	-
D	47.4	4.29	1.28	608	14
E	232.6	15.58	1.19	630	22
F	536.8	28.8	1.2	592	15
Average				624	~ 17

Table 4.1: Table summarizing the properties of the samples

16nm [66]. The intrinsic coherence length however, is much smaller than calculated value of 1200nm. The BCS theory was derived for materials with spherical Fermi surface and coherence length was calculated assuming the Fermi surface is spherical. But in reality materials have anisotropic Fermi surfaces. Hence, the change in intrinsic coherence length has been attributed to the anisotropic Fermi surface of Al in the literature where the coherence length in the range of 500nm is observed [67]. The variations in the intrinsic

coherence length between samples given in the table could be explained by the stoichiometric change because of the difference in quality of Al and vacuum in chamber when depositing each film.

4.2 RF measurements

The RF measurements in this work involves, spectroscopic measurements of resonators in reflection. The setup used for the measurement and the results obtain on resonator samples are discussed in this section.

4.2.1 Measurement setup

The measurements of resonators are done at temperature in the range of $20 - 500mK$. In order to reach a base temperature of $20mK$ Bluefors dilution dry fridge is used. The detailed schematic representation of the setup is given in the Figure 4.5.
The microwave signal is transmitted from and received back to the ZNB-20 Vector Network Analyzer. A series of attenuators are placed in the input line at different stages of the refrigerator. These attenuators reduce the amount of thermal photons entering the waveguide from room temperature and exciting the resonators. The total attenuation inside the fridge from $50K$ to $20mK$ is $62dB$.
In addition, the signal is filtered by $40GHz$ and $12GHz$ low pass filter (LPF) before entering the waveguide. The reflected signal from the waveguide passes through a circulator and is amplified with a commercial HEMT low noise amplifier from Low noise factory at 4K and other room temperature amplifiers. An isolator is used to avoid any high amplitude signal from reflecting back to the waveguide from the higher stages of refrigerator of the output port. To avoid any radiation and magnetic field fluctations from affecting the sample, the waveguide is enclosed in a Cryoperm and IR shield.

4.2.2 Measurement details

The measurements are done by sweeping the frequency of the microwave signal across resonances of the resonators at different applied power. The measurements are done with a bandwidth of 1Hz which increases the SNR. At low powers, to reduce the noise further, the sweeps are averaged 20-50 times depending on the power of the signal. The reflection coefficient of resonator from sample B is reported in Figure 4.6 for an average photon number in the resonator of about 1.
The reflection coefficient data corresponds to the resonator design with Capacitance gap of $30\mu m$. The magnitude of S_{11} in dBm as a function of frequency is given in Figure 4.6a in blue lines and its phase in radians is given in Figure 4.6b. The measured coefficient in complex plane is plotted in Figure 4.6c as blue dots which is circle fit. The fits are shown

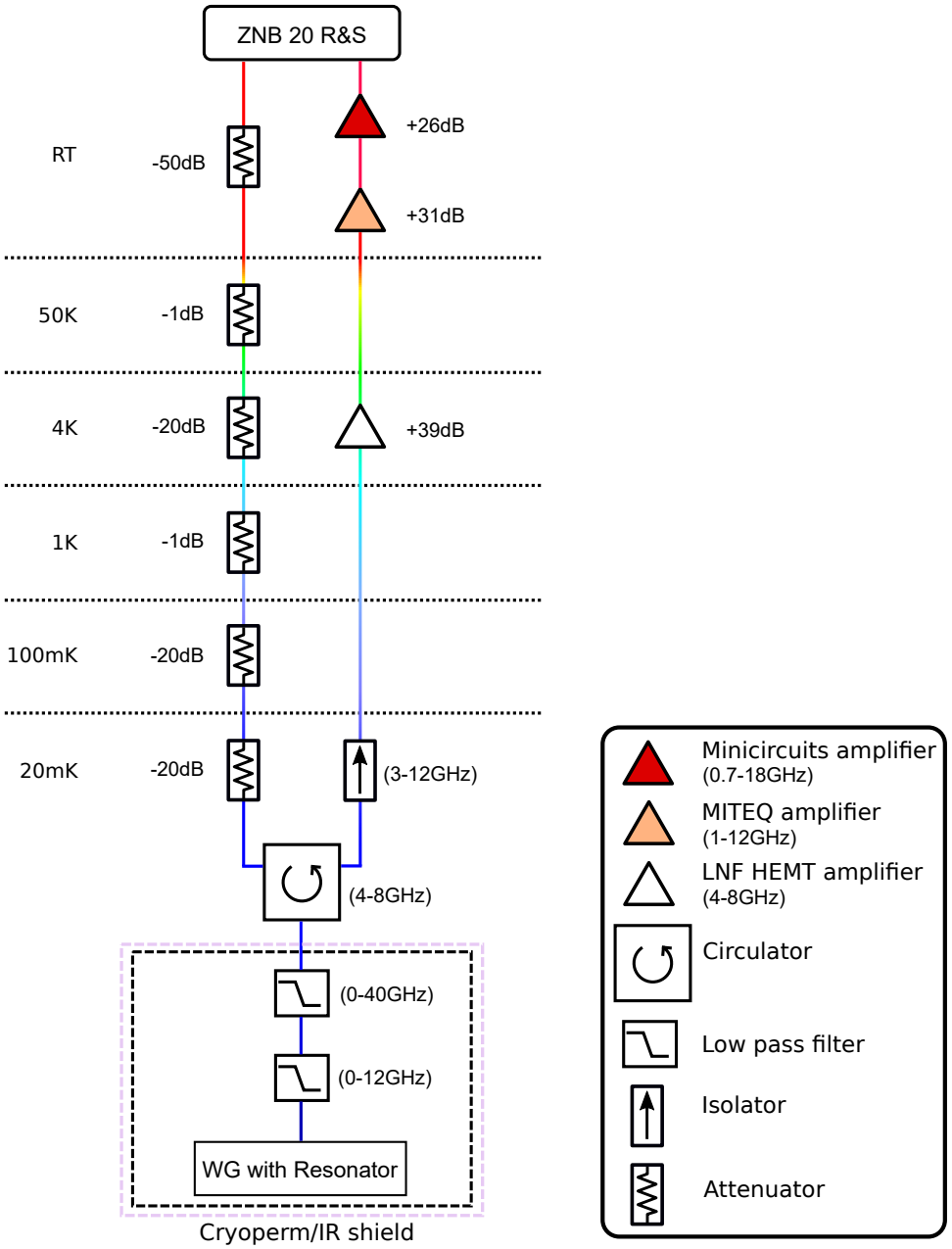

Figure 4.5: Resonator measurement setup

by the black solid lines.

The measurement is explained as follows: Out of resonance, signal amplitude and phase reflected from waveguide remains constant. At resonance, the resonator is excited. The signal reflected from the port of the waveguide decreases since some of the signal is absorbed by the resonator. The absorption is maximum at the resonance and a dip in the amplitude of reflected signal is observed. This is quantitatively discussed in the Equation 2.10. The phase of the resonator undergoes a phase rotation by less than π radians at resonator frequency.

By fitting these measurements with the circle fit, the resonant frequency(f_r), the internal quality factor(Q_i) and the coupling quality factor(Q_C) are obtained. In addition, since

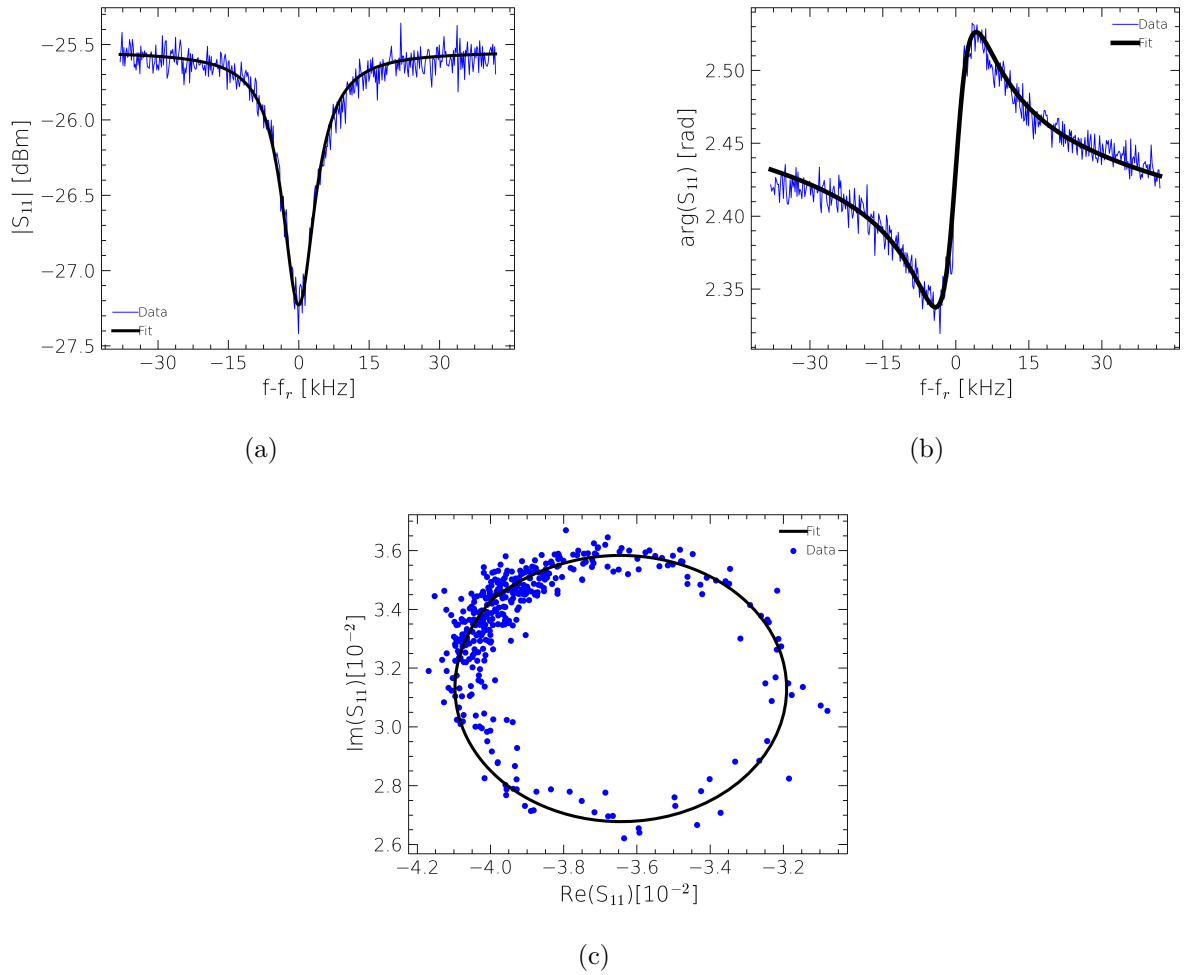

(a) (b)

(c)

Figure 4.6: Resonator measurements given in blue and fit shown in solid black line. (a) $|S_{11}|$ as a function of frequency, (b) $\angle S_{11}$ as a function of frequency and (c) real vs imaginary part of S_{11}.

the applied power is known, the photon number n can be estimated using:

$$n = \frac{4P_{in}Q_L^2}{\hbar\omega_r^2 Q_C} \tag{4.7}$$

where P_{in} in the applied power to the resonator, Q_L and Q_C are the loaded and coupling quality factors respectively.

4.2.3 Photon number dependence

The above measurements are repeated with different photon numbers by changing applied power. From the extraction of internal quality factor and photon number, Figure 4.7a is plotted. The data is fit with TLS model given in Equation 2.37, the different parameters such as n_c, Q_{0TLS}, β and Q_{other} can be extracted. All the parameters from the fit can be seen in Appendix B.

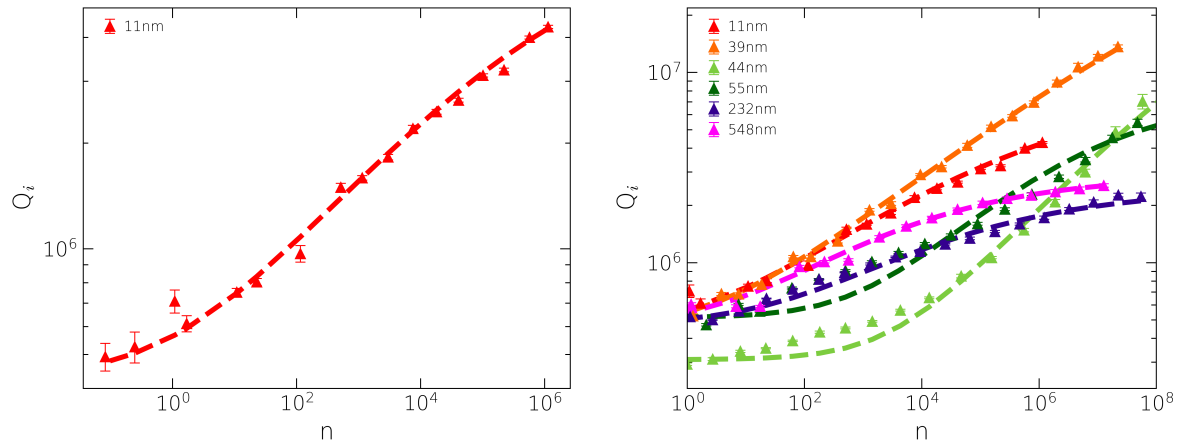

(a) (b)

Figure 4.7: Internal quality factor as a function of photon number (a) for resonator with 30μm capacitance gap of Sample A and (b) for resonators of different mean free path with 30μm capacitance gap.

As it can be seen, for low photon numbers the quality factor is low. TLS loss is the dominating factor in the low photon limit since some of the signal is absorbed by the defects and adatoms which gets excited and relaxed between two configurations as discussed in theory chapter. When all the TLSs are saturated, the quality factor starts to increase. The increase stops once another quality factor limiting losses starts to dominate. This could be due to other mechanisms that are discussed in the theory chapter.
The measurements and extractions are repeated for different resonators. In Figure 4.7b, the quality factor given by triangular dots of different color for different mean free path is fit with the TLS model. The data shown corresponds to resonators with Capacitance gap of 30μm. These measurements are performed at temperature of $\sim 25mK$. The losses extracted from the fit and its inference will be discussed in detail in the next section 4.3.

4.2.4 Temperature dependence

For a given power, the reflection coefficient measurements are performed at different temperatures, from $25mK$ to $480mK$. These measurements are performed in order to study the frequency shift and the change in quality factor of the resonators as a function of temperature.
The reflection coefficient measurement as a function of frequency is reported for different temperatures in Figure 4.8. Between $27mK$ and $175mK$ there is no visible shift in the frequency of the resonator. Further increase of temperature, indeed shows a red-shift of the frequency. This can be explained by the decrease of the superconducting electron density, and hence increase in the kinetic inductance. As kinetic inductance increases, the total inductance increases resulting in the decrease of resonant frequency.

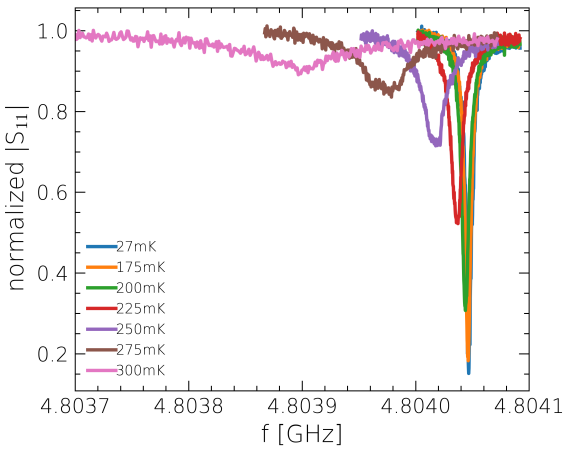

Figure 4.8: S_{11} as a function of frequency for resonator with $60\mu m$ Capacitance gap of sample B for different temperatures.

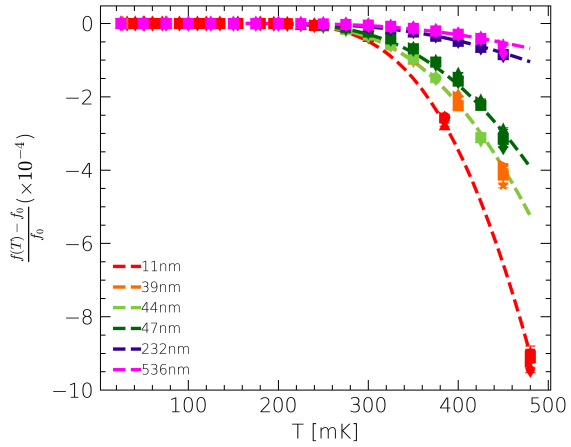

Figure 4.9: Change of frequency as a function of temperature for resonators of different mean free path.

Sample	l [nm]	α (%)
A	11	12.02±0.17
B	39	4.73±0.15
C	44	4.53±0.27
D	47	3.18±0.11
E	232	0.65±0.01
F	536	0.43±0.05

Table 4.2: Values of ratio α for different samples

The change in frequency as function of temperature is plotted in the Figure 4.9 for the different samples. Sample data are indicated by their mean free paths. The dashed lines represent the fitting of the frequency shift using the formula [68]:

$$\frac{f(T)-f_0}{f_0} = -\frac{\alpha}{2}\sqrt{\frac{\pi\Delta(0)}{2k_BT}}e^{-\Delta(0)/k_BT} \tag{4.8}$$

where f_0 is the resonant frequency at base temperature of $25mK$, α is the ratio of kinetic inductance to the total inductance. The only free parameter here is the ratio α because $\Delta(0)$, whose relationship to T_C is given in Equation 2.11, is obtained from DC measurements.

In the Table 4.2, the meanfree path of the samples and the corresponding α is given. The

relationship between mean free path and kinetic inductance can be calculated for thin and thick film as:

$$\begin{aligned} L_k =& \frac{\mu_0 \lambda^2 l_r}{Wt} = \frac{\mu_0 \lambda_L^2 (1 + \xi_0/l) l_r}{Wt} \text{ when } \lambda >> t \\ =& \frac{\mu_0 \lambda l_r}{2W} = \frac{\mu_0 \lambda_L \sqrt{1 + \xi_0/l} l_r}{2W} \text{ when } \lambda << t \end{aligned} \tag{4.9}$$

where λ is the effective penetration depth, t is the thickness of the resonator and l_r is the length of the resonator.

Since all the parameters are known, the kinetic inductance can be extracted. The largest kinetic inductance is calculated to be $0.99 pH/\square$ for sample A. The value is cross verified with the results from simulation.

As samples mean free path increases the kinetic inductance ratio decreases. In sample B, C and D the difference of mean free path is small but sample D has smaller α than sample B and C. This is because of an increase in thickness in sample D in comparison with sample B and C.

For thin films where $\lambda >> t$, the kinetic inductance varies due to mean free path and the thickness. For thick films where $\lambda << t$, the kinetic inductance is only dependent on the sample mean free path. Therefore, sample F has smaller α than sample E even though the thickness of sample F is five times smaller than sample E.

Therefore, in order to achieve high kinetic inductance in thin films one could reduce the mean free path and thickness of the sample. These results could help the different applications involving high kinetic inductance in better design of their systems.

4.3 Losses in resonators

All the different losses in resonators witnessed in this work will be discussed in detail in this section. Loss related to thermal quasiparticle is discussed first. Then the ground plane loss, followed by high photon and TLS losses are discussed.

4.3.1 Equilibrium thermal quasiparticle loss

The internal quality factor as a function of temperature is shown for resonators of sample B in Figure 4.10a. The internal quality factor for temperatures below $200 mK$ is mostly constant. The quality factor for these temperatures is limited by two level system loss. For temperature above $200 mK$, quality factor starts to decrease and becomes independent of the applied power. It can be attributed to the increase of thermal quasiparticle density with temperature which increases the losses.

In Figure 4.10b, a scatter plot of internal quality factor at $300 mK$ as a function of mean free path is reported. The dots represent the mean value of quality factor of the six

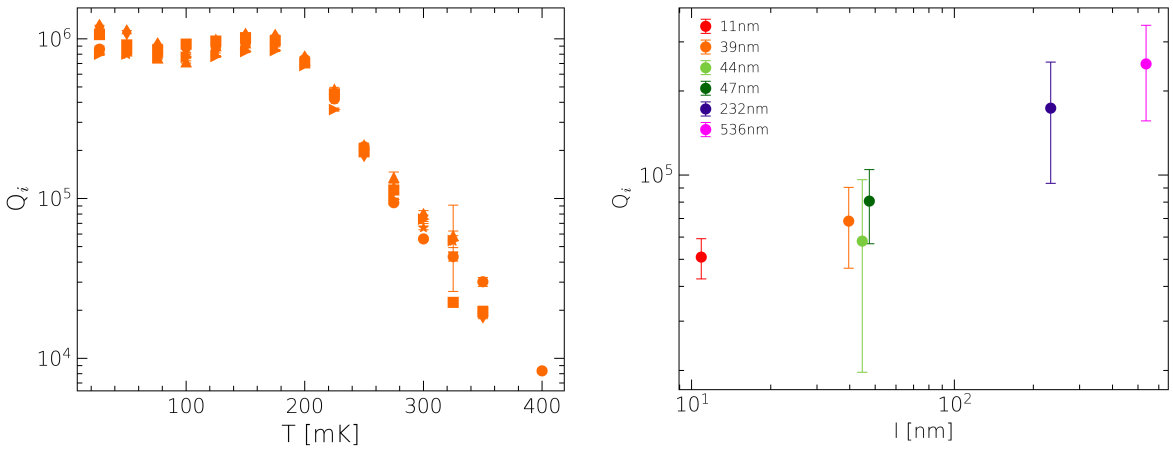

(a) (b)

Figure 4.10: (a) Internal quality factor as a function of temperature for resonators of sample B. (b) Internal quality factor as a function of mean free path at 300mK temperature.

resonators with different Capacitance gap and the error bar represents their standard deviation. It can be seen that the quality factor increases with mean free path.

The internal quality factor is given by $1/Q_i = 1/Q_{TLS} + 1/Q_{qp}$ where $1/Q_{TLS}$ is the TLS dependent quality factor and $1/Q_{qp}$ is the quasiparticle dependent quality factor. The quality factor is plotted for data from $300mK$ temperature measurements. This is because, above $250 - 275mK$, the quality factor is dominated by quasiparticle losses, $Q_i \simeq Q_{qp}$, since at these temperatures $Q_{TLS} >> Q_{qp}$.

From the measured intrinsic quality factor we can extract the resistance of the resonators due to quasiparticles using Equation 2.34 where

$$R_{qp} = \frac{\omega L}{Q_i} = \frac{\omega L_k}{\alpha Q_i}$$
$$R_S = R_{qp} W / l_r \tag{4.10}$$

where L is the total inductance, R_{qp} is the resistance due to quasiparticles, R_S is the surface resistance, l_r is the length of the resonator with W as the width. α, ω and Q_i are known from the experiments and L_k is calculated using Equation 4.9.

The surface resistance of different resonators is scatter plotted as a function of mean free path in Figure 4.11a. The surface resistance of the samples reduces with increasing mean free path.

This behaviour is compared with theoretical calculations of surface resistance for bulk film using Equation 2.30 with the black dashed lines when $T_C = 1.2K$ and black bold lines when T_C is dependent on mean free path. Similarly, blue dashed and bold lines are calculated considering finite film thickness of 50nm, calculated using Equation 2.33. Since the thickness is finite, the surface resistance is larger than bulk samples.

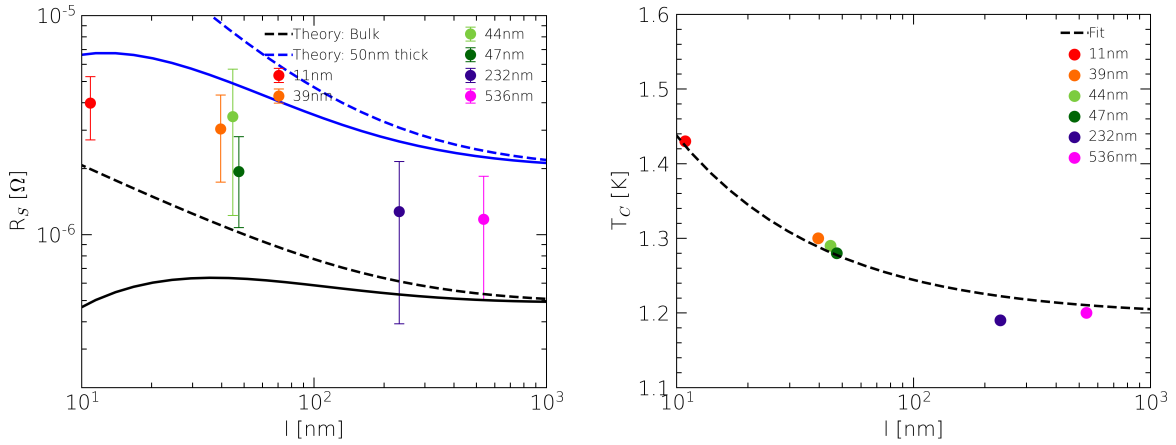

(a) (b)

Figure 4.11: (a) Surface resistance as a function of mean free path with data from resonators of different mean free path shown in dots and bold and dashed lines are the theoretical calculations and (b) Critical temperature as a function of mean free path with an empirical fit.

In order to obtain mean free path dependent T_C, the critical temperature of samples as a function of mean free path is plotted in Figure 4.11b and the data is empirically fit. This is shown by dashed lines in the figure. The fitting formula used here is:

$$T_C = 1.2\left(1 + \frac{1}{l^{\gamma}}\right) \tag{4.11}$$

where l is the mean free path and γ is found to be 0.693 from the fit.
The data of surface resistance lies within the agreeable limits of the theoretically calculated levels. Therefore, it can be concluded that for higher temperatures the loss reduces with increasing mean free path in 2D resonators.

4.3.2 Ground plane loss

One of the parameters obtained from fitting internal quality factor as a function of n, is the high photon limit saturating quality factor given in equation 2.37 as Q_{other} which is discussed in section 4.2.1. There are many limiting factors as discussed in the theory chapter. The loss under consideration is the ground plane loss of the metal in the high photon limit.
Sample A is measured both in Copper waveguide and Aluminium waveguide. Cu walls acts as metallic ground plane while Al walls acts a superconducting ground plane. It can be fairly assumed that the loss due to superconducting ground plane (few tens of $n\Omega$s) is much smaller than the metallic ground plane. Hence, the surface resistance of the Cu

used in the waveguide at the temperature of $25mK$ can be calculated using:

$$R_{SCu} - R_{SAl} = \frac{\omega L_k}{\alpha}\left(\frac{1}{Q_{otherCu}} - \frac{1}{Q_{otherAl}}\right) \simeq R_{SCu} \quad \text{since } R_{SAl} << R_{SCu} \tag{4.12}$$

where R_{SCu} and R_{SAl} is the surface resistance of the Cu and Al waveguide wall with internal quality factor $Q_{otherCu}$ and $Q_{otherAl}$. By taking the difference as shown above, all other losses due to quasiparticles or AC losses can be eliminated.
The resonators of sample A are measured in Cu and Al waveguides in consecutive cool downs of the fridge.The saturating quality factor of all resonators of sample A in Cu and Al waveguide as a function of their resonant frequencies is shown in Figure 4.12. The quality factor of resonators in Cu waveguide is smaller than Al waveguide. This is explained by the increased loss coming from metallic waveguide.

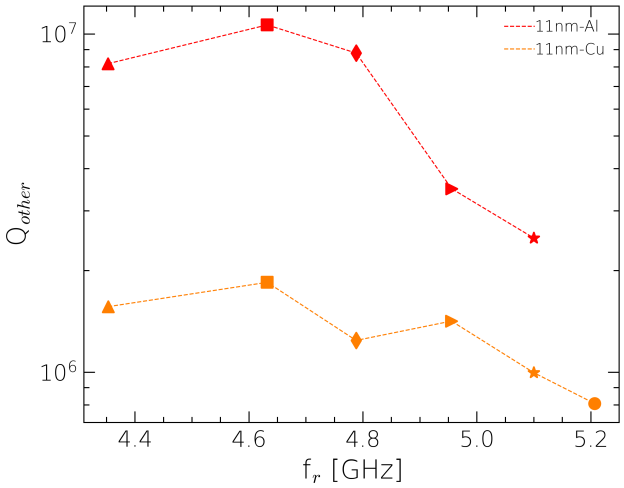

Figure 4.12: Saturating internal quality factor as a function of resonant frequencies with data from sample A in Copper (orange) and Aluminum (red) waveguide.

The surface resistance R_{SCu} is calculated to be $131 \pm 30\mu\Omega$. The conductivity of the Copper metal at $25mK$ calculated using Equation 2.42 is hence $1.2 \pm 0.47 \times 10^{10}[\Omega.cm]^{-1}$. This is comparable to the value obtained in literature [69]. The conclusion of this work is that metallic ground planes limit the quality factor at large photon limit. It can be solved by using superconducting ground planes. However, superconducting ground planes can be dissipative if there is movement of flux or flux creep which would increase the loss [70][71]. But this can be avoided by surface treatments [72] or design modifications of ground planes for flux traps.

4.3.3 AC loss

The saturating quality factor Q_{other} obtained from resonators measured in Al waveguide is discussed in this section. In the high photon limit, the internal quality factor saturates because of non-TLS sources. The origin of these sources is still an open question. The saturating quality factor as a function of mean free path of the resonators is plotted in Figure 4.13a. Different colors represent different mean free paths. Quality factor of samples is shown to decrease with increasing mean free path except for sample A. Saturating quality factor of more than 10 million is extracted for sample B, with mean free path of 39nm.

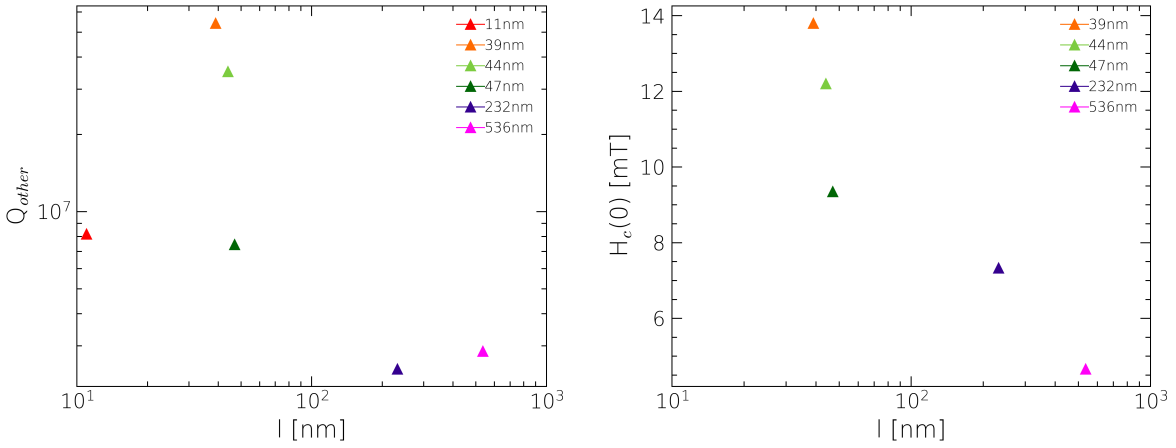

(a) (b)

Figure 4.13: (a) Saturating internal quality factor as a function of mean free path for all resonators with $30\mu m$ capacitance gap and (b) Critical magnetic field as a function of mean free path for all samples except A at 0K.

The extrapolated critical magnetic field at 0K as a function of mean free path is plotted in Figure 4.13b. From comparison between Figure 4.13a and Figure 4.13b, it can be seen that saturating internal quality factor changes similar to the critical magnetic field. Hence it can be argued that the saturating quality factor depends on the critical field of the film. In the literature, the losses at high photon numbers are attributed to RF heating causes by large magnetic field [73][74]. Therefore, the probable limiting factor for loss is the quasiparticles developed by power dissipation in superconductor. And, the dissipation mechanism is governed by the critical field of the resonators.

However sample A does not follow the trend of other samples. It exhibits smaller quality factor even though its expected critical field is large. The losses in sample A can be argued to be due to two reasons. Firstly, nonequilibrium quasiparticles in the high kinetic inductance material [75]. But the kinetic inductance is not large enough compared to the other materials studied in the literature with larger quality factor [39].

The other argument originates from the presence of whiskers on the edge of the sample A

which is about tens times the sample thickness as seen in AFM image in Figure 3.12a. This could interact with the magnetic field and generate vortex motion resulting in generating excess quasiparticles. At this time, second argument seems to be more realistic, however more samples with smaller mean free paths need to be measured to check the validity of these reasons.

4.3.4 Two level system loss

Limitation at low photon number is dominated by the TLSs. The internal quality factor due to TLS i.e. Q_{0TLS} for each sample measured, is plotted in Figure 4.14 as a function of the resonator Capacitance gap. The extracted Q_{0TLS} of each sample is given by colored

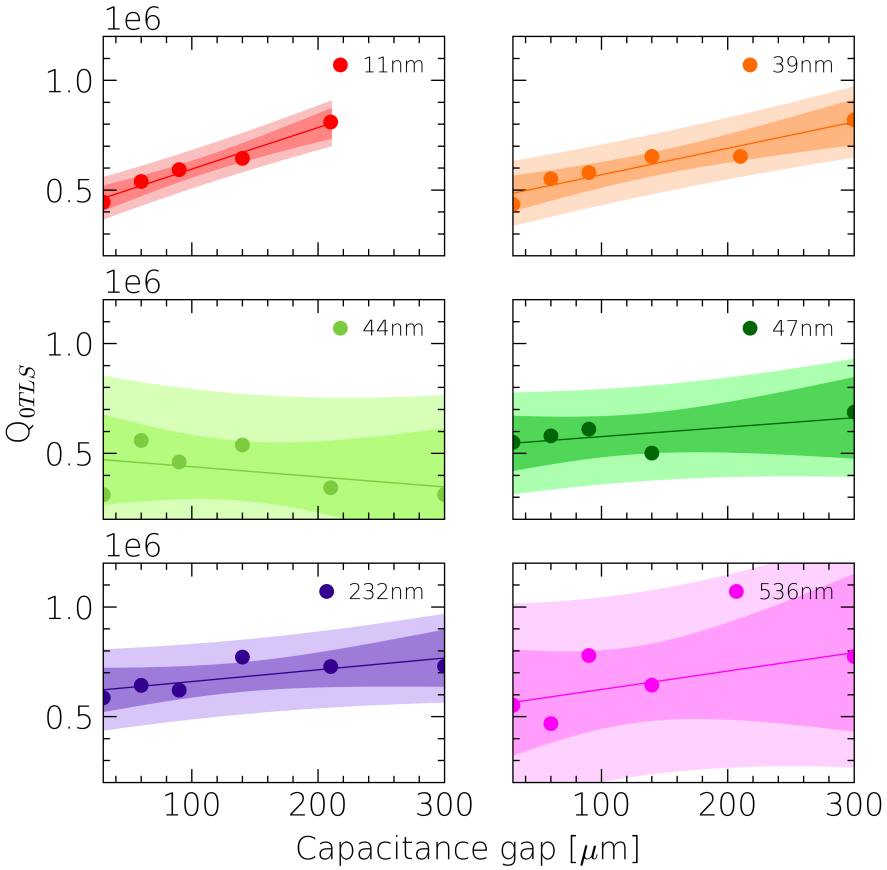

Figure 4.14: Internal quality factor due to TLS losses as a function of resonator capacitance gap with data given in scatter plot with a linear fit and confidence interval.

dots. A linear regression fit is shown as solid line in each plot. It provides the slope of the data. Each plot also shows 95% confidence interval to estimate the predictable range of Q_{0TLS} from the given data. All samples show an increase in the quality factor with Capacitance gap except sample C with 44nm mean free path as shown in the figure. Also the squared correlation coefficient which defines the correlation between the capacitance

gap and quality factor is calculated for each sample. It is given in Table 4.3.
It can be seen that the thin films have very high correlation coefficient which expresses that the change in quality factor in thin films are directly related to the Capacitance gap. For the thick films, the coefficient reduces. This reduction of correlation for thick films can be explained by the larger distribution of the extracted Q_{0TLS} as a function of the Capacitance gap. However, the sample of 44nm mean free path has the least correlation coefficient suggesting that other losses independent of capacitance gap are affecting the resonators.
The conclusions obtained from these measurements are:

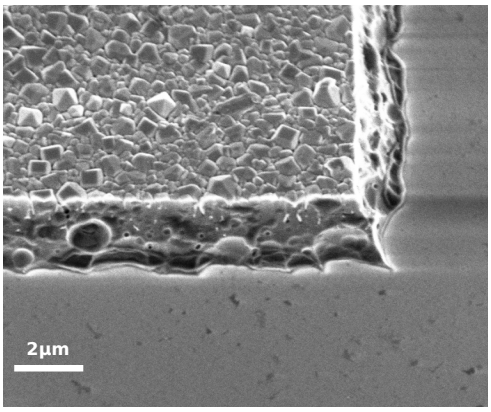

Figure 4.15: SEM image of the surface of the sample E with mousebites because of etching.

Sample	l [nm]	r^2
A	11	0.98
B	39	0.91
C	44	0.17
D	47	0.43
E	232	0.55
F	536	0.43

Table 4.3: Table showing the squared correlation coefficient of different samples.

Firstly, the quality factor increases with capacitance gap due to reduced electric field concentration at interfaces of substrate and air [76][77]. This reduces any TLS loss originating from the substrate surface. Secondly, thick films in general show reduced slope than the two thin films. This could be due to the increase of superconducting surface area. More TLS on the superconducting surface interact with the electric field hence additional losses are seen in thick films.
Thirdly, the quality factor of the 44nm mean free path sample decreases with the increasing capacitance gap. Since the film is etched, the sample has residue of biproducts of etchants on the surface or unevenly etching of Al as shown in the red dashed boxes of AFM image in Figure 3.14b which increases the loss. Additionally, the uneven surfaces and "mousebites" as shown in SEM image of thick film surface in Figure 4.15 due to wet etching could increase the oxide defects on the surface increasing TLS loss. Sample E with mean free path of 232nm, which is also a film that is etched, shows stronger correlation compared to Sample C. This might be explained by considering the electric field in thick films are less sensitive to residues on the substrate surface since the electric field is not highly concentrated close to the substrate as in thin films.

4.4 Summary

From the resonators measurements done with temperature ranging from 25mK to 500mK, it can be concluded that the quality factor increases as temperature decreases due to reduction in thermal quasiparticles and below the temperature of 200mK, the quality factor saturates due to the limiting factor of TLS interface losses. The losses due to thermal quasiparticles are shown to reduce with increasing mean free path. The surface resistance decreases from $4 \times 10^{-6}\Omega$ to $10^{-6}\Omega$ as sample mean free path increases from 11nm to 588nm, a four time reduction in resistance. The kinetic inductance ratio reduces from 12% to 0.5% as mean free path increases and this is again due to the reduction of quasiparticle density or increased superconducting electron density.
The resonators are also measured at 25mK with average photon number ranging from 0.1 photons to $10^7 - 10^8$ photons. The quality factor increases with photon number from $5 - 6 \times 10^5$ to $1 - 2 \times 10^7$. At the low photon limit, the dominant loss comes from the TLSs on the interface between substrate and air. This is proven by considering different capacitance gaps in the resonators where reduced capacitance is shown to improve the quality factor at low photon limit.
Saturating quality factor at high photon number limit changes with respect to mean free path similarly to the critical field of the electrode. It implies the dependence of magnetic field induced loss which could be explained by the RF heating effect.
To numerically quantify the ground plane loss in metallic ground plane, the saturating quality factor of a set of resonators in two different waveguides are considered. The loss in the Cooper waveguide resonators is larger than the Aluminum waveguide. This is due to the difference in their conductivity. The calculated conductivity of Cooper from the resistance measurements is $1.2 \pm 0.47 \times 10^{10}[\Omega.cm]^{-1}$ which is measured by others to be the conductivity at low temperatures.

Part II

Fluxonium qubit

Chapter 5

Qubit theory

This part of the thesis starts with the theory on the Fluxonium qubit. The chapter is divided into two parts. First part deals with the description of the Fluxonium qubit using lumped elements and explains the energy spectrum of the Fluxonium qubit. The second part is dedicated to considerations for modeling the high kinetic inductance used in the qubit and realized by a chain of Josephson junctions.

5.1 Qubit lumped element description

As mentioned in the introduction chapter, Fluxonium is a variant of the superconducting qubits whose quantum states are characterized by tunneling of quantum of flux into and out of a superconducting loop through the Josephson junction. The simplified circuit schematics of Fluxonium is given in Figure 5.1.

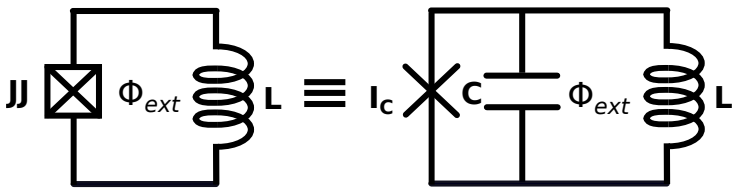

Figure 5.1: Simple Fluxonium circuit with junction (represented by a cross within a box or a cross parallel to a capacitor) parallel to an inductor.

A Fluxonium qubit is obtained by replacing a capacitor with a Josephson junction (JJ) in the LC circuit schematic, which was discussed in section 2.1.1. This novel circuit has a tunable parameter which is the flux Φ_{ext} inside the superconducting loop which is constituted by the inductance and the Josephson junction. The total Hamiltonian therefore includes the Josephson energy in addition to the harmonic oscillator Hamiltonian. Using the circuit theory previously developed [78] the total Hamiltonian is given as:

$$\begin{aligned} H &= 4E_C\hat{n}^2 + \frac{E_L}{2}\hat{\varphi}^2 - E_J\cos(\hat{\varphi} - \varphi_{ext}) \\ \text{with } E_C &= \frac{e^2}{2C}, E_L = \frac{(\Phi_0/2\pi)^2}{L} \text{ and } E_J = (\Phi_0/2\pi)I_C \end{aligned} \tag{5.1}$$

where C is the capacitance of the JJ with energy E_C, L is the inductance with energy E_L, I_C is the critical current of the JJ giving raise to the Josephson energy E_J and Φ_0

is the quantum of flux. The reduced external phase is $\varphi_{ext} = 2\pi\Phi_{ext}/\Phi_0$ where Φ_{ext} is the applied magnetic flux. For the sake of usual convention in superconducting qubits, the capacitive energy has a factor 4 coming from a pair of electrons (i.e. Cooper pairs). It is possible to define reduced charge number operator on the junction capacitance as $\hat{n} = \hat{q}/(2e)$ and the reduced phase operator across the Josephson junction as $\hat{\varphi} = 2e\hat{\phi}/\hbar$ where $\hat{q}$ and $\hat{\phi}$ are the charge and flux operators discussed in the theory chapter of the resonators. They are canonically conjugate variables and they obey the following commutation relation $[\hat{\varphi}, \hat{n}] = \mathrm{i}$.

5.1.1 Eigen matrix and wavefunction calculation

Calculating the eigen values or the energy spectrum of such anharmonic quantum system is analytically difficult. The best way to diagonalize the Hamiltonian matrix is to numerically approximate the eigenvalues. One way to accomplish this is by perturbative method [79]. This method allows the evaluation of the eigenvalues of a relatively complex system by first evaluating the solution for a part of the Hamiltonian which can be easily solved. The solution hence obtained is applied on the analytically unsolvable part of the Hamiltonian and an approximated solution is obtained. The Hamiltonian is hence rewritten as

$$\begin{gathered} H = H_0 - H_1 \text{ where} \\ H_0 = 4E_C\hat{n}^2 + \frac{E_L}{2}\hat{\varphi}^2 \text{ and } H_1 = E_J\cos(\hat{\varphi} - \varphi_{ext}) \end{gathered} \tag{5.2}$$

where H_0 represents the harmonic oscillator whose solution is known and H_1 is the anharmonic part. Using the commutation relation shown above, reduced charge and reduced phase operator can be compared respectively to the momentum and the position operator of a quantum mechanical oscillator. By writing H_0 in the reduced phase basis:

$$H_0 = -4E_C\frac{\hat{\partial}^2}{\partial\varphi^2} + \frac{E_L}{2}\hat{\varphi}^2 \tag{5.3}$$

and comparing it to a quantum mechanical harmonic oscillator

$$H_0 = -\frac{\hbar^2}{2m}\frac{\hat{\partial}^2}{\partial x^2} + \frac{1}{2}m\omega^2x^2 \tag{5.4}$$

where the equivalent mass is $m = \hbar^2/(8E_C)$ and the plasma frequency is $\omega_0 = \sqrt{8E_C E_L}/\hbar$ which are important parameters of the oscillator.
The matrix elements of the Hamiltonian can be calculated using Fock-states of the oscillator as

$$\langle l|H|m\rangle = \langle l|H_0|m\rangle + \langle l|H_1|m\rangle \tag{5.5}$$

The first term on the right side of the above equation associated to the harmonic oscillator can be written as:

$$\langle l|H_0|m\rangle = \langle l|\hbar\omega_0\left(l+\frac{1}{2}\right)|m\rangle = E_l\delta_{l,m} \tag{5.6}$$

The wavefunction of the harmonic oscillator is given by [79]:

$$\langle\varphi|n\rangle = \sqrt{\frac{1}{2^l l!}}\left(\frac{m\omega_0}{\pi\hbar}\right)^{\frac{1}{4}}\exp\left(-\frac{m\omega_0}{\hbar}\frac{\varphi^2}{2}\right)\mathcal{H}_l\left(\sqrt{\frac{m\omega}{\hbar}}\varphi\right) \tag{5.7}$$

where $|n\rangle$ is the charge number basis vector, $|\varphi\rangle$ is the phase basis vector and $\mathcal{H}_l(x)$ is the Hermite polynomial. This solution can be used to find the matrix elements of the second term on the right side of Equation 5.5 since

$$\begin{aligned}\langle l|H_1|m\rangle &= -E_J\langle l|\cos\left(\hat{\varphi}-\varphi_{ext}\right)|m\rangle \\ &= -E_J\cos\left(\varphi_{ext}\right)\langle l|\cos\left(\hat{\varphi}\right)|m\rangle - E_J\sin\left(\varphi_{ext}\right)\langle l|\sin\left(\hat{\varphi}\right)|m\rangle \\ &= -E_J\left[\cos\left(\varphi_{ext}\right)\int_{-\infty}^{\infty}d\varphi\cos\left(\varphi\right)\langle l|\varphi\rangle\langle\varphi|m\rangle + \sin\left(\varphi_{ext}\right)\int_{-\infty}^{\infty}d\varphi\sin\left(\varphi\right)\langle l|\varphi\rangle\langle\varphi|m\rangle\right]\end{aligned} \tag{5.8}$$

By substituting Equation 5.7 in 5.8, one obtains:

$$\begin{aligned}\langle l|H_1|m\rangle = &-E_J\cos\left(\varphi_{ext}\right)2\int_0^{\infty}dx\cos\left(\varphi_0 x\right)\sqrt{\frac{1}{2^l 2^m l!m!}}\sqrt{\frac{1}{\pi}}e^{-x^2}\mathcal{H}_l\left(x\right)\mathcal{H}_m\left(x\right) \\ &- E_J\sin\left(\varphi_{ext}\right)2\int_0^{\infty}dx\sin\left(\varphi_0 x\right)\sqrt{\frac{1}{2^l 2^m l!m!}}\sqrt{\frac{1}{\pi}}e^{-x^2}\mathcal{H}_l\left(x\right)\mathcal{H}_m\left(x\right)\end{aligned} \tag{5.9}$$

where $\varphi_0 = \left(\frac{8E_C}{E_L}\right)^{\frac{1}{4}}$ and $\varphi = \varphi_0 x$. The integration can be solved using formula (In section 7.388 of [80]):

$$\begin{aligned}\int_0^{\infty}dxe^{-x^2}\cos\left(bx\right)\mathcal{H}_l\left(x\right)\mathcal{H}_{l+2p}\left(x\right) &= 2^{l-1/2}\left(-1\right)^p\sqrt{\frac{\pi}{2}}l!b^{2p}e^{-b^2/4}\mathcal{L}_n^{(2p)}\left(b^2/2\right) \\ \int_0^{\infty}dxe^{-x^2}\sin\left(bx\right)\mathcal{H}_l\left(x\right)\mathcal{H}_{l+2p+1}\left(x\right) &= 2^{l-1}\left(-1\right)^p\sqrt{\pi}l!b^{2p+1}e^{-b^2/4}\mathcal{L}_l^{(2p+1)}\left(b^2/2\right)\end{aligned} \tag{5.10}$$

where $\mathcal{L}_l^p(x)$ is the generalized Laguerre polynomial and $p \in N$. The final matrix of Hamiltonian will be

$$\begin{aligned}\langle l|H|m\rangle &= E_l\delta_{l,m} \\ &- E_J\cos(\varphi_{ext})\sqrt{\frac{2^l l!}{2^m m!}}(-1)^p\,\varphi_0^{2p}e^{-\varphi_0^2/4}\mathcal{L}_l^{(2p)}\left(\frac{\varphi_0^2}{2}\right)\delta_{m,l+2p} \\ &- E_J\sin(\varphi_{ext})\sqrt{\frac{2^l l!}{2^m m!}}(-1)^p\,\varphi_0^{2p+1}e^{-\varphi_0^2/4}\mathcal{L}_l^{(2p+1)}\left(\frac{\varphi_0^2}{2}\right)\delta_{m,l+2p+1}\end{aligned} \tag{5.11}$$

This is the Hamiltonian matrix in the Fock state basis. Only first few levels are interesting for qubits, it is sufficient to calculate the 30×30 matrix of the above Hamiltonian. Calculating large matrix slows the computation since the complexity of matrix eigenvalue computation scales as $O(n^3)$. The eignvalues and eigenvectors are obtained by numerically diagonalizing the above matrix. The elements of the eigenvector along with the wavefunctions of the harmonic oscillator in Equation 5.7 is used to obtain the Fluxonium eigenstates.

5.1.2 Energy spectrum and flux dependence

The potential of Fluxonium qubit and the eigenvalues are shown for different external magnetic flux in Figure 5.2a-5.2c. The spectrum is calculated for E_J=10GHz, E_C=2GHz and E_L=0.5GHz for Φ=0, $0.25\Phi_0$ and $0.5\Phi_0$ in a, b and c of Figure 5.2 respectively.
The black dotted line represents the inductive energy and the blue solid lines shows the full potential of the Hamiltonian. The first five eigenvalues of the Fluxonium qubit in terms of frequencies (f_g-f_i) are given in dashed lines. As the external flux bias changes from 0 to $0.5\Phi_{ext}$, the potential of Fluxonium qubit changes from perturbed parabolic potential to a double well potential. This change in potential also changes the energy levels of the eigenstates which is clearly reported in Figure 5.2a-5.2c.
The transition frequency between the ground state and the other excited states (f_{ge}-f_{gi}) as a function of applied magnetic flux is readily observable in Figure 5.2d. At integer quantum of flux, the energy difference between ground state and first excited state is close to the difference between ground state and second excited state. At half integer quantum of flux the difference between the energy difference is maximum and the transition frequency (f_{ge}) is minimum. The transitions at half and full integer of quantum of flux are called the sweet spots because the qubit transition f_{ge} verifies $df_{ge}/d\Phi_{ext} = 0$. Due to this property, the qubit is immune to low frequency flux noise in first order. However transition at half integer quantum of flux is preferred for computation due to large anharmonicity and low probability to excite the second excited state from the ground state, which leads to very low leakage error which is common in Transmon qubit [81].

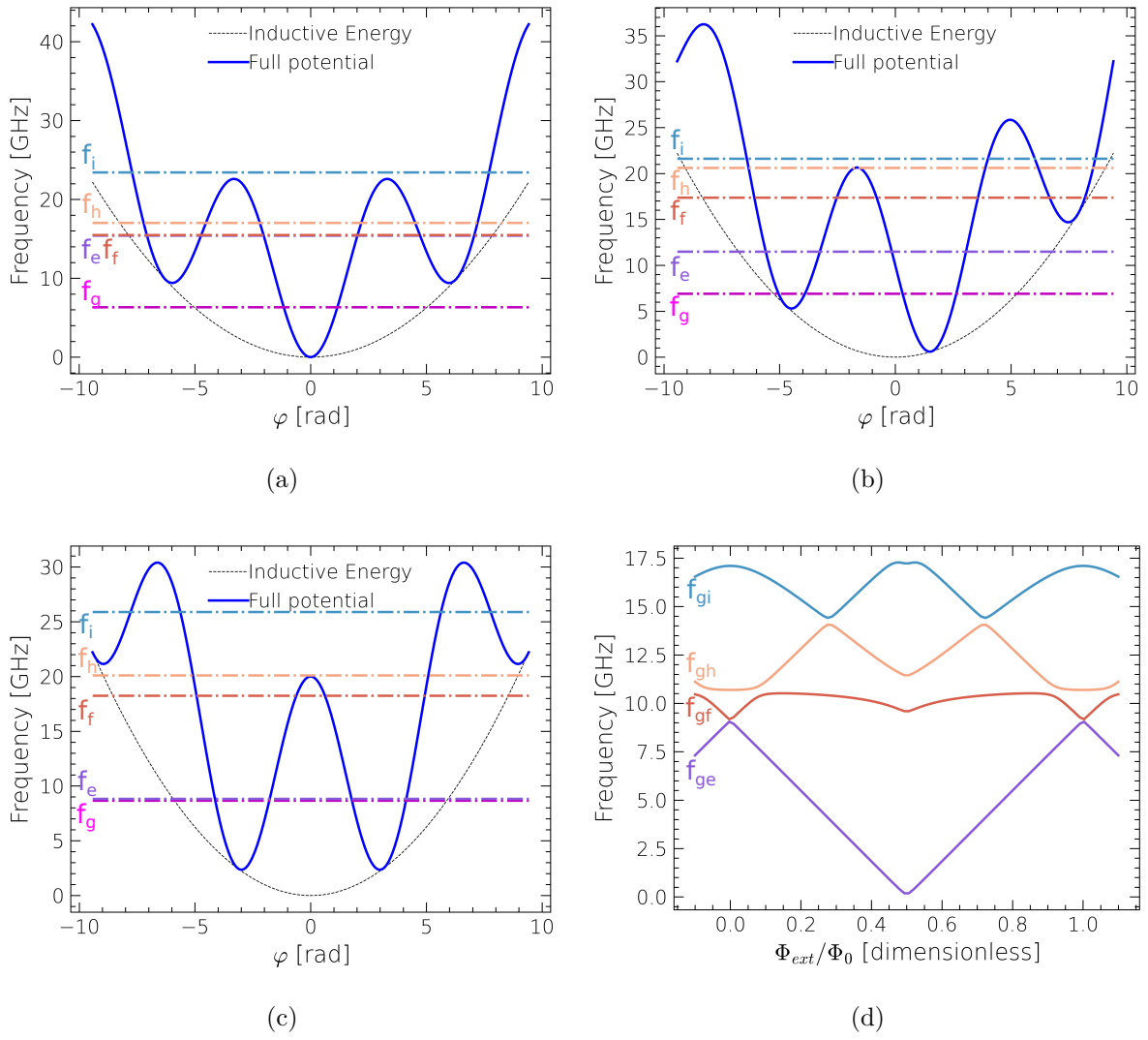

Figure 5.2: Potential energy with eigen frequency as a function of phase for (a) $\Phi_{ext} = 0$, (b) $0.25\Phi_0$ and (c) $0.5\Phi_0$. (d) Transition frequency as a function of reduced applied flux.

The energy spectrum can be changed by the three energies namely E_J, E_C and E_L since the ficticious particle mass and frequency depend on them (see Equation 5.4.) The typical values of these energy scales are: $E_J = 8 - 12GHz$, $E_C = 1 - 3GHz$ and $E_L = 0.3 - 0.6GHz$. In order to obtain such low E_L one needs a very high dissipationless inductance L of about 150-300nH.

5.1.3 Achieving large inductance: Superinductance

Superinductors are used for fulling such a demand of large inductance by the qubit. A superinductor can be defined as an inductor which is superconducting, frequency indepen-

dent and whose impedance (Z_0) is larger than quantum resistance (R_Q) i.e. $|Z_0| > R_Q$.

$$\begin{aligned} R_Q &= \frac{h}{(2e)^2} \simeq 6.5k\Omega \\ Z_0 &= j\omega L \end{aligned} \tag{5.12}$$

where L is the superinductance.
Inductance per square of simple superconducting wires are very small even though there dissipation is negligible as realized in the resonator part of the thesis ($< 1pH/\square$). Hence they are impractical to achieve superinductance. One other way to realize a superinductance is to use dirty superconductor nanowires like granular Al [82] or NbN [83] with inductance ($0.1nH/\square$). The advantage of dirty superconductors is the simplicity of the fabrication. The disadvantage is, it becomes hard to control properties such as phase slips [84] which are dissipative. Efforts are currently underway to reduce these phase slip rates [85]. More details on phase slips are given in section 5.2.2.
The well defined way to obtain high inductance is by using Josephson junction chains [86] where the size of junction can be adjusted to reduce phase slips. More details are provided when the attributes of the chain are explicitly discussed. By adding N such junctions in series, the resulting inductance is:

$$\begin{aligned} L &= N \times L_J \\ \text{where } L_J &= \frac{\Phi_0}{2\pi I_C \cos(\varphi)} \end{aligned} \tag{5.13}$$

where L_J is the inductance of individual junctions known as Josephson inductance calculated from Equation 1.2 and 1.3. When the phase difference(φ) between the two leads of the junction are small, which is true for a series of junctions in a loop, the cosine term can be ignored.

5.2 Attributes of Josephson junction chains

A chain of JJs is used to achieve the large inductance values required in a Fluxonium qubit. In this section, the validity and design limitation of such chains is discussed. The two design limitations discussed are the modes of the chain of JJs and the phase slips in the chains which causes dissipation.

5.2.1 Modelling chain of Josephson junction

The chain of junctions consists of series of Josephson junctions and each junction has a ground capacitance C_G. This has been discussed in literature extensively [87][88]. The size of junctions are chosen in this work such that the chain behaves inductively below $8GHz$

since the $|g\rangle$ to $|e\rangle$ transition frequencies (f_{ge}) of most of the qubits designed in this work are below $8GHz$.

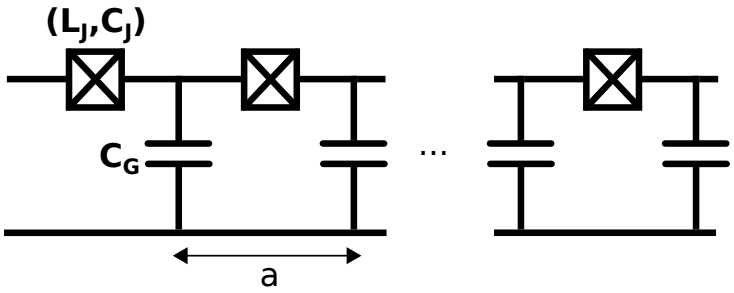

Figure 5.3: Chain of JJs with inductance L_J and capacitance C_J grounded by capacitance C_G.

The model of the chain is shown in Figure 5.3, where the junction inductance L_J is in parallel with the junction capacitance C_J and a is the unit cell length of the chain. The junction capacitance C_J is estimated by considering a parallel plate capacitance $C_J = \epsilon_0 \epsilon_r A/d$ where $\epsilon_r = 10.5$ is the relative permittivity of aluminum oxide. This leads to a capacitance per unit area of $50\text{fF}/\mu m^2$, since the thickness of junctions used in this work is about 2nm. This will be discussed further in the fabrication chapter. The thickness of the Silicon wafer used is around $300\mu m$, which yields an estimated ground capacitance of $\simeq$0.15fF for a given area of $4\mu m$ the junction. In this work, the plasma frequency of the junctions of the chain i.e. $\omega_P = 1/\sqrt{L_J C_J}$ is around 16GHz.
Since the chain carries alternating current through it, it can be treated as a transmission line. The chain hence could have resonant modes which produce standing electromagnetic waves. The dispersion relation which defines the resonant modes as a function of the wavevector k in the chain of JJs is given by (formula 5.36 of [89]):

$$\omega(k) = \frac{1}{\sqrt{L_J C_J}} \sqrt{\frac{1 - cos(k\mathsf{a})}{1 - cos(k\mathsf{a}) + C_G/2C_J}} \tag{5.14}$$

When $k\mathsf{a} << \sqrt{C_G/2C_J}$ and $k\mathsf{a} << 1$, the linear dispersion relation is given as $k\mathsf{a}/\sqrt{L_J C_G}$.
The number of junctions N can be defined using the open boundary conditions on the above circuit such that:

$$N\mathsf{a} = n\pi/k \text{ for } n = 1, 2, ..N-1 \tag{5.15}$$

If the first resonant mode of the chain is chosen to be more than 8GHz which is the maximum operating frequency f_{ge} of the qubits designed, the number of junctions required is approximately 100. In this work, 97 junctions are used to achieve an E_L of $0.5GHz$ with a self resonance of $8GHz$ below which the chain behaves as an inductor.

5.2.2 Phase slips in Josephson junctions of the chain

Phase slip is a phenomenon where the phase across the superconducting junction or wire changes by 2π due to fluctuations. Such phase-slips are dissipative [90], which creates relaxation channels for the qubit [91].
In Equation 5.13, the Josephson inductance L_J is inversely proportional to the critical current I_C. By using smaller critical current through small JJs, larger inductance L can be achieved with less number of JJs, but this would induce an increase of the phase slips. The phase slip amplitude E_{PS} between the sinusoidal potential wells of the junctions is given by [92][93]:

$$E_{PS} = 16\sqrt{E_J E_C/\pi}(E_J/2E_C)^{1/4}\exp -\sqrt{8E_J/E_C} \tag{5.16}$$

To be more intuitive, the energy bands of the individual junctions in the chain as a function of phase difference across their leads are shown in Figure 5.4a. The discrete energy bands within these wells are shown by different colors. The energy bands are calculated by solving Mathieu's equation using Python library functions. The tunneling of the fictitious particle between wells with degenerate energy levels causes the phase slip. The tunneling rate is called the phase slip rate or amplitude. The phase slip amplitude as a function of E_J/E_C ratio is plotted in Figure 5.4b, considering $E_J = 100GHz$.

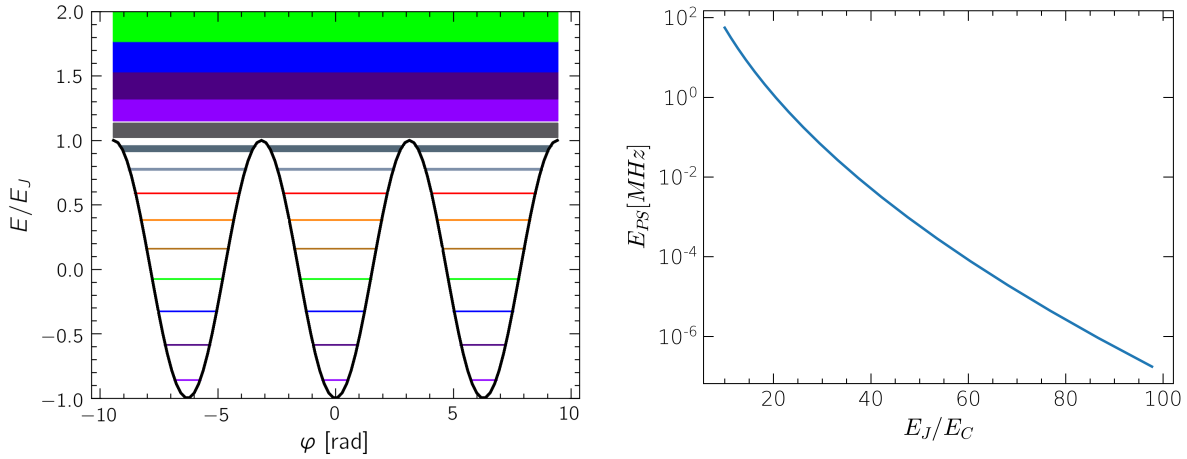

(a) (b)

Figure 5.4: (a) Potential energy and energy bands as a function of reduced phase for $E_J/E_C = 100$ and (b) Phase slip amplitude as a function of E_J/E_C.

As it can be seen, the phase slip amplitude reduces from a few tens of MHz for $E_J/E_C = 10$ to less than 1Hz for $E_J/E_C = 100$. Therefore, in this work, junctions in the chain are designed with E_J/E_C close to 100 so that the phase slip rate is less than 0.5Hz. On a side note, due to large E_J/E_C, the junction becomes insensitive to charge noise.

5.3 Qubit coupling to environment

Previously the Fluxonium circuit was considered to be an isolated artificial atom. However the qubit needs to be coupled to the external environment to be able to measure and manipulate it. The process of coupling the qubit to the environment is discussed in this section.

5.3.1 The system components

The qubit is driven by microwave source. The microwave is sent through the transmission lines as shown schematically in Figure 5.5.

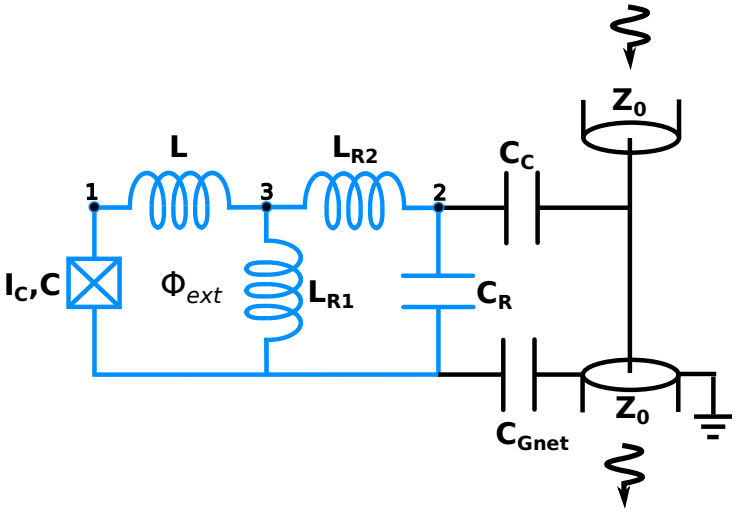

Figure 5.5: Qubit coupled to the environment via a transmission line. The qubit and the resonator are shown in blue color.

The qubit is coupled to a resonator with capacitance C_R. The coupling chosen in this work uses inductive coupling with a common inductor L_{R1} between the qubit and the resonator. The inductance of the bare resonator is $L_{R1} + L_{R2}$. Inductor L_{R1} is also part of the Fluxonium qubit where the total inductance in the loops is $L + L_{R1}$. On a side note, the qubit can also be capacitively coupled as discussed in reference [94]. C_C is the coupling capacitance between the resonator and the microstrip transmission line with impedance Z_0.

5.3.2 Qubit-resonator coupling

The coupling between the qubit and resonator can be calculated by circuit analysis. In the Figure 5.5, the numbers in the figure represent the nodes with respective phases φ_1,

φ_2 and φ_3. The Lagrangian of the circuit shown in blue can be written as

$$\begin{aligned}\mathfrak{L} =& C\Phi_0/2\dot{\varphi_1}^2 + C_R\Phi_0/2\dot{\varphi_2}^2 - \frac{E_L}{2}(\varphi_1-\varphi_3)^2 - \frac{E_{L_{R2}}}{2}(\varphi_2-\varphi_3)^2 \\ &- \frac{E_{L_{R1}}}{2}{\varphi_3}^2 + E_J\cos(\varphi_1-\varphi_{ext})\end{aligned} \tag{5.17}$$

where all energies are described by the same notation as in Equation 5.1.
By applying Kirchhoff's current law to the two loops and expressing φ_3, in terms of φ_1 and φ_2, the Lagrangian changes to

$$\begin{aligned}&\mathfrak{L} = C\Phi_0/2\dot{\varphi_1}^2 + C_R\Phi_0/2\dot{\varphi_2}^2 - E_{L_1'}\varphi_1^2 - E_{L_2'}\varphi_2^2 - E_M\varphi_1\varphi_2 + E_J\cos(\varphi_1-\varphi_{ext}) \\ &\text{where } E_{L_1'} = \frac{(\Phi_0/2\pi)^2}{L}\left(1-\frac{L_{tot}}{L}\right);\ E_{L_2'} = \frac{(\Phi_0/2\pi)^2}{L_{R2}}\left(1-\frac{L_{tot}}{L_{R2}}\right) \\ &\text{and } E_M = -\frac{2L_{tot}(\Phi_0/2\pi)^2}{LL_{R2}} \text{ where } \frac{1}{L_{tot}} = \frac{1}{L}+\frac{1}{L_{R1}}+\frac{1}{L_{R2}}\end{aligned} \tag{5.18}$$

The Hamiltonian of the system is then given as:

$$\begin{aligned}&H = H_{qubit} + H_{resonator} + H_{coupling} \\ &\text{where } H_{qubit} = 4E_C\hat{n_1}^2 + \frac{E_{L_1'}}{2}\hat{\varphi_1}^2 - E_J\cos(\hat{\varphi_1}-\varphi_{ext}); \\ &H_{resonator} = 4E_{C_R}\hat{n_2}^2 + \frac{E_{L_2'}}{2}\hat{\varphi_2}^2; \\ &H_{coupling} = -\frac{E_M}{2}\hat{\varphi_1}\hat{\varphi_2}\end{aligned} \tag{5.19}$$

where $\hat{n_1}$ and $\hat{n_2}$ are the conjugate variables of the phase operators $\hat{\varphi_1}$ and $\hat{\varphi_2}$. The Fluxonium and the resonator Hamiltonian H_{qubit} and $H_{resonator}$ are then retrieved. $H_{coupling}$ describes the coupling between the qubit and the resonator. The phase operator $\hat{\varphi_2}$ can be expressed as a function of creation and annihilation operators as follows:

$$\hat{\varphi_2} = \varphi_0(\hat{a_2} + \hat{a_2}^\dagger)/\sqrt{2} \tag{5.20}$$

The coupling Hamiltonian therefore can be rewritten as:

$$H_{coupling} = -\frac{E_M\varphi_0}{2\sqrt{2}}(\hat{a_2} + \hat{a_2}^\dagger)\hat{\varphi_1} = -g_0(\hat{a_2} + \hat{a_2}^\dagger)\hat{\varphi_1} \tag{5.21}$$

where $\varphi_0 = \left(8E_{C_R}/E_{L_2'}\right)^{\frac{1}{4}}$ and $g_0 = E_M\varphi_0/2\sqrt{2}$ is the coupling strength between the qubit and the resonator.

Chapter 6

Design and fabrication

This chapter is divided into two parts. The first part deals with the design of the sample. The second part of this chapter explains the fabrication process used to obtain the qubit sample and the DC characterization of the junctions fabricated.

6.1 Design of the system

The qubit system is designed using GDS with Klayout software. The design is shown in Figure 6.1 with labels of individual parts and it involves three layers of patterns for three levels of exposure given in the figure. For the structure where dimension accuracy is less important, high current high dose is used. Two of the layers dedicated for small structures uses low current exposure for accurate dimensions.

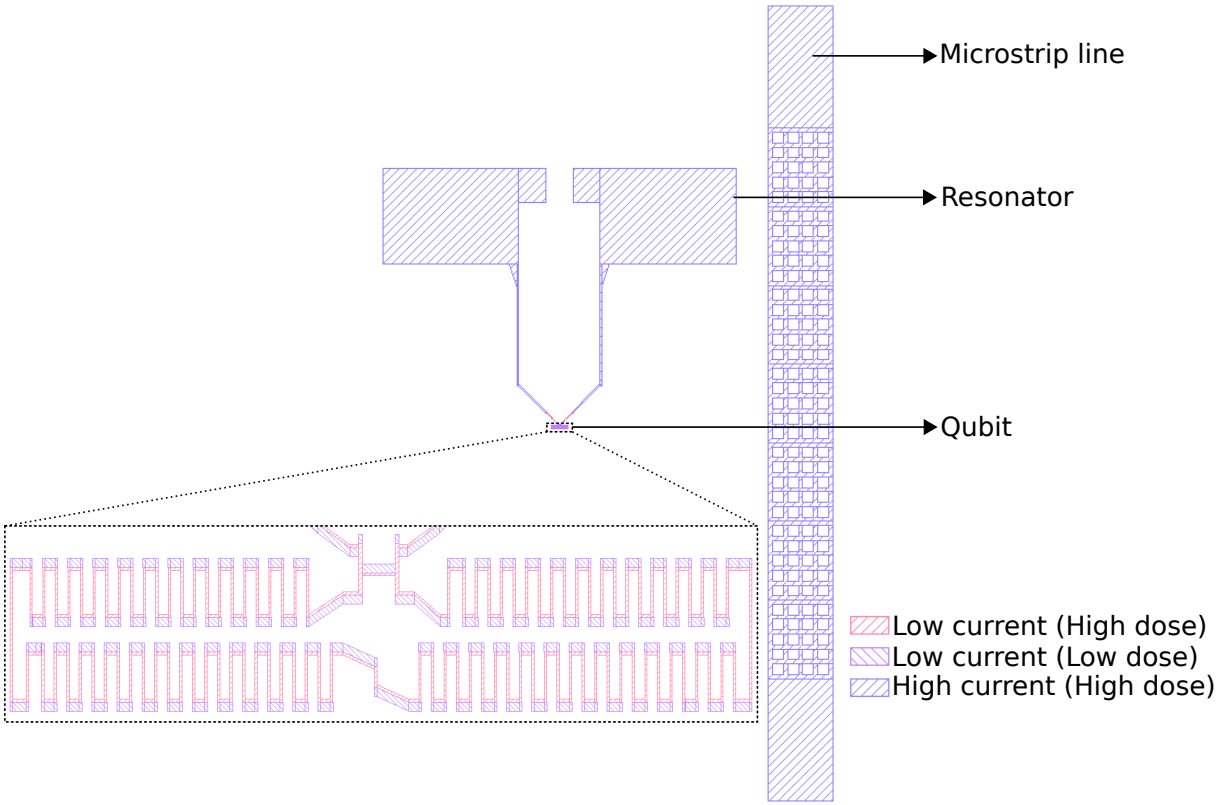

Figure 6.1: GDS drawing of the designed qubit

The microstrip line shown in the figure is designed as intricate mesh. Since supercon-

ductors repel flux, the mesh structure helps trapping the flux. The capacitor pads of the resonator are designed approximately $600\mu m$ away from the qubit. This distance is chosen to reduce any effects of flux creep, in the pads, on the qubit. This distance could be reduced further by using other designs such as mesh like structure in capacitor pads for flux trapping or using interdigitated capacitors. These designs would help for scaling of the qubit system.
The resonator capacitor pads are connected to the qubit with 2 common junctions which is the coupling inductor. Small strip in the bottom middle of the inset is designed to be the main small junction responsible for the tunneling of quantum of flux into or out off the loop. The loop consisting of JJ chains. Further explanation of the qubit sample is done in the fabrication section.

6.1.1 Resonator design optimizations

In this work, Fluxonium qubit is implemented in 2D architecture. There are other 2D designs available in the literature [9][26]. However, this work uses a lumped element resonator for coupling the qubit to the environment. This reduces the layout space and improves scalability.
In order to optimize the design, HFSS software is used to estimate the resonator frequencies and field distributions. The Figure 6.2a shows the model of the resonators in HFSS which is simulated both in Eigen mode and Driven modal. Eigen mode simulations are performed to extract the eigen modes of a resonant circuit. Whereas in Driven modal, the transmission coefficient as a function of frequency is simulated.
The green color in the figure represents a 300 um thick Si substrate, while the pink structure shows the two resonators and the microstrip line. The resonator is modelled using perfect conductor boundary condition for capacitors and a lumped element impedance for the inductors in the design.
By changing the value of lumped element inductance, different frequencies are attained. This is used to calculate the capacitance:

$$C_R = \frac{1}{L_1 - L_2}\left(\frac{1}{\omega_1^2} - \frac{1}{\omega_2^2}\right) \tag{6.1}$$

where L_1 and L_2 are the simulated inductances of the resonator resulting in angular frequencies of ω_1 and ω_2 respectively. The capacitance estimated from the eigen mode simulation is about 120fF.
The electric field distribution in the resonator obtained from simulation is shown in Figure 6.2b. The red and blue color represents the highest and lowest electric field amplitude respectively. It can be seen that the electric field is largest close to the lumped element inductor. Hence, the dielectric loss could be large close to the inductor.

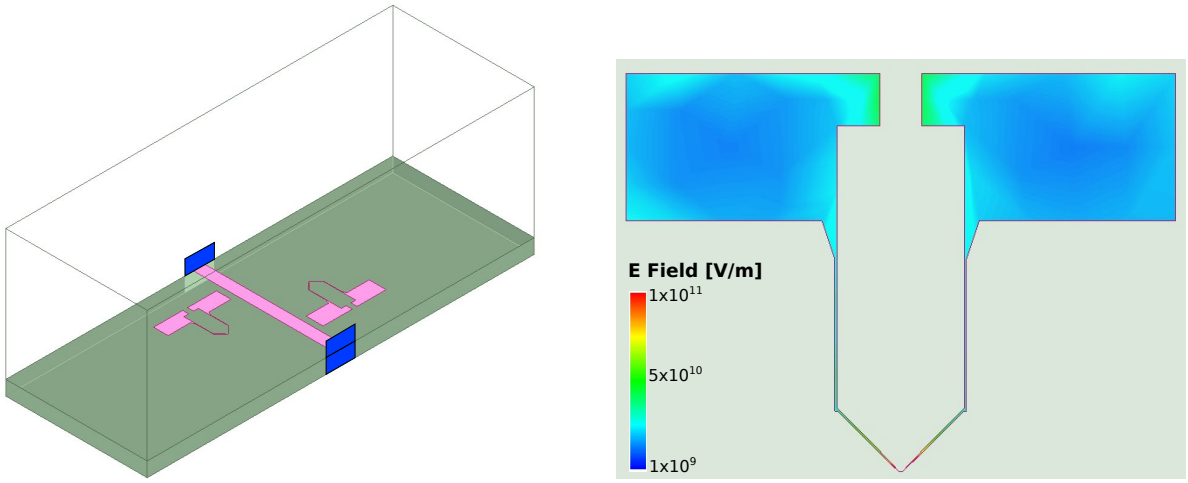

(a) (b)

Figure 6.2: (a) Modelled device with two resonators and microstrip line connected to two ports represented by blue color on Si substrate represented by green color and (b) electric field distribution in one of the resonators.

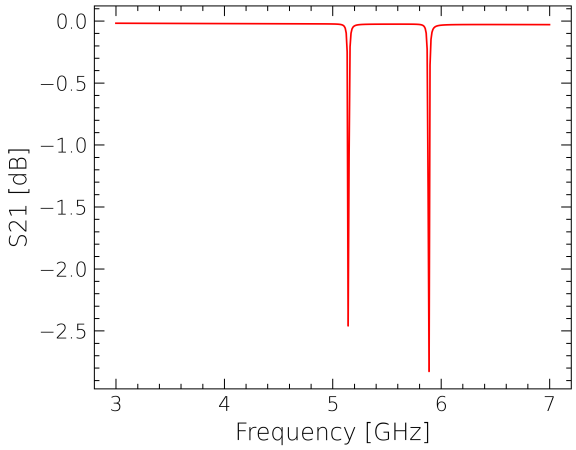

Figure 6.3: Simulated S_{21} as a function of frequency with the two resonances corresponding to the two different resonators coupled to the transmission line.

In the driven modal simulation, the signal is applied through ports shown as blue rectangles in Figure 6.2a. They excite the microstrip line by sweeping frequency from $3GHz$ to $7GHz$. The results of such simulation are the scattering matrix elements. The transmission coefficient S_{21} as a function of frequency is plotted in Figure 6.3. The two resonators simulated have two resonances.

The resonator frequency observed from the eigen mode and from driven model are different. This is because of the additional coupling capacitance C_C. The coupling capacitance responsible for this frequency shift is calculated using the reference [95] is found to be ∼12fF.

With this simulation, the coupling capacitance and resonator capacitance are estimated. The actual value of capacitances are however obtained by fitting the experimental data.

6.2 Fabrication

The fabrication of the qubit is made by lift-off method using e-beam lithography. The samples are prepared using a single side polished Silicon (Si) wafer of a 2 inch diameter and 280-300μm thickness. The junctions are fabricated by in-situ oxidation. The process flow and recipe is discussed in this section.

6.2.1 Process flow

The process steps are shown below:

1. **Ground plane sputtering**: The sample needs a ground plane provided by metal deposition on the unpolished side of the wafer. The polished surface is covered with photoresist to protect the surface from dust and other particle contamination. The sputtering is done in a commercially available Alliance Concept DP850 magnetron sputtering system. The ground plane consists of a 450nm of Cu layer on top of 20nm of Tantalum(Ta) which acts as an adhesion layer. After the sputtering, the resist on the polished side is removed using acetone and IPA. The sample is blow dried with N_2 gas. Further cleaning is done using O_2 plasma with 20W power for 20s.

2. **Spin coating**: The sample is spin coated with two layers of resist to achieve required thickness. These are positive e-beam resists. The bottom layer consists of Polymethyl methacrylate (PMMA) and copolymer methacrylic acid(MAA) and top layer consists of PMMA. The pictorial representation of the spin coated sample is shown in Figure 6.4a. The grey color represents the Si substrate, blue layer represents PMMA/MAA 9% and green layer represents PMMA 4%. The sample is baked at very high temperatures to dehydrate the polymers and copolymers.

3. **e-beam lithography**: Beam of electrons accelerated by 80keV as used for lithography. These beams are used to cause scission of the polymers of the resist because broken polymers are soluble in developer solvents. Nano-beam Ltd. NB5 electron beam lithography machine is used for making patterns. Resist layer with densely pack long chain polymers and copolymers, which enhance the sensitivity to e-beam exposure, are easily broken with smaller dose of electrons. However, low concentration long chain polymers, requires larger dose of e-beam since polymers are sparsely distributed. Therefore to remove top layer of resist larger dose of electrons are required in comparision with bottom layer.

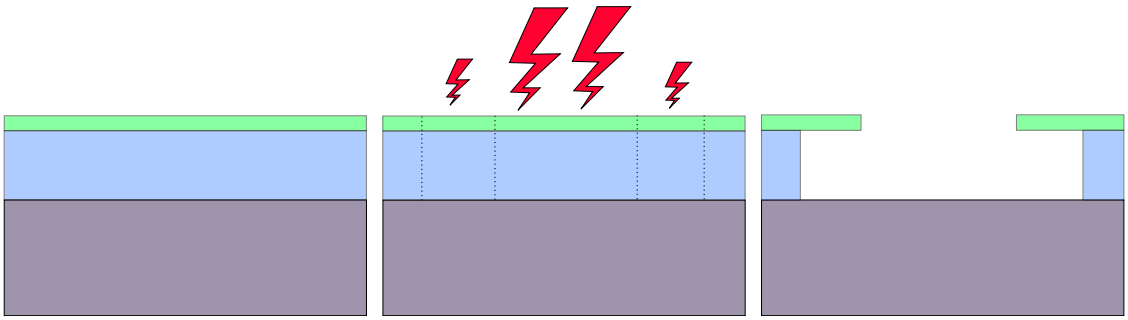

Figure 6.4: Representation of (a) spin coating of bilayer resist, shown in blue and green colors, (b) e-beam lithography with lightening bolts representing e-beams with different density of electrons and (c) developed sample with undercuts.

The design shown in Figure 6.1 is fed to the lithography machine. For small structures, it can be seen in Figure 6.4b that the two different doses (represented by two sizes of lightening symbol) are applied to the resist. These corresponds to the two low current doses labelled in Figure 6.1. Low current of electrons provide very precise dimensions of the structures. Since very high precision in dimensions is not required for big structures such as microstrip line or capacitor pads, dose with high current is applied.
The design pattern is exposed in parts, with the help of a moving base to move the substrate and deflection coils to move the e-beam. The area of exposure for a given instance is $20 \times 20 \mu m^2$ and between different areas e-beam is deflected. After exposing every $500 \times 500 \mu m^2$ area, the base moves. Hence it is important to have the e-beam focus clearly defined for samples to not have an discontinuities i.e. stitching error.

4. **Development**: Development is performed with a solvent bath of MIBK:IPA in 1:3 ratio where the exposed polymers are dissolved. The residues are cleaned with IPA bath and the sample is blow dried with N_2 gas. Further cleaning is done using RIE with O_2 plasma for 15s with 10W power. Figure 6.4c represents resist structure in the developed sample. The top layer PMMA are not broken by small dose of e-beam. This creates an undercut, where top layer resist remains while the bottom layer resist is removed. PMMAs are very stiff materials which are hardened by baking. The resist of few hundred nanometers of thickness would not bend due to gravity. Hence it is useful for creating hanging structures.

5. **Evaporation**: The junctions of Al-AlOx-Al is made by evaporation process. The evaporation involves two angles for depositing two overlapping layers of Al electrodes to obtain the junctions. These junctions can be obtained using resist as mask (also known as Dolan bridge technique [96]) or using undercuts (also known as bridge

free technique) which was developed in my group [97]. For my Fluxonium samples, undercut technique is used. As shown in Figure 6.5a, the first deposition is made at 35° perpendicular to the substrate. After the deposition of the first layer of Al represented by the blue layer, 4 Torrs of oxygen is introduced into chamber for 5 minutes to create the AlOx layer of the junction shown as red line. This creates an oxide layer of about 2nm. Another layer of deposition is made at -35° as shown in Figure 6.5b to obtain the junction.

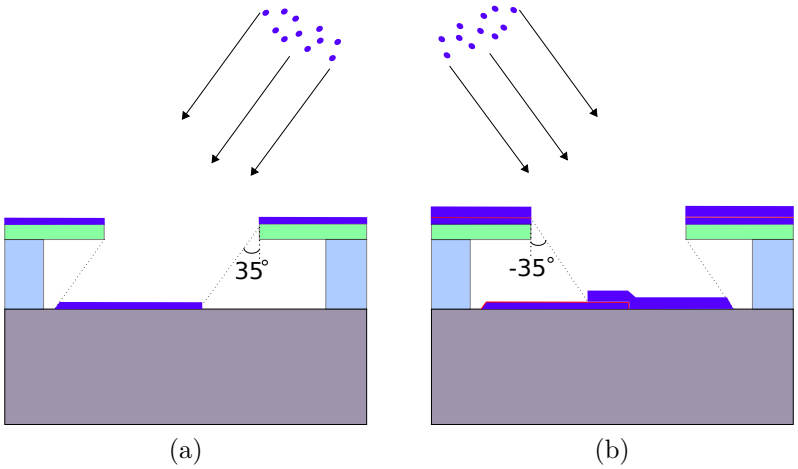

Figure 6.5: Representation of double angle evaporation process with 35° perpendicular to the substrate surface.

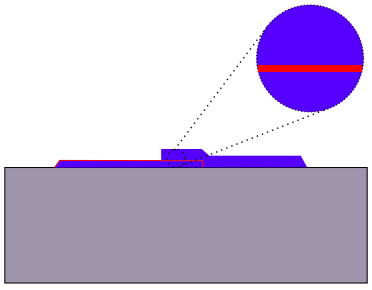

Figure 6.6: Final sample with the junction

6. **Lift-off**: The resist used as mask is removed in the final step of the fabrication using a NMP solution. The residues are cleaned using an IPA bath and sample is blow dried with N_2 gas. To remove resist residues further, RIE with O_2 plasma is done for 15s at 10W power. The final sample has junctions on Si substrate as represented in Figure 6.6.

The Silicon wafer is diced to obtain the final samples. The size of the diced samples is $4 \times 8mm^2$ with two qubits in each sample.

Process name	Equipment	Precision
Deposition	Alliance concept (DP850)	Ground plane Sputtering: 20nm (Ta) at 0.1nms^{-1} and 450nm (Cu) at 0.5nms^{-1}
Spin coating	PMMA/MAA 9%	4000rpm, 30 seconds (Achieved thickness:720nm)
Bake	Hot plate	200°C, 10 minutes
Spin coating	PMMA 4%	4000rpm, 30 seconds (Achieved thickness:235nm)
Bake	Hot plate	180°C, 5 minutes
e-beam Lithography	Nanobeam (NB5)	3Cm^{-2} dose for undercut with low current 11Cm^{-2} dose for junctions with low current 10Cm^{-2} dose for pads and Tx line with high current
Development	Developer	MIBK:IPA(1:3), 60s and IPA, 30s N_2 blow dry and O_2 RIE with 10W, 15s
Evaporation	Plassys (MEB550)	20nm at 0.1nms^{-1} O_2 at 4 Torrs for 5 minutes 50nm at 0.1nms^{-1}
Lift-off	Solvent	NMP with 80°C for 3 hours Acetone and IPA baths for 30 seconds N_2 blow dry and O_2 RIE with 10W, 15 seconds

Table 6.1: Recipe for qubit sample fabrication

6.2.2 Sample images and size

The optical image of the final sample is shown in Figure 6.7a. Optical image of the sample is taken using Ziess microscope in the Nanofab cleanroom of Neel Institute. The black region at the bottom of the optical image is the region where the qubit is present. Figure 6.7b shows the false colored SEM image of the qubit taken using Ziess+ Scanning electron microscope available at Neel Institute.

The blue color in Figure 6.7b represents the common junctions (i.e. the inductance common to the resonator and the qubit.) Green color represents the chain of junctions and red color represent the main small junction of the qubit.

Five different qubits were measured during this work. Table 6.2 shows the difference between the qubits measured in terms of the capacitor pad area, the small junction area and the coupling junction area. The sizes given in the table are obtained from the SEM

Sample name	Area(mm^2) (Capacitor pad)	Area(μm^2) (Main junction)	Area(μm^2) (Coupling junction)
A	0.175	0.1426	0.99
B	0.175	0.1426	0.69
C	0.15	0.1426	0.69
D	0.175	0.10695	0.99
E	0.15	0.10695	0.99

Table 6.2: Table summarizing difference in area between the measured samples

measurements of the sample. The areas of junctions of the chain are kept constant and

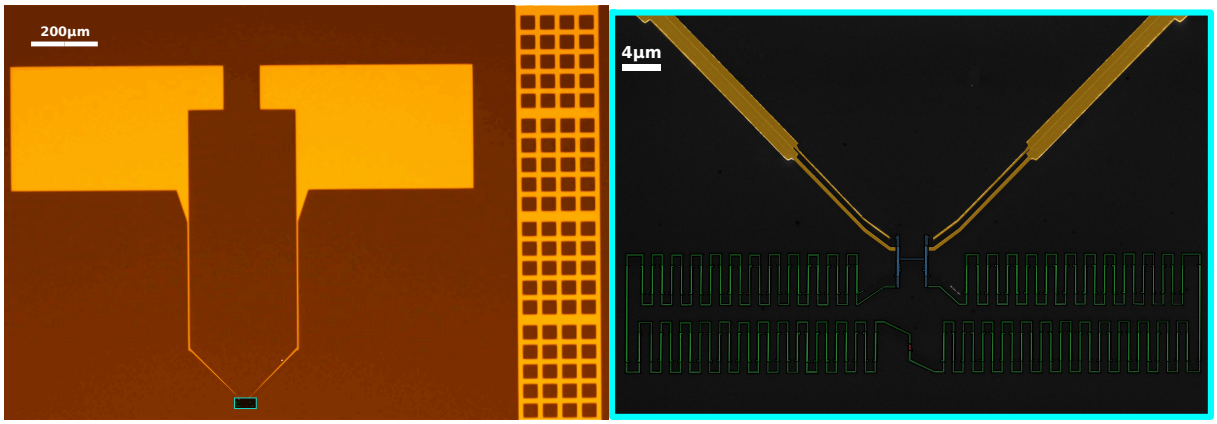

(a) (b)

Figure 6.7: (a) Optical image showing microstrip line and resonator, (b) False colored SEM image showing Fluxonium qubit.

it's value is $0.648\mu m^2$. These difference change the properties of the qubit which will be discussed in chapter 7.

6.2.3 Sample holder

To perform qubit measurements a double layered PCB is used. The PCB is designed using GDS and is fabricated at Neel Institute. The PCB is placed in a Copper RF box and connected with SMA connectors. The sample is placed in a Cu RF box as shown in Figure 6.8a. The microstrip line on the sample is connected to the microstrip line of the PCB using wedge wirebonding.

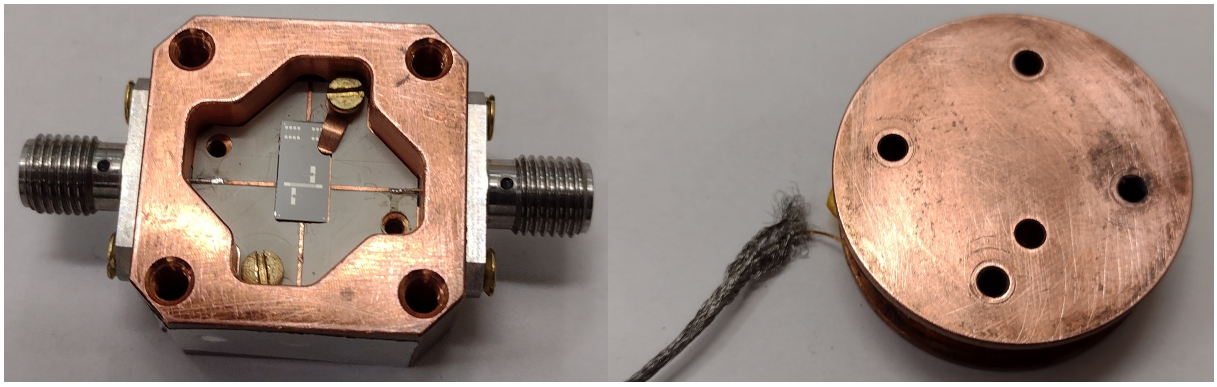

(a) (b)

Figure 6.8: (a) Photo of RF box with sample and (b) Photo of Coil holder.

The RF box is used as sample holder and provides thermal connections between the sample and the refrigerator. The SMA connectors on the RF box are the ports used to connect to the input and output lines of the microwave setup.
The coil shown in Figure 6.8b is used to apply the external flux to the qubit. The coil is

made out of superconducting wires held in a Cu frame. The coil is anchored to the RF box to have no spatial fluctuations of the flux in the qubit loop. This constitutes the basic block of device under test (DUT).

6.2.4 DC measurements

Before measuring the qubit, to gauge the quality and the yield of the junctions in the fabricated batch and to estimate the value of junction energy before cooling down the sample, room temperature DC measurements are performed. A 2-probe measurement is done using a probing station at Neel Institute. A Keithley 2400 current source is used for sending a DC current sweep through the pads shown in the SEM image of Figure 6.9a and the voltage drop across the pads is measured by Keithley multimeter. A room temperature resistance is hence calculated from such measurements.
As shown in the SEM image, there are four different samples. It has 0,1,2 and 3 junctions respectively between each pair of pads. By measuring the resistance across each of these pads, the resistance as a function of junction number is plotted in Figure 6.9b. The blue dots are the measured values of resistance and the red line is a linear fit to obtain the slope which gives the actual resistance per junction.

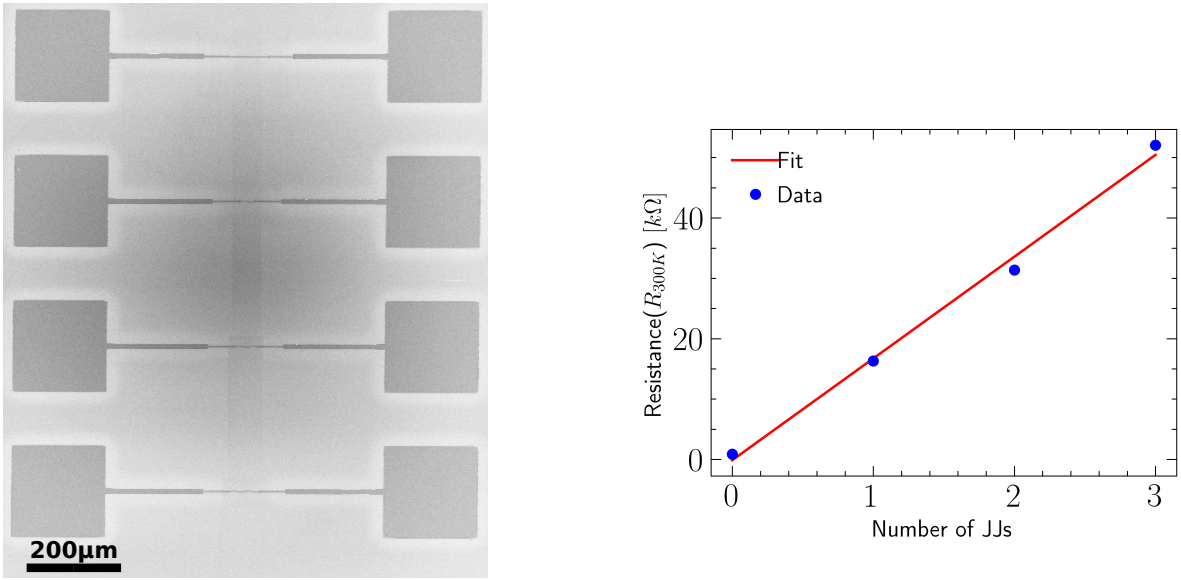

(a) (b)

Figure 6.9: (a) SEM image of the 2-Probe sample set consisting of different number of junctions and (b) DC measurement of the junctions.

The critical current I_C is related to the residual normal resistance of a Josephson junction

by the Ambegaokar-Baratoff formula [98]:

$$I_C(T) = \frac{\pi \Delta_{Al}}{2e} tanh\left(\frac{\Delta_{Al}}{2k_B T}\right)\frac{1}{R_n} \tag{6.2}$$

where Δ_{Al} is the superconducting gap of the electrodes of the junction (which is 210μeV in our labs case) and R_n is the residual normal state resistance of the junction above superconductor-normal metal transition temperature. It is found that from room temperature to low temperature above transition the resistance of the junction increases by about 30%. Hence $R_n = 1.3R_{300K}$. The junction operates at a temperature of 20mK hence the contribution of tanh term can be ignored. Therefore the critical current would be

$$I_C = \frac{\pi \Delta_{Al}}{2e}\frac{1}{1.3R_{300K}} \tag{6.3}$$

Hence the estimated value for E_J for this particular set of junctions is $7.5GHz$. This of course is an estimation. The real values come from the spectroscopic measurements reported in Chapter 7.

Chapter 7

Measurements and analysis

This chapter is divided into five parts. The first part involves description of the measurement setup for spectroscopy and time domain measurements. In the second part, spectroscopy data and extracted parameters are discussed. The third part involves explanation of the physics and the experiments of various time domain measurements done on the qubit. The forth part discusses the contribution of the different dissipation mechanisms in Fluxonium. Finally, the various noise sources involved in qubit decoherence are discussed in the fifth part.

7.1 Measurement setup

Since there are multiple measurements performed, the setup can be divided into three parts. Firstly, there is a part of setup common between spectroscopy and time domain measurements. This is the setup within the fridge. Next is the spectroscopy measurement setup of the resonator and the qubit. Lastly, there is the time domain measurement setup for various pulse measurements.

7.1.1 Fridge setup

There are seven samples measured during this work with two of them measured at IBM Zurich and the other five at Neel Institute. The samples are measured at low temperatures of 13mK in case of IBM and 25mK in Neel Institute's case, for which dilution refrigerator is used. Both places use Bluefors dry fridge and the schematic of the setup is shown in the Figure 7.1.
The DUT is connected to a Cu column at the base plate of 25mK for thermalization. The DUT is enclosed in a Cryoperm and IR shield. This protects the qubit from any IR radiations and magnetic field fluctuations coming from the outside world.
The signal is transmitted to the fridge through Port 1 labelled in the figure. The signal passes through series of attenuators at different temperature stages. They are used firstly to attenuate any thermal photons coming from higher temperature stages and secondly, they thermalize the inner conductor of the coaxial cables.
The signal is filtered with a low pass filter (LPF) to prevent any high frequency signals from entering the DUT. For the same reason, another LPF is connected to the DUT's

output. Two isolators in series are added to the output line to avoid any reflection of the resonator signal back to the DUT. The output signal needs amplification to be detected by the measuring instrument. Hence a low noise HEMT amplifier from Low noise factory is used at 4K stage.

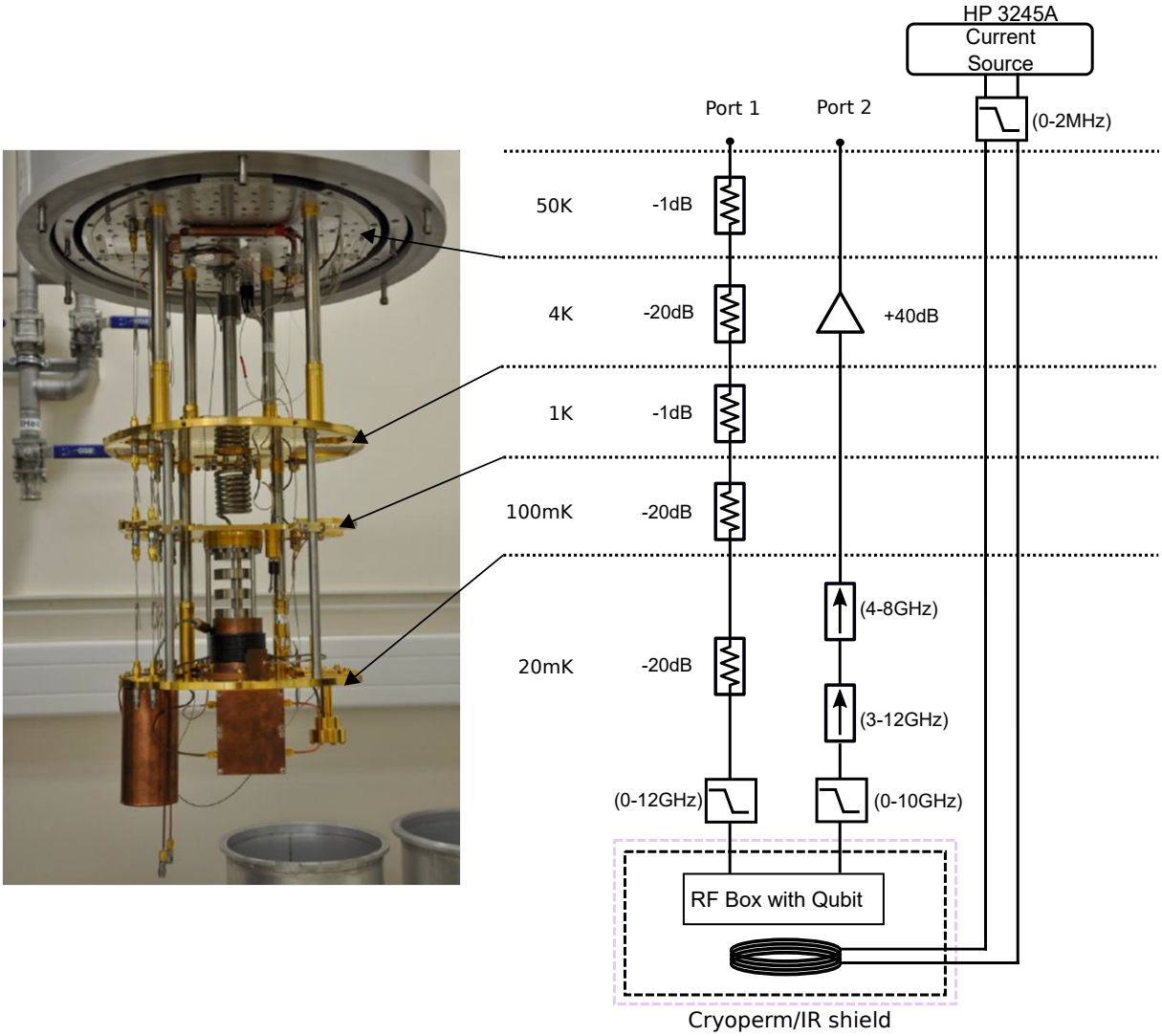

Figure 7.1: Part of measurement setup inside the refrigerator.

7.1.2 Spectroscopy setup

The spectroscopy of the resonator is done by single tone sweep using the vector network analyzer(VNA). The signal in the frequency range of the resonator is transmitted to Port 1 of the fridge. The signal is sent through the coupled port of the directional coupler as shown in Figure 7.2. The signal is received back from the VNA through Port 2 after amplification.

Differently, the spectroscopy of the qubit requires two tones. One tone is swept in the frequency range of the qubit and the other tone is used for observing the shift of resonance

of the resonator due to the coupling between the qubit and the resonator. In literature this is called the dispersive shift or χ shift [24].
The experiment is realized using a microwave generator to transmit a variable frequency to drive the qubit and the VNA measures the transmission coefficient at resonant frequency of the resonator. When the variable frequency matches the qubit frequency, the amplitude and phase of the transmission coefficient changes. This results in the indirect measurement of the qubit frequency.

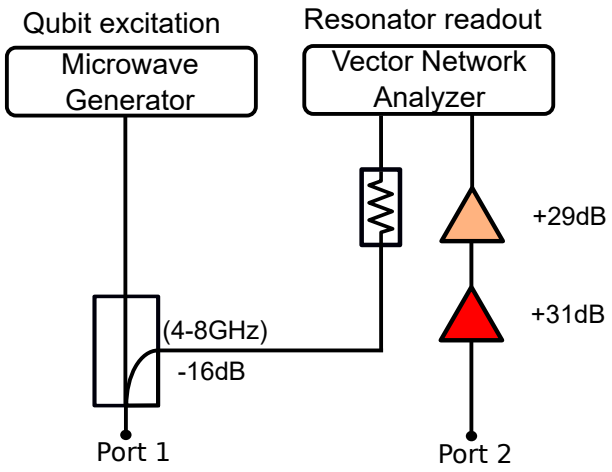

Figure 7.2: Setup for spectroscopy measurement

7.1.3 Time measurement setup

In order to obtain qubit properties, pulse measurements are performed. The setup of such measurements is represented in Figure 7.3. In order to create controllable pulses, an arbitrary waveform generator(AWG) from Tabor electronics is used. The AWGs are programmed using Python script to load pulsed waveforms into their memory so that the waveforms are sent out through the ports of AWGs until measurements are completed.
Pulses at qubit frequency f_{ge} are applied to excite the qubit. The pulses are generated using modulation mechanism. Continuous wave of frequency f_{LOq} from the microwave generator is up-converted to the qubit frequency such that $f_{ge} = f_{LOq} + f_{IRq}$ using single sideband (SSB) modulator or mixers. f_{IRq} is the frequency of the sinusoidal waveform of the AWG pulses.
For measuring the qubit state with the resonator, the resonator with frequency f_r is excited using the same modulation mechanism as for the qubit such that $f_r = f_{LOr} + f_{IRr}$ where f_{LOr} is the resonator microwave generator frequency and f_{IRr} is the frequency of sinusoidal waveform from the AWG.
In order to reduce leakage of the resonator photons from the generators into the samples in the fridge, a switch from minicircuits with a switching time of $35ns$ and isolation of 65dB is used. It is turned on only during the readout. This helps in avoiding readout

photons entering the sample during qubit operations [99]. The pulses are transmitted through some room temperature attenuators before passing the signal to the fridge so that only a few photons are sent into the sample through Port 1.

The signal received from the sample through Port 2 is amplified at room temperature. The

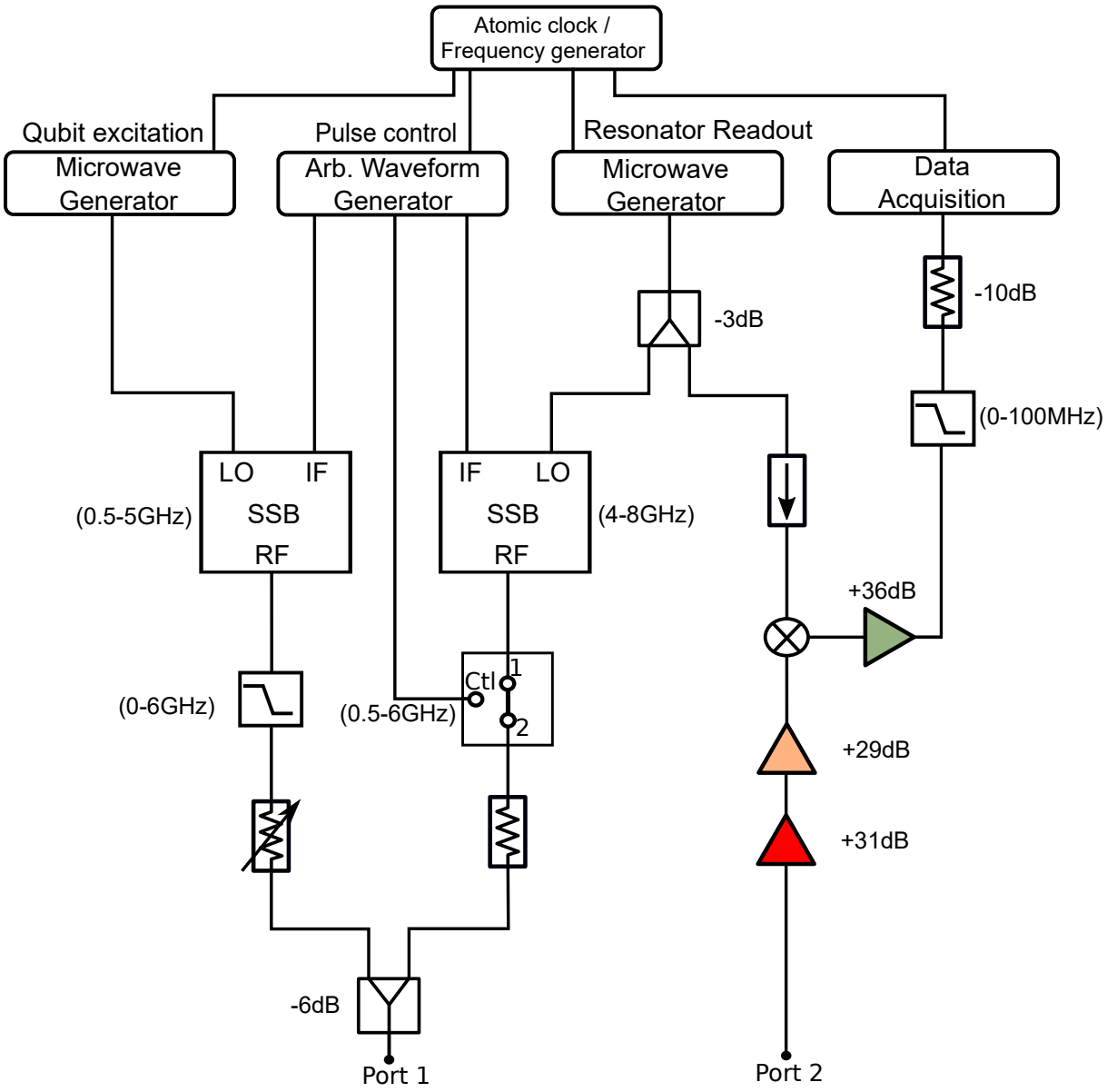

Figure 7.3: Setup for timed domain measurements

resonator signal due to its high frequency cannot be properly sampled and processed by our data acquisition card (DAC) which is from Alazar tech 9360. It only has a maximum sampling rate of 1.8GS/s. Hence the signal is down converted to f_{IRr} using a mixer. The intermediate frequency f_{IRr} which is 80MHz can be detected and acquired by the DAC. All the devices are synchronized by using a single master clock which is either an atomic clock (in case of IBM) or a clock generator (in case of Neel Institute).

7.2 Spectroscopy

This section is dedicated to the results from spectroscopy measurements. The spectroscopy of the resonator and the qubit are performed on five different qubit systems. Additionally, two more measurements are done on a pair of qubit systems that are aged for five months. Samples are named A-E chronologically, and B* and C* are the aged samples. Measuring these samples helps in understanding the qubit properties with change in junction area, coupling inductance and aging. Sample B and C have been measured at IBM Zurich under Dr. Stefan Filipp's supervision.

7.2.1 Resonator spectroscopy

The spectroscopy of the resonator is carried out by sweeping external flux. The flux sweep in sample A,D,E,B* and C* is performed using current source and for samples B and C using voltage source. The resonator spectroscopy of sample A and sample B as a function of flux are shown in Figure 7.4.

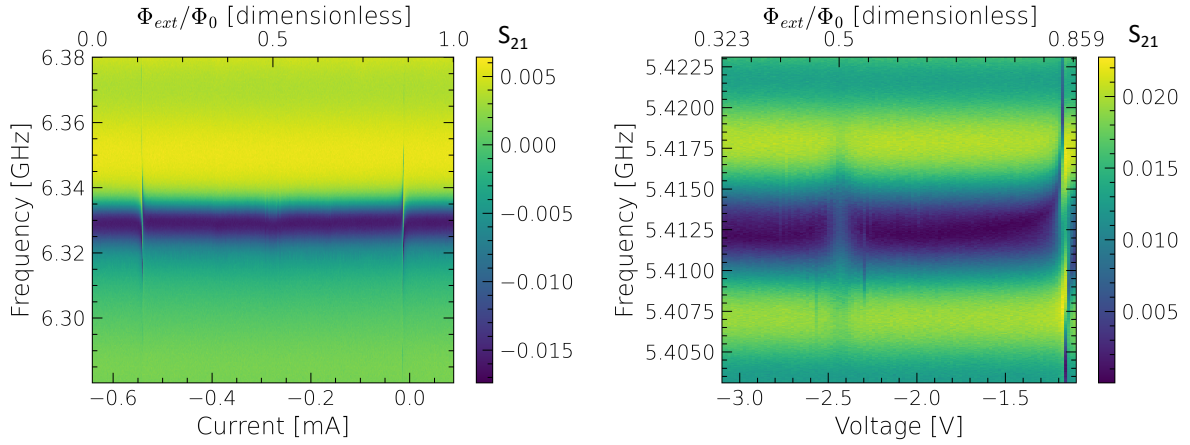

(a) (b)

Figure 7.4: Color mapped resonator spectroscopy of (a) sample A and (b) sample B, with frequency as a function of flux.

The dark blue color in the figures represent the resonant dips in the transmission amplitude and the greenish yellow part is the signal amplitude away from resonance.
In sample A, at -0.55mA and 0mA of current bias and for sample B at -1.1V voltage bias, one can see a shift in the resonator frequency. This is due to the anticrossing between the qubit and resonator frequencies. These anticrossings are symmetric with respect to half integer quantum of flux. By this signature anticrossing, one can confirm the existence or presence of the qubit.

7.2.2 Resonator spectroscopy model

In order to extract the parameters of the 2D resonators, I modelled the circuit using lumped element description. The model used for fitting the transmission coefficient of the measurements is shown in Figure 7.5. The asymmetry in the resonance are modelled as complex impedances X_E in series with transmission line impedance $Z_0 = 50\Omega$ [95].
The coupling capacitance C_C is connected in series with resonator having inductance L_R (the Fluxonium coupled to the resonator can be ignored due to its large inductance in parallel to the resonator inductance.) The capacitance of the resonator is C_R and R is the resistive loss of the resonator.
The transmission coefficient of a two port network is given [in table 4.2 of [100]] as

$$S_{21} = \frac{2}{A + \frac{B}{Z_0} + CZ_0 + D} \tag{7.1}$$

where $A = D = 1 + X_E/Z_L, B = 2X_E + X_E^2/Z_L, C = 1/Z_L$ by comparing the model with the two port network. Z_L is the load impedance which is the series impedance of coupling capacitor and resonator i.e. $Z_L = Z_{C_C} + Z_{resonator}$.

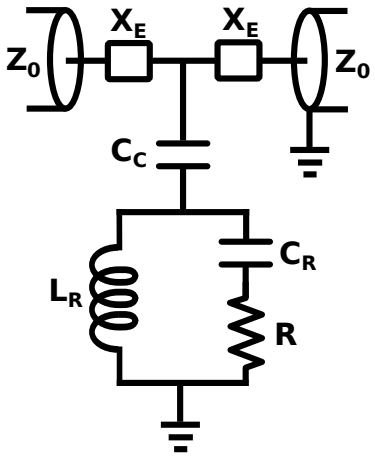

Figure 7.5: Model of the resonator coupled to a transmission line

When the flux is far away from the anticrossings and half flux points, one can find the undressed frequency of the resonator. The frequency sweep in such regions is chosen to fit the transmission coefficient of the resonators. Figure 7.6 shows the normalized transmission coefficient as a function of frequency across resonances of sample A and B resonators. The data is shown in red dots and its fit from the model in black solid line.
By fitting the S_{21} coefficient, one can extract the parameters shown in table 7.1. The geometric inductance L_{geo} of these resonators is calculated to be 1.16nH [101].
A couple of important conclusions from the fitting are: Firstly, the HFSS simulations gives results for capacitances of 120fF and 12fF for C_R and C_C which is close to the measured capacitances of 105fF and 10fF respectively. Secondly, with a sample aging of five months,

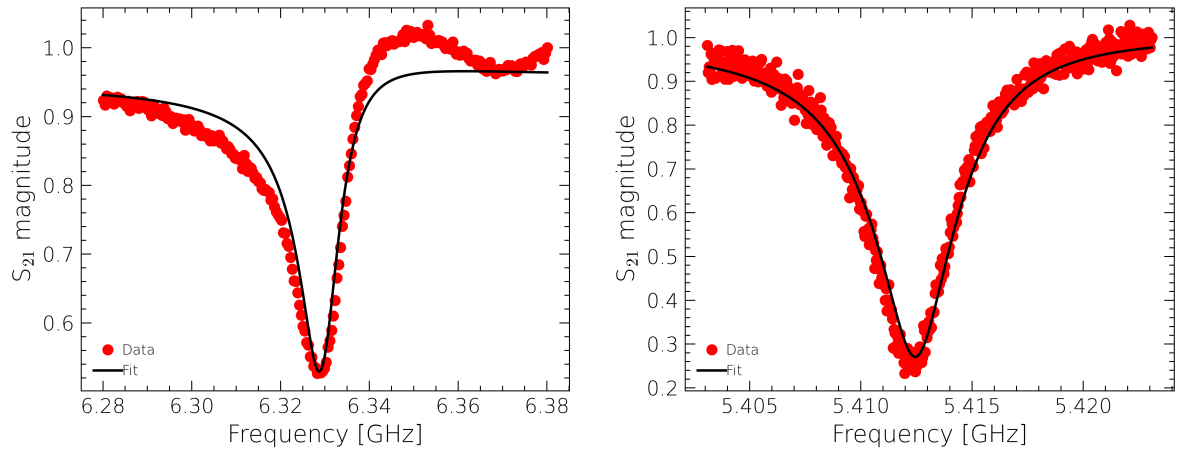

(a) (b)

Figure 7.6: Resonator S_{21} as a function of frequency of (a) sample A at 0 flux and (b) sample B at 0.323 quantum of flux.

Sample	C_C [fF]	C_R [fF]	L_R [nH]	L_k=L_R-L_{geo} [nH]	R [Ω]	X_E [Ω]
A	10.07	105.25	5.48	4.31	0.32	-15.46
B	10.59	105.25	7.46	6.29	0.0945	-4.01
C	9.83	93.24	7.76	6.59	0.0752	-13.91
D	10.6	105.25	5.09	3.92	0.1342	6.39
E	10.36	93.24	5.06	3.9	0.0842	-2.04
B*	10.59	105.25	9.88	8.71	0.725	-10.83
C*	9.83	93.24	10.04	8.88	0.8322	-9.32

Table 7.1: Table summarizing resonator parameters

the loss in the resonator increases by about a decade. In addition, aging increases junction inductance by ∼36%. And finally most of the asymmetry in the resonance is due additional capacitive effect as shown by the X_E column.

7.2.3 Qubit spectroscopy

The qubit spectroscopy obtained by χ shift of the resonator as a function of flux sweep is shown in Figure 7.7. The green colors represent the qubit transition frequency which changes with flux.

The qubits reach minimum frequency at half integer flux. This transition frequency is given by the phase slip amplitude E_{PS} of the small junction. Hence, as phase slip rate reduces in the small junction, so does the frequency at half integer flux.

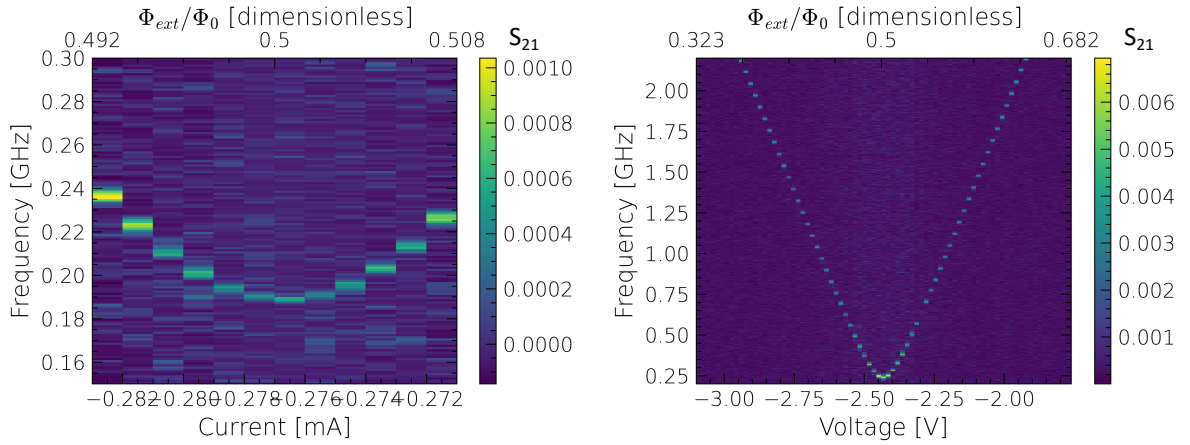

(a) (b)

Figure 7.7: Spectroscopy of qubit as a function of flux of (a) sample A and (b) sample B.

7.2.4 Energy spectrum

The spectrum data is then fit with eigenvalues of the qubit as a function of flux. This gives the quantities: E_C, E_J, E_L, f_r and g_0 which is the coupling strength. The eigen values for the fit are calculated using equation 5.19.

The data is shown in red dots and the fit is shown in the black dashed lines in Figure 7.8. Figures 7.8a and 7.8b are the full transition spectrum of sample A and B, one of the anticrossing of sample A is shown in Figure 7.8c.

Sample	E_J [GHz]	E_C [GHz]	E_L [GHz]	f_r [GHz]	g_0 [MHz]	$f_{ge}(0.5\Phi_0)$ [MHz]
A	10.11	2.19	0.48	6.328	80	189
B	8.53	2.12	0.44	5.412	78	247
C	11.29	2.15	0.44	5.627	70	131
D	6.55	2.9	0.56	6.554	84	911
E	8.72	2.86	0.54	6.948	99	529
B*	5.53	2.38	0.28	4.714	80	562
C*	7.44	2.37	0.28	4.949	92	349

Table 7.2: Table summarizing qubit parameters

The table 7.2 shows the parameters of the qubit obtained from the fitting along with, f_{ge} at sweet spot. Firstly, the minimum transition frequency depends on E_J and E_C and the slope of the transition frequency depends on the inductance E_L. One can intuitively give an analytical formula for the transition frequency as:

$$f_{ge} = \sqrt{E_{PS}^2 + (E_L(2\pi)^2(\Phi_{ext}/\Phi_0 - 1/2))^2} \tag{7.2}$$

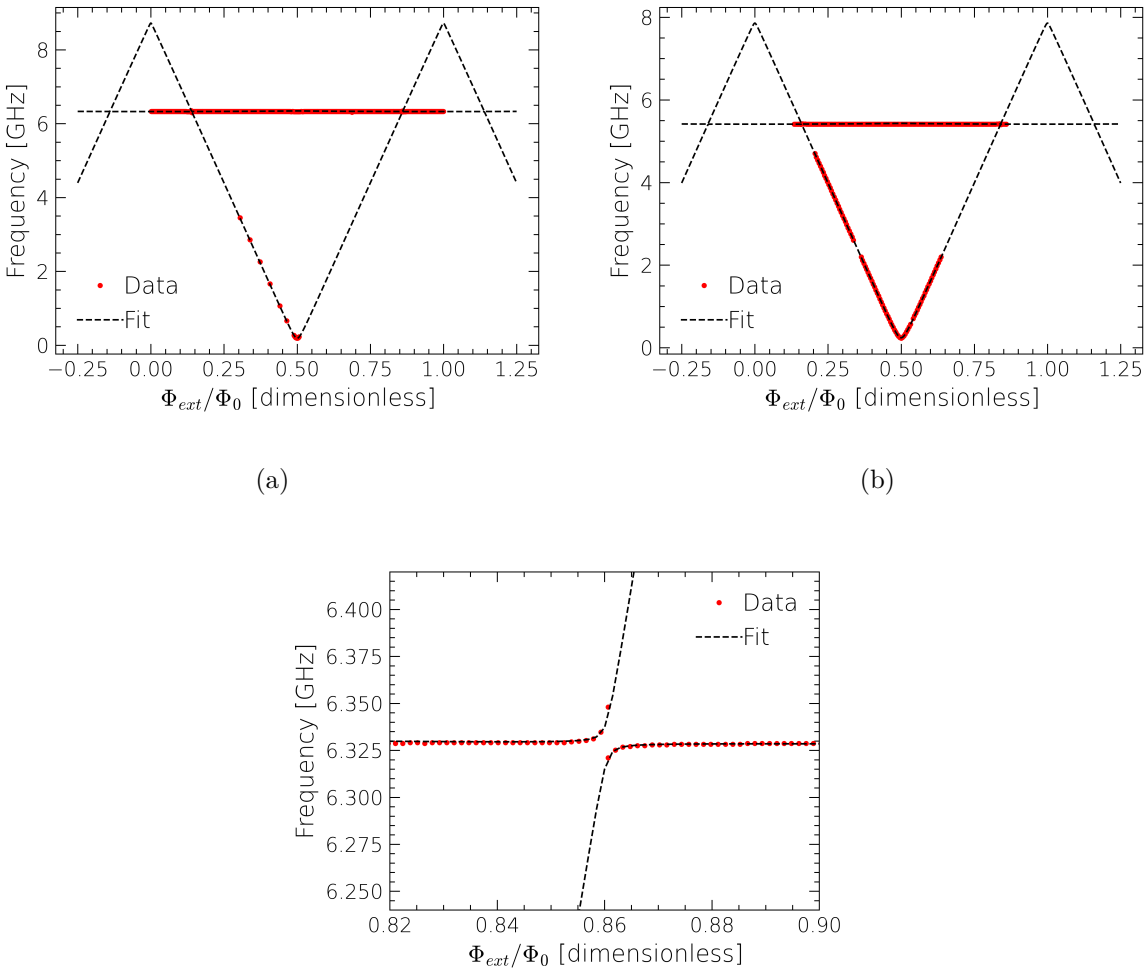

Figure 7.8: Transition frequency as a function of reduced flux between -0.25 and 1.25 of (a) sample A and (b) sample B. (c) Anticrossing between the qubit and resonator as a function of reduced flux of sample A

Secondly, the aging reduces the inductance energy and Josephson energy by ∼36%. Thirdly, the coupling strength between the qubit and the resonator is proportional to $E_M\varphi_0/2\sqrt{2}$ from Equation 5.21 with a predicted value of 130MHz and the measured value of about 85MHz.

7.3 Time domain measurements

Since the transition frequency as a function of external flux is determined, the relaxation and decoherence time of the qubit can be extracted. This is achieved by doing time domain measurements. In the upcoming sections, the Rabi, T_1, T_2^*, T_{2echo} measurements and their protocols are discussed.

7.3.1 Interaction Hamiltonian

In this section, the qubit dynamics in presence of external drive is described. In the rotating frame picture the qubit evolution can be described by the interaction Hamiltonian:

$$H = \frac{hf_\Delta}{2}\sigma_z + \frac{\hbar\Omega}{2}\sigma_x \tag{7.3}$$

where σ_x and σ_z are the Pauli matrices and Ω is the coupling between the qubit and the external field. Ω is proportional to the drive signal amplitude and

$$f_\Delta = \mathrm{f}_{ge} - f_d \tag{7.4}$$

where f_d is the drive frequency and f_Δ is the detuned frequency. When a Pauli matrix is exponentiated, the resulting matrix is called the rotation matrix since it performs rotation operations on the Bloch sphere. The rotation operations by angle θ about z-axis and y-axis of Bloch sphere are given respectively by:

$$\begin{aligned} R_z(\theta) = e^{-i\theta\sigma_z/2} &= \begin{bmatrix} e^{-i\theta/2} & 0 \\ 0 & e^{i\theta/2} \end{bmatrix} \\ R_y(\theta) = e^{-i\theta\sigma_y/2} &= \begin{bmatrix} cos(\theta/2) & -sin(\theta/2) \\ sin(\theta/2) & cos(\theta/2) \end{bmatrix} \end{aligned} \tag{7.5}$$

Therefore the above Hamiltonian in exponential form can be written as:

$$e^{iHt/\hbar} = \begin{bmatrix} e^{-i\pi f_\Delta t} & 0 \\ 0 & e^{i\pi f_\Delta t} \end{bmatrix} \begin{bmatrix} cos(\Omega t/2) & -sin(\Omega t/2) \\ sin(\Omega t/2) & cos(\Omega t/2) \end{bmatrix} \tag{7.6}$$

Any time dependent evolution of the qubit states by the above Hamiltonian can hence be represented in Bloch sphere by rotation of state vector.

7.3.2 Rabi measurement

I.I. Rabi in 1937 formulated the driven evolution of a magnetic moment by a gyrating magnetic field [102]. The same concept is now used in driven evolution of qubits. In Fluxonium the drive signal generates a current flow in the Fluxonium loop inducing the transition of the qubit state. The rate of transition of states is governed by the strength of the drive signal (i.e. current in the loop) [103]. The protocol for the Rabi measurement is given below:

- Qubit is ideally initialized to $|g\rangle$. In this work, the initialization is achieved just by keeping the sample at its base temperatures (25mK or 13mK). Population of the excited state due to thermal photons is finite. The ratio of occupation due to

thermal excitation is given as:

$$\frac{P(|e\rangle)}{P(|g\rangle)} = e^{-hf_{ge}/k_BT} \tag{7.7}$$

where $P(|g\rangle)$ and $P(|e\rangle)$ are the probability of occupation of the ground and the excited state. In this work, the average occupation ratio is 0.45 which means 45% of the time the state is in excited state. This reduces the contrast of the measurement. However, only loss mechanisms are studied in this work hence the initialization to the ground state is not important. But for quantum computation, this may become an issue which needs to be solved with lower base temperatures or a smart initialization mechanism.

- Drive signal pulse of duration τ with zero detuning frequency is applied to the qubit. The state hence evolves unitarily as:

$$e^{iHt/\hbar}|g\rangle = |\psi\rangle = \begin{bmatrix} cos(\Omega\tau/2) & -sin(\Omega\tau/2) \\ sin(\Omega\tau/2) & cos(\Omega\tau/2) \end{bmatrix} \begin{bmatrix} 1 \\ 0 \end{bmatrix} = cos(\Omega\tau/2)|g\rangle + sin(\Omega\tau/2)|e\rangle \tag{7.8}$$

- After the drive signal pulse, the qubit state is measured using the resonator. The pulse duration of the resonator readout signal is chosen to be long enough to get an integrable signal which can differentiate the ground and excited state of the qubit. In this work an integration time of 4μs is taken for the readout of the resonator signal. The probability of occupation of the excited state is hence given by:

$$|\langle e|\psi\rangle|^2 = sin^2(\Omega\tau/2) \tag{7.9}$$

Therefore the probability of occupation of states oscillates with time. The frequency of oscillation Ω is called the Rabi frequency which depends on the strength of the external field. The measurements are averaged over a few tens of thousands of times since the ratio of occupation is large.

The representation of the measurement protocol is shown in the Figure 7.9a. The waveforms in the schematic show the varying width of the qubit drive signal and the pink pulse is the resonator readout pulse. Rabi oscillation averages out exponentially with time due to dephasing about y-axis of the Bloch sphere shown in Figure 7.9b, and the time taken for this dephasing phenomenon is called the T_{2rabi}.

The measurement of Rabi oscillation of sample D at sweet spot is given in Figure 7.10 by blue solid lines. The fit of the Rabi oscillation to the data yields the red solid line. The period of oscillation in this case is 98.8ns leading to a π pulse i.e. width of the pulse to excite the qubit from ground to excited state of 49.4ns. The decay of Rabi oscillation gives $T_{2rabi} = 8.3\mu s$.

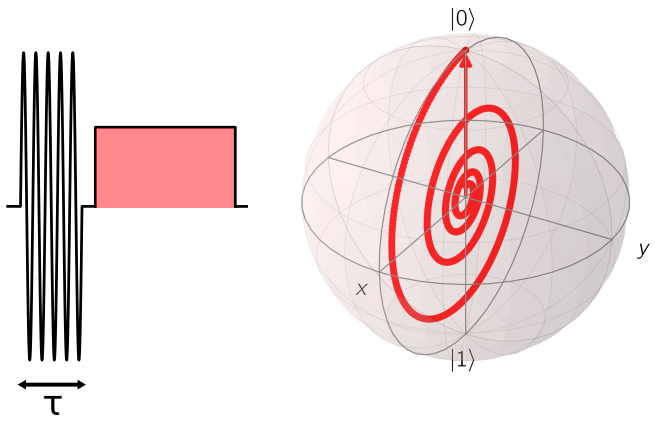

(a) (b)

Figure 7.9: (a) Representation of Rabi measurement where τ is a variable and (b) Bloch sphere representation with state vector evolving due to drive signal.

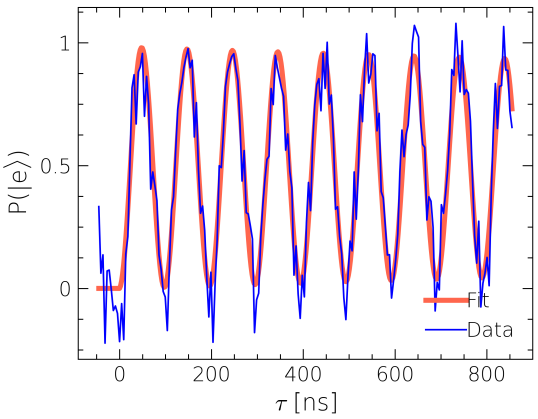

Figure 7.10: Rabi measurement with probability of occupation of excited state as a function of pulse duration τ of sample D at sweet spot with frequency f_{ge}= 911MHz.

7.3.3 Relaxation measurement

The π pulse is applied to the qubit and the qubit is measured after a variable waiting time τ by a resonator readout pulse as represented in Figure 7.11a. The Bloch sphere shows an ideal case of exciting the qubit from $|g\rangle$ to $|e\rangle$ state with a π pulse in Figure 7.11b.

In Figure 7.12, the measured values of probability of occupation of excited state for a T_1 measurement is shown. The relaxation of the qubit from its excited state to the ground state happens with an exponentially decay given by the relaxation time T_1. The data is fit with an exponentially decaying function given in red color which gives a T_1 of $20\mu s$. It is the time taken for the qubit to reach 36% of its initial excited population.

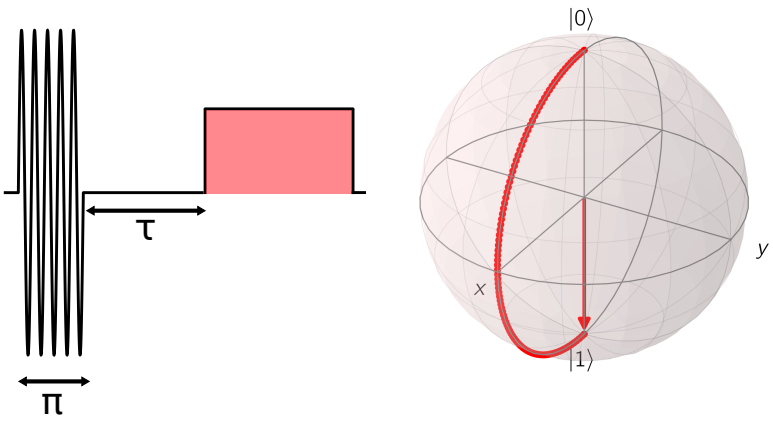

(a) (b)

Figure 7.11: (a) Representation of relaxation measurement protocol with varying time τ between π pulse and resonator readout and (b) Bloch sphere with state vector evolving due to π pulse drive signal.

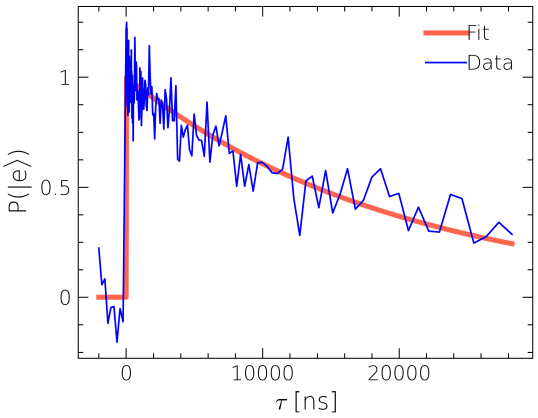

Figure 7.12: T_1 measurement with probability of occupation of excited state as a function of waiting time τ of sample D at sweet spot with frequency f_{ge}= 911MHz.

7.3.4 Ramsey measurement

In Ramsey measurement, the free evolution of the qubit state is observed due to the detuning [104]. The protocol for such measurement is given below:

- The qubit is prepared in the superposed state by applying a $\pi/2$ pulse with a detuned drive signal where the state evolves with time. The evolution of the state

over time τ is defined as:

$$\begin{aligned} \psi(\tau) &= e^{iHt/\hbar}|g\rangle \\ &= \begin{bmatrix} e^{-i\pi f_\Delta \tau} & 0 \\ 0 & e^{i\pi f_\Delta \tau} \end{bmatrix} \begin{bmatrix} cos(\pi/4) & -sin(\pi/4) \\ sin(\pi/4) & cos(\pi/4) \end{bmatrix} \begin{bmatrix} 1 \\ 0 \end{bmatrix} \\ &= \frac{1}{\sqrt{2}}(e^{-i\pi f_\Delta \tau}|g\rangle + e^{i\pi f_\Delta \tau}|e\rangle) \end{aligned} \tag{7.10}$$

- After the waiting time τ, another $\pi/2$ pulse is applied to the qubit to obtain the new state:

$$\psi'(\tau) = -isin(\pi f_\Delta \tau)|g\rangle + cos(\pi f_\Delta \tau)|e\rangle \tag{7.11}$$

- The probability of occupation of excited state is hence given by:

$$|\langle e|\psi'\rangle|^2 = cos^2(\pi f_\Delta \tau) \tag{7.12}$$

Therefore the occupation probability oscillates with time with the detuned frequency f_Δ. The measurement schematic is shown in Figure 7.13a. τ is the waiting time between the two $\pi/2$ pulses. In the Figure 7.13b, the states evolution by a drive is represented by red dots. The blue dots represent the free evolution of qubit during the time τ. The state

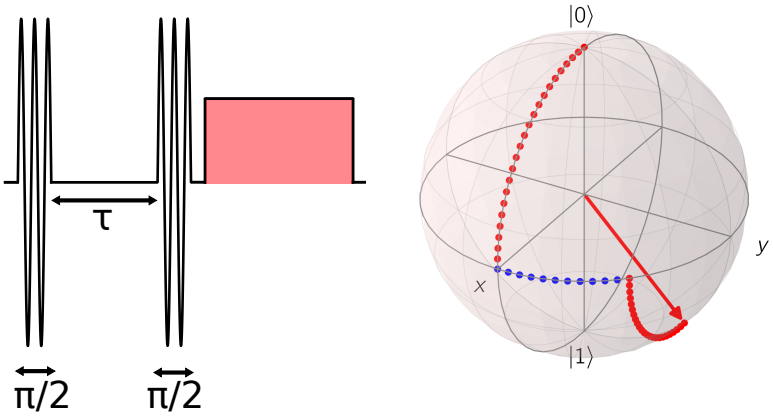

(a) (b)

Figure 7.13: (a) Representation of Ramsey measurement protocol and (b) Bloch sphere representation of state vector evolution due to free evolution given by blue color and driven evolution given by red color.

occupation oscillates between excited and ground state with increasing τ. But due to dephasing induced by fluctuation of the qubit levels, the Ramsey fringes decay into a statistical mixture of states.

In Figure 7.14, the data and the fit of the Ramsey fringes are shown in blue and red color. The T_2^* or the decoherence time in this case is 2.9μs. The detuning frequency is set

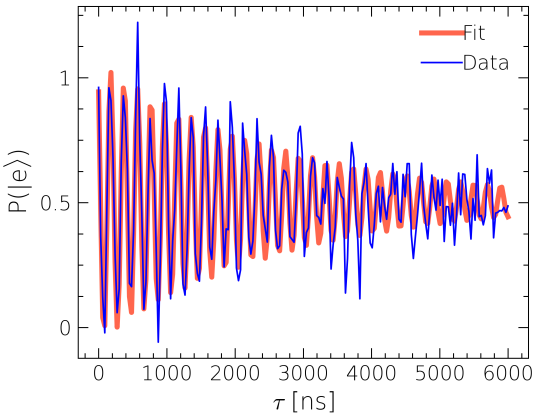

Figure 7.14: Probability of excitation as a function of waiting time τ of sample D at sweet spot with frequency f_{ge}= 911MHz.

to be 5MHz and the fit gives the frequency of 5.06MHz which is close to the set value. Therefore Ramsey measurements give accurate result of the qubit frequency compared to spectroscopic measurements.

7.3.5 Spin echo measurement

Spin echo also known as Hahn echo is a measurement where the dephasing of qubit due to low frequency noise is compensated. The protocol is as follows:

- The qubit is prepared in the superposed state with equiprobable distribution of the states, without any detuning. Due to stochastic shift in the energy of the qubit coming from low frequency noise δf_{ge}, the qubit states gain phase with time and the state is given by:

$$\psi(\tau) = \frac{1}{\sqrt{2}}(e^{-i\pi\delta f_{ge}\tau}|g\rangle + e^{i\pi\delta f_{ge}\tau}|e\rangle) \tag{7.13}$$

- After the waiting time τ, a π pulse is applied to the qubit to inverse the phase accumulation of the states. This causes the refocusing of the dephasing state. Hence the state changes to

$$\psi'(\tau) = \frac{1}{\sqrt{2}}(-e^{i\pi\delta f_{ge}\tau}|g\rangle + e^{-i\pi\delta f_{ge}\tau}|e\rangle) \tag{7.14}$$

- Again the qubit is evolving freely in time τ with opposite phase such that the dephasing is cancelled out. The state hence changes to:

$$\psi = \frac{1}{\sqrt{2}}(-|g\rangle + |e\rangle) \tag{7.15}$$

- A $\pi/2$ pulse is applied to get the state back to its ground state such that:

$$|\langle g|\psi\rangle|^2 = 1 \tag{7.16}$$

This protocol was first showed by Hahn in 1950 [105]. The measurement schematic is

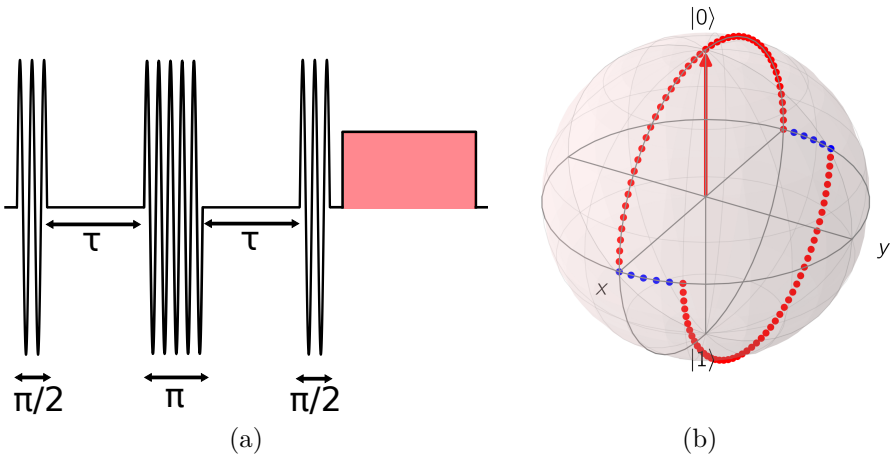

(a) (b)

Figure 7.15: (a) Representation of Spin echo measurement protocol and (b) Bloch sphere representation of state vector evolution due to free evolution given by blue color and driven evolution given by red color.

shown in Figure 7.15a. τ is the waiting time between the $\pi/2$ and π pulses. As shown in the Figure 7.15b the Bloch sphere evolution of state due to drive signal is given by red color and evolution due to low frequency noise is given in blue color.

The protocol is immune to low frequencies noises as the π pulse acts as a high pass

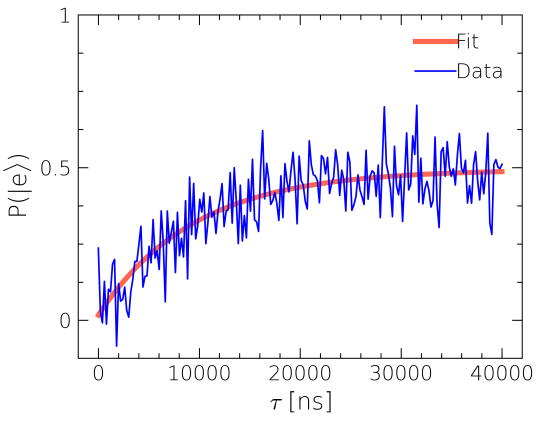

Figure 7.16: Probability of occupation of excited state as a function of waiting time τ of sample D at sweet spot with frequency f_{ge}= 911MHz.

filter. Any fluctuation occurring in time slower than the measurement time is removed due to refocusing of the qubit state. Due to high frequency noise, the dephasing still occurs

but at a different time scale T_{2echo}. This has extensively been used in quantum sensing applications to achieve high T_{2echo} times in the order of milliseconds to seconds [2][106]. The data and fit for spin echo measurement is shown in Figure 7.16 in blue and red color respectively. The echo measurement with single π pulse gives a dephasing time of 9.46μs.

7.3.6 Time domain measurement summary

The measurements are carried out at different flux points. The details of the measurements at sweet spot of the qubit are given in Table 7.3 for all the samples. The analysis on the

Sample	T_1 [μs]	T_2^* [μs]	T_{2echo} [μs]
A	10.1	1.08±0.1	1.03±0.2
B	48.8	4.68±0.6	15.07±7.0
C	53	5.02±0.8	12.3±2.8
D	19.9	2.89	9.46
E	20.2	2.35	10.13
B*	10.3	0.18±0.03	0.18
C*	14.3	0.32±0.04	0.37

Table 7.3: Table showing relaxation time T_1 and decoherence times T_2^* and T_{2echo} at respective sweet spots.

measured T_1 and T_2^* are carried out in the next sections after explanation on sources of loss.

7.4 Dissipation calculation

With the measurements completed, the sources of the dissipation due to fluctuations is discussed. In this section, dissipation in the Fluxonium qubit is described. The coupling of the qubit to the environment can be seen as a variation in phase across the main small junction of the qubit because of a noise current source. The coupling Hamiltonian between the qubit and the environment is hence:

$$H_{cenv} = \Phi_0 \hat{\varphi} I_{noise} \tag{7.17}$$

This coupling dictates the transition rates between the qubit states. The transition rates is given by Fermi's Golden rule as:

$$\begin{aligned} \Gamma_{e\to g} &= \frac{1}{\hbar^2}|\langle e|H_{cenv}|g\rangle|^2 = \frac{1}{(2e)^2}|\langle e|\hat{\varphi}|g\rangle|^2 S_{noise}(\omega_{eg}) \\ \Gamma_{g\to e} &= \frac{1}{\hbar^2}|\langle g|H_{cenv}|e\rangle|^2 = \frac{1}{(2e)^2}|\langle g|\hat{\varphi}|e\rangle|^2 S_{noise}(\omega_{ge}) \end{aligned} \tag{7.18}$$

where Γ is the transition rate, S_{noise} is the noise spectral density. The total noise spectrum density is the sum of the two densities i.e. $S_{noise}(\omega_{ge}) + S_{noise}(-\omega_{eg})$. The relaxation time T_1 is hence given by:

$$T_1 = 1/(\Gamma_{e\to g} + \Gamma_{g\to e}) \tag{7.19}$$

T_1 hence depends on the transition matrix element $\langle e|H_{cenv}|g\rangle$ and on the noise spectrum S_{noise}.

7.4.1 Matrix element dependence

To understand the dependence of transition matrix element, two different scenarios are considered. The two scenarios are named (a) and (b) where inductance energy E_L is 2GHz in scenario (a) and 0.5GHz in scenario (b). In both cases, Josephson energy E_J and capacitive energy E_C is chosen to be 10GHz and 2GHz respectively. The wavefunctions and potential for an external flux of $0.45\Phi_0$ is shown in the Figure 7.17 for both scenarios.

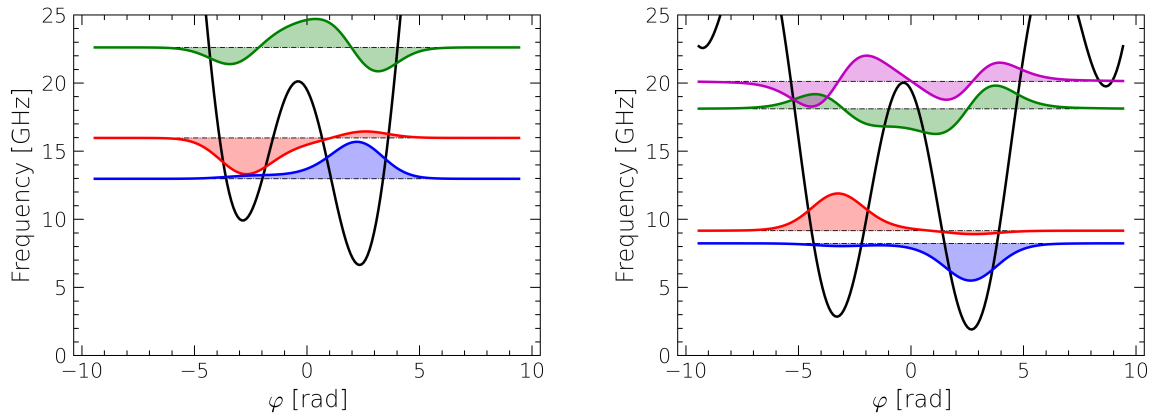

(a) (b)

Figure 7.17: Potential with energy levels and wavefunctions as a function of phase for $E_J = 10GHz$, $E_C = 2GHz$ and (a) $E_L = 2GHz$ and (b)$E_L = 0.5GHz$.

The black solid lines are the potential of the Fluxonium qubit and the blue, red, green and purple colored shaded regions are the wavefunctions of ground, first, second and third excited state respectively. Large overlap of wavefunctions increases the relaxation rates. The matrix element value which defines the extent of overlap is calculated for these examples to be 0.331 and 0.228 for scenario (a) and (b) respectively. This implies 31% decrease in transition rate or 31% increase in T_1 by just decreasing the E_L from 2GHz to 0.5GHz. And further increase in T_1 is possible when E_J/E_C ratio is increased.

7.4.2 Impedance dependence: Lumped element circuit

The spectral density depends on the real part of the admittance of the qubit circuit given by the relation:

$$S_{noise}(\omega_{eg}) = \hbar\omega_{eg} Re[Y_{env}(\omega_{eg})](coth(\hbar\omega_{eg}/2k_BT) + 1) \tag{7.20}$$

where $Y_{env}(\omega_{eg})$ is the admittance of the circuit and T is the operating temperature. The lumped element circuit is shown in Figure 7.18. The different parts of the circuit is color coded to the optical and false color SEM image of Figure 6.7.

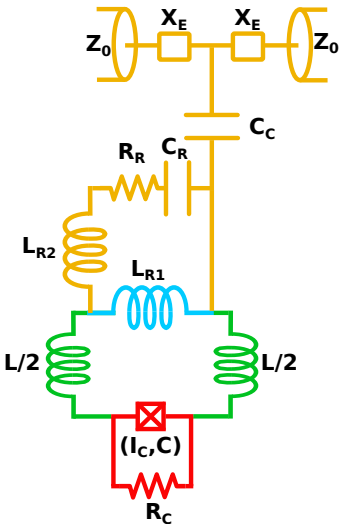

Figure 7.18: The circuit of Fluxonium with resonator modelled from spectroscopy measurement and resistance due to junction capacitance.

- **Purcell effect:** The readout resonator part which couples to the transmission line induces Purcell effect [107] on the qubit at resonant conditions. The admittance responsible for Purcell effect is calculated to be:

$$Y_P(\omega)^{-1} = \left[j\omega(L_{R1} + L_{R2}) || \left(R_R + \frac{1}{j\omega C_R} \right) \right] || \left(\frac{1}{j\omega C_C} + \frac{Z_0 + X_E}{2} \right) \tag{7.21}$$

  The values of circuit elements are obtained from the resonator spectroscopy fitting discussed in section 7.2.2. Further details about the impedance is given in section 7.4.4.

- **Capacitive loss:** The resistance in the small junction R_C is mainly attributed to the dielectric loss. The junction oxide and the surface of the electrodes is made out of dielectric material which is lossy. The loss in such dielectrics are given by $tan\delta = \epsilon''/\epsilon'$ where ϵ' and ϵ'' are the real and imaginary part of the relative permittivity of the dielectric.

The lossy material contributes to the relaxation of the qubit. The loss is given by the inverse of the quality factor of the capacitance such that:

$$Q_C = Im[Y_C(\omega)]/Re[Y_C(\omega)] = 1/tan\delta$$
$$\text{where } Y_C(\omega) = j\omega C + (1/R_C) \tag{7.22}$$

where C is the capacitance of the small junction obtained by the qubit spectrum and R_C is the fitting parameter of the capacitance loss.

7.4.3 Impedance dependence: Propagating mode

The previous circuit description used lumped element model for the inductors. But in the measurements an unexpected drop of T_1 was observed away from the sweet spot which will be discussed in the next section. In order to study this effect an accurate description was examined. The accurate description involves considering the chain of Josesphson junctions since the chain can have propagating modes and compromise additional dissipative channels. Therefore the real circuit as shown in Figure 7.19 is considered for the calculation of the relaxation time.

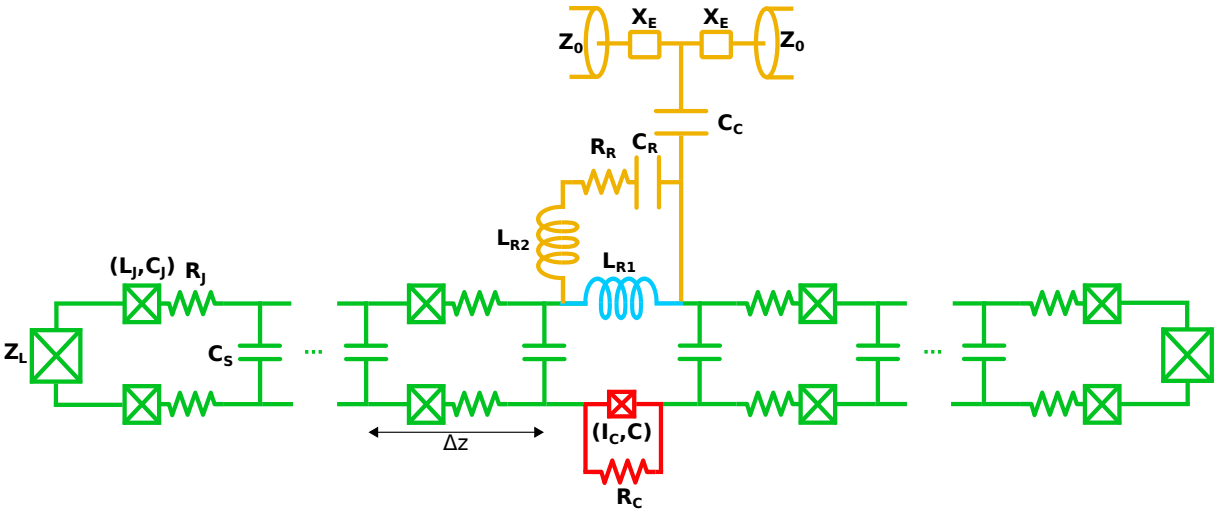

Figure 7.19: The real circuit of Fluxonium with resistances used for noise spectral density calculation.

- **Chain loss and chain mode:** The chain of JJs is described by series of the junction inductance L_J which is parallel with the junction capacitance C_J. The upper and lower arms of the chain in the rectangular loop of the qubit consists of junctions such that a repetitive structure with length Δz can be defined. The SEM image of the chains is explicitly shown in Figure 7.20a. The green region highlights the smallest group of repeatable units of JJs to form a chain.
  The unit cell in the chain consists of one junction on each arm of the chain. Since the junctions on each arms are close to one another, a capacitance between the two

arms can be considered. C_S is the capacitance per unit length between the two arms of the chain which can lead to chain modes in the circuit.
The capacitance between the two arms can be analytically calculated as a Coplanar strips whose complete treatment is given in reference [108]. The capacitance is given by:

$$C_S = \epsilon_0(1+\epsilon_r)\frac{log[2(1+\sqrt{k})/(1-\sqrt{k})]}{\pi}$$
$$\text{where } k = \sqrt{1-\left(\frac{S}{S+2W}\right)^2} \tag{7.23}$$

where S is the distance between the two sides of the chains. In this work it is 1.54μm and W is the width of the arms is 5.2μm. For the above values with dielectric being the Silicon substrate, capacitance per unit length between the two arms of the chain is about 250pF/m. The actual value obtained from the measurement will be shown in the section 7.4.4.

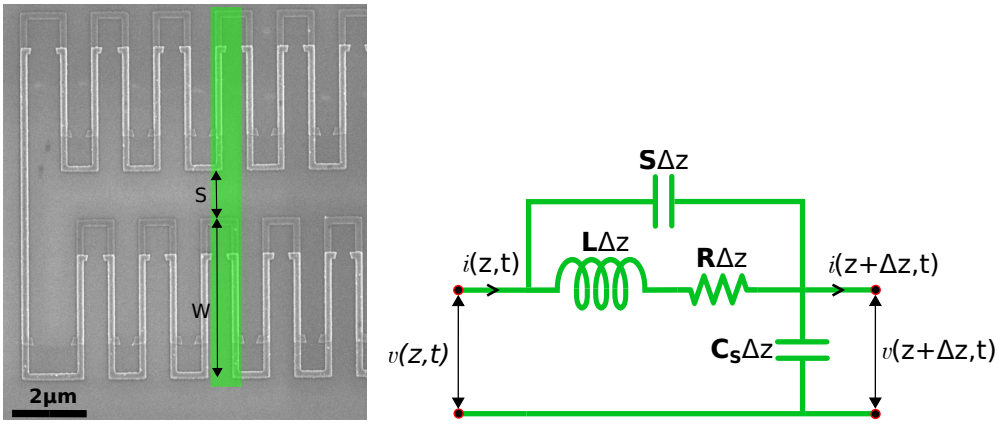

(a) (b)

Figure 7.20: (a) SEM image of the chain with highlight of a unitcell and (b) The model of unit cell.

Since one junction in each arm has same net effect as two junctions on one arm of the chain, the unit cell can be modelled with linear circuit elements as shown in Figure 7.20b where $S_c\Delta z = 2S_J$ is the elastance or the inverse of capacitance of the junction, $L\Delta z = 2L_J$ is the junction inductance and $R\Delta z = 2R_J$ is the resistive element. R_J incorporates both the dielectric loss in the chain of JJs and the quasiparticle loss in the chain.
With all the given parameters, the impedance of such chain can be solved by using transmission line formalism where the impedance observed by the small junction

will be:

$$Z_{in} = Z_0\left[\frac{(Z_L + Z_0)e^{l\gamma} + (Z_L - Z_0)e^{-l\gamma}}{(Z_L + Z_0)e^{l\gamma} - (Z_L - Z_0)e^{-l\gamma}}\right]$$
$$\text{where } Z_0 = \frac{1}{\sqrt{[\frac{j\omega}{S} + \frac{1}{R+j\omega L}]j\omega C_S}} \text{ and } \gamma = \sqrt{\frac{j\omega C_S}{[\frac{j\omega}{S} + \frac{1}{R+j\omega L}]}} \tag{7.24}$$

Z_L is the load impedance which is the long junction impedance at the end of the chain shown in the SEM in Figure 7.20a and l is the length of the chain.
Since, Z_L is very small, if one assume it to be 0Ω, the chain of junctions would be terminated by a short circuit and the chain acts as a $\lambda/4$ transmission line. The resonant modes of the chain could then affect the T_1.

Therefore, the total impedance of the circuit observed by the small junction due to resonator and the chains on two sides of the small junction is:

$$Z(\omega) = 2Z_{in} + 1/Y_P(\omega) \tag{7.25}$$

The real part of the admittance i.e. $Re[1/Z(\omega)]$ contributes to the relaxation time.

7.4.4 Quasiparticle dependence

The quasiparticles tunneling through the small junction also induces relaxation of the qubit. Normalized density of quasiparticle i.e. ratio of quasiparticles to Cooper pairs, in thermal equilibrium is given by $x_{eq} = \sqrt{2\pi k_B T/\Delta}e^{-\Delta/k_B T}$. The transition rate due to the quasiparticles is given by [109]:

$$\Gamma = |\langle 1|sin(\hat{\varphi}/2)|0\rangle|^2 S_{qp}(\omega_{10})$$
$$\text{where } S_{qp}(\omega_{10}) = 2\hbar\omega_{10} Re[Y_{qp}(\omega_{10})]/e^2 \tag{7.26}$$

The real part the of admittance $Y_{qp}(\omega_{10})$ is calculated to be [110]:

$$Re[Y_{qp}(\omega_{10})] = \frac{4x_{eq}E_J e^2}{\Delta h}\left(\frac{2\Delta}{\hbar\omega}\right)^{3/2} \tag{7.27}$$

The quasiparticle at the sweet spot plummets due to equal circulation of clockwise and counterclockwise current. Away from the sweet spot however, there is a phase difference between the electrodes of the junction resulting in finite quasiparticle tunneling.

7.4.5 Relaxation analysis

The qubit frequency and its transition matrix element changes with flux. Hence data for relaxation is taken at different flux points. For the sake of statistics T_1 is measured at each point for some number of times. The number of repetitions of measurements is not constant owing to long time required for these relaxation measurements.
The measured relaxation time is plotted as a function of reduced external flux for sample A in Figure 7.21a. The blue dots with error bars are the values of T_1 which is fitted optimally with total relaxation times given by black dashed lines. It is the sum of relaxation times due to quasiparticles and capacitive loss in small junction given by red and blue dashed lines and Purcell and chain loss given by green dashed lines.
As it can be seen, at the sweet spot, the T_1 reaches a minimum. This indicated the limiting factor for relaxation is not quasiparticles in the small junction. In this case, the limiting factor is the loss in the small junction capacitance and in chain which could be due to quasiparticles or dielectrics as shown in the figure.
Away from the sweet spot both quasiparticles and junction capacitance loss are dominating factors in reducing T_1. Further away from the sweet spot close to $0.2\Phi_0$, the T_1 drops significantly. This is due to the impedance of the chain dropping to zero which causes small junction to couple to the environment. The imaginary part of the impedance of the chains and resonator is shown in Figure 7.21b as a function of frequency and external flux.

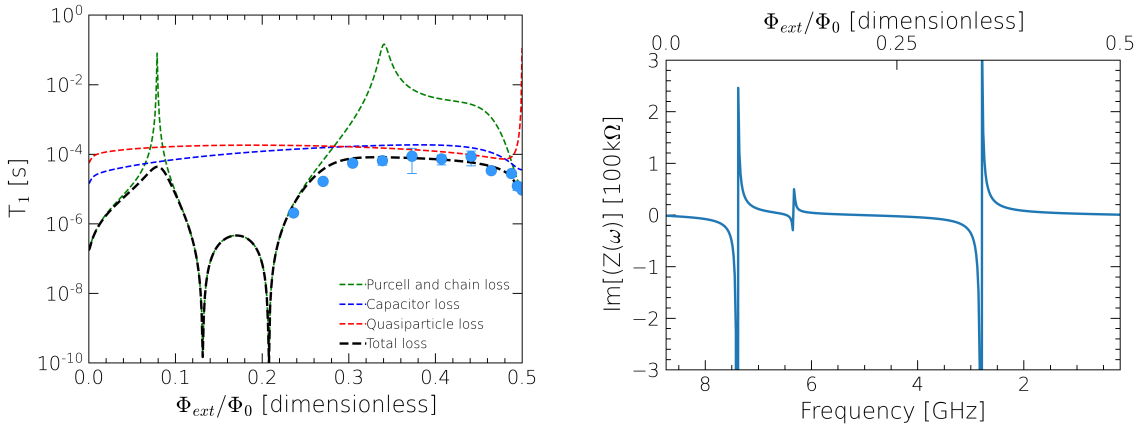

(a) (b)

Figure 7.21: (a) T_1 as a function of reduced external flux and (b) Imaginary part of impedance observed by the small junction as a function of reduced external flux and frequency.

The detailed explanation is as follows:
Close to the sweet spot the chain acts as inductor but as transition frequency increases away from the sweet spot, the qubit frequency approaches first mode of the chain. At the

first chain mode, the impedance of the chain increases significantly and the small junction does not observe the environment. This causes T_1 due to chain loss to significantly increases as shown in green dashed lines. Above this frequency the chain behaves capacitively due to negative impedance. As the qubit transition frequency further increases the chains impedance approaches zero and the small junction is short circuited to the resonator readout causing the T_1 to drop significantly. As the resonator mode and second chain modes are present at higher frequencies the qubit T_1 never recovers.

The data is fit using x_{eq}, Q_C, C_S and R_J as free parameters. The capacitance per unit length, C_S from the fit is found to be 295.1pF/m which is close to the value obtained by considering chains as coplanar striplines i.e. 250pF/m from Equation 7.23. The other parameters extracted from the fit are given in the Table 7.4.

When more data as a function of flux is available an optimum fit can be provided. However, just a few data points are available for several of the samples. With such data, an optimal fit is impossible to accomplish. As a result, the maximum loss from each mechanisms can be determined by eliminating one loss mechanism at a time. This is shown in the table as rows titled without(w/o) chain loss and without(w/o) capacitive loss. Due to lack of data there are no optimal fit possible for B, C, D and E and for sample C, D and E neither minimum nor maximum amount of quasiparticle density can be estimated.

Sample	T_{1ss} [μ s]	Fit	$x_{eq}(\times 10^{-6})$	$tan\delta(\times 10^{-5})$	Chain loss [Ω]
A	10.1	Optimum	3.02	1.05	0.36
		Min. Chain loss	0.45	4.26	0.21
		W/O capacitive loss	3.98	-	0.43
B	48.8	W/O Chain loss	2.04	2.45	-
		W/O capacitive loss	3.47	-	0.32
C	53	W/O Chain loss	-	4.57	-
		W/O capacitive loss	-	-	0.09
D	19.9	W/O Chain loss	-	1.09	-
		W/O capacitive loss	-	-	3.19
E	20.2	W/O Chain loss	-	1.95	-
		W/O capacitive loss	-	-	1.44
B*	10.3	Optimum	4.07	2.24	1.39
		W/O Chain loss	3.89	2.57	-
		W/O capacitive loss	5.25	-	9.26
C*	14.3	Optimum	2.34	2.18	0.79
		W/O Chain loss	2.04	3.01	-
		W/O capacitive loss	3.028	-	2.69

Table 7.4: Table summarizing loss parameters with different limits

Firstly, the average capacitive loss among the samples in this work is about $tan\delta \approx 3 \times 10^{-5}$. This is ten times lossier than current state of the art [77][94][111]. This could be explained by the resist residue remaining on the substrate despite O_2 plasma etching of the resist. It is known as the vile of death [112] in the qubit community since it is a

thin layer of resist that increases decoherence and dissipation in the qubit.
Secondly, the typical value of quasiparticles density in the small junctions is 3×10^{-6} which is two orders of magnitude larger than the current state of the art. This can be attributed to the quality of junctions achieved in the evaporation chamber which was using at this time a large variety of materials.
Thirdly, by comparing the estimations between B and B*, it can be seen that quasiparticle density and loss in the chain in general increases with aging. And the chain loss is lower in the samples which are unaged compared to aged samples. T_1 at sweet spot is longer in samples with smaller chain loss.

7.5 Decoherence due to noise

Dephasing and relaxation can induce decoherence as discussed in the introduction. The decoherence is measured by Ramsey interferometry. In the current work, decoherence is due to dephasing since $2T_1 >> T_2^*$. The fluctuations in qubit energy levels due to noise in the environment causes dephasing.
Generally, there are two sources of the decoherence. First, is the coherent dephasing sources originating from the control systems. These are caused by fluctuating control sequence pulses. Such issues are solved by mixer calibration to avoid any side band interactions or working with setup having less phase drifts etc. Second and important ones are the stochastic noise sources which comes from charge, flux noise which are inherent and random in nature but also thermal noise. This causes a distribution or spreading of energy levels. There are different noise sources for decoherence in superconducting qubits [113].
For the dephasing of the qubit, usually, all frequency components of the noise can contribute. For detailed formalism, consider the change of phase of the qubit as a function of time.

$$\phi(t) = \int_0^t \omega_{ge} dt' = \langle\omega_{ge}\rangle t + \delta\phi(t) \tag{7.28}$$

where $\phi(t)$ is the time dependent phase of the qubit and $\delta\phi(t)$ is the time dependent phase fluctuation. In a rotating frame, the phase evolving at the qubit transition frequency is ignored such that

$$\phi(t) = \delta\phi(t) = \frac{\partial\omega_{ge}}{\partial N} \int_0^t N(t')dt' \tag{7.29}$$

where N is the noise variable and ω_{ge} is dependent on N. The average time evolution function due to fluctuation which has Gaussian distribution is given by:

$$\begin{gathered}\langle e^{i\delta\phi(t)}\rangle = e^{-\langle\delta\phi^2(t)\rangle/2} \\ \text{where } \langle\delta\phi^2(t)\rangle = t^2\left|\frac{\partial\omega_{01}}{\partial N}\right|^2\int_{-\infty}^{\infty} d\omega S_N(\omega)g_N(\omega,t)\end{gathered} \tag{7.30}$$

where $S_N(\omega)$ is the noise spectral density of the noise source N and $g_N(\omega,t)$ is the filter function of the noise spectrum [114] with qubit free evolution time t. For Ramsey and Spin echo measurement, the filter function is given as [115]

$$\begin{aligned} g_N(\omega,t)|_{Ramsey} &= sinc^2(\omega t/2) \\ g_N(\omega,t)|_{Spinecho} &= sin^2(\omega t/4)sinc^2(\omega t/4)\end{aligned} \tag{7.31}$$

The noise spectral density $S_N(\omega)$ is usually dominated by low frequency $1/f$ noise. As frequency increases noise density reduces. The window of the filter function of Ramsey is dominant close to $\omega = 0$ due to sinc function. Whereas in a spin echo measurement, the filter function is 0 when $\omega = 0$ due to sine function. The function becomes dominant when $\omega = 2\pi/t$. Therefore, the contribution of $1/f$ noise is large in Ramsey compared to spin echo. Hence, the T_2^* is smaller compared to T_{2echo}. When number of evenly spaced π pulses applied increases, the filter function frequency window moves to higher frequencies where noise density is lower. This cause the decoherence to reduce further. In literature this is called a Carr-Purcell-Meiboom-Gill (CPMG) sequence [116][117].
In general there are four main noise sources in superconducting qubits namely, charge noise, flux noise, critical current noise and readout photon noise. For large waiting time t, the sinc function in Equation 7.31 can be considered as a delta function and the decoherence time is given as [24]:

$$T_2^* \simeq \frac{1}{A}\left|\frac{\partial\omega_{ge}}{\partial N}\right|^{-1} \text{ where } A = \sqrt{S_N(\omega)|\omega|/2\pi} \tag{7.32}$$

- **Charge noise($N = n_g$):** Charge noise arises from fluctuations of charge leading to fluctuations in the local electric field close to the small junction. For Fluxonium, the low frequency charge noise is negligible due to the presence of large inductance in parallel to the small junction resulting in filtering of any low frequency electric field fluctuations. Since the chains have large E_J/E_C the junctions in the chain are also insensitive to charge noise.

- **Flux noise($N = \Phi_{ext}$):** The magnetic flux noise is an important dephasing mechanism in Fluxonium. Close to the small junction where the phase slip rate is large, any stochastic flipping of spins (magnetic dipoles) on the surfaces of the supercon-

ducting metals or substrate [118][119] or noise from the coil, can change the flux in the Fluxonium loop. At the sweet spot due to the derivative $\frac{\partial \omega_{ge}}{\partial \Phi_{ext}} = 0$, the T_2^* is enhanced. For other flux points, even with a small fluctuations amplitude (A) of the order $10^{-6}\Phi_0$ [120], T_2^* of only few microseconds can be achieved.
The gradient of frequency as a function of flux is calculated using Equation 7.2. The slope hence is directly proportional to square of the inductive energy. Hence large inductance would reduce the slope. Therefore, by decreasing E_L, T_2^* can be increased which is the advantage of Fluxonium qubits. In this work, value of T_2^* at sweetspot is given in Table 7.3 with shows a maximum of $5\mu s$. Away from the sweet spot the values rapidly decreases to about 150 ns.

- **Critical current noise($N = I_C$):** The critical current fluctuation causes fluctuation in junction energy. This causes qubit frequency to change. The junction with large area is more susceptible to current noise [121]. Therefore, the noise is large in the junctions of the chain which fluctuates the inductive energy of the superinductor. This is the another important limiting factor for the coherence time of Fluxonium.

- **Readout photon noise:** The resonator coupled to the qubit is used for measurements after qubit operations are performed. However, there could be fluctuating thermal photons [122] or non-zero mean number of photons from the sources at resonator frequency during the qubit operation. These photon-number fluctuations impact the qubit frequency fluctuation $f_{01} + \chi n$ due to AC stark shift, where n is the photon number and 2χ is the difference in the frequency of resonator between qubit in ground and excited state. The decoherence due to readout photon noise is given by:

$$T_2^* = \left[\frac{\kappa}{2} Re\left[\sqrt{\left(1 + \frac{2i\chi}{\kappa}\right)^2 + \frac{8i\chi n_{th}}{\kappa}} - 1\right]\right]^{-1} \tag{7.33}$$

  where κ is the linewidth of the resonator and n_{th} is the effective thermal photon number in the resonator.

In sample A, T_2^* and T_{2echo} are similar. This signifies the noise source is not $1/f$ dependent. Further study needs to be done to find the source. Samples B and C measured at IBM at 13mK base temperature has larger T_2^* than samples measured in Neel Institute with dilution refrigerator at 25mK base temperature. This could be explained by thermal photons interacting with the resonator and the chain modes increasing readout and chain photon noise.
The aged sample B* and C* have reduced T_2^* and T_{2echo} compared to the unaged samples. This can be attributed to phase slips in the chain of arrays because of quasiparticle induced fluctuation in the junctions of chains due to aging [123]. Therefore, qubits that are aged are not good for coherence of the qubit.

The flux noise amplitude A in all these samples is around $0.25\text{m}\Phi_0$ which is two orders of magnitude larger than the state of the art. One of the reasons could be due to large magnetic noise originating from the fluctuating oxygen molecules and ions on the surface of the substrate and metal [124].

7.6 Summary

From the measurements of seven samples the data on qubit parameters are extracted. The spectroscopy shows the measured values of the qubit parameters are close to the designed values. The increase in inductance of junctions 36% with aging of samples by five months is another revelation from the spectroscopic measurement.
At the sweet spot the maximum T_1 observed is the about $53\mu s$ in sample C and losses dominating at sweet spot is found to be the chain loss and the small junction capacitive loss. Away from the sweet spot the maximum T_1 observed was about $80\mu s$ in sample A and the limiting factors for reduced relaxation is observed to be originating from capacitive and quasiparticle loss in the small junction.
The loss from the chain modes are extracted. The origin of this loss was explained by considering additional capacitance between the two arms of the chain in the rectangular loop causing the chain on each side of the small junction to act as a $\lambda/4$ transmission lines.
The decoherence time rather very low i.e. around $4\mu s$. The limitations for decoherence is originating from few noise mechanisms such as flux noise, resonator and chain mode thermal photon noise and critical current noise. In aged samples the phase slip rate is said to increase causing decoherence. Noise amplitude due to flux noise is found to be $0.25\text{m}\Phi_0$. More detailed study is necessary to quantify the other noise amplitudes.

Chapter 8

Conclusion and perspectives

Conclusion

In this research, I addressed the question on sources of dissipation in superconducting quantum circuits. Low loss superconducting circuits are beneficial for many applications which made the study rather important for different fields.

Resonators are the best devices to study losses. Hence during my PhD I fabricated and measured thirty three distinct superconducting resonators made from Aluminum. Aluminum was the material of choice for the study due to their common usage in quantum circuits. This work focused in particular on understanding the origin of quasiparticle and TLS losses in such superconductors. After studying and developing a theoretical understanding of the effects of quasiparticles in 2D superconducting circuits, it was identified that thermal quasiparticles affect the resonator quality factor above $200mK$.

Since mean free path and loss are directly related in normal state metal it was interesting to study the same effect in superconductors. To study the effect of mean free path, the resonators were fabricated with different thickness, from 50nm to 2700nm, which involved both lift-off and etching methods. It includes fabrication of a thick evaporated film of 550nm using a bilayer resist which is to my knowledge the first time for the resonators. It was confirmed from the measurements that losses due to thermal quasiparticles reduce with increasing mean free path.

At temperatures below $200mK$, other losses dominate the resonator and they are dependent on the number of photons in the resonators. This was characterized by sweeping the power applied to the resonators. From this work, two loss mechanisms depending of photon numbers were identified: TLS loss and AC loss at low and high photon numbers respectively.

To study the effect of losses from TLSs, resonators with different capacitances were used. The results showed that resonator losses reduced as capacitance gap increased. This was interpreted to be due to the reduction of electric field concentration at the substrate air interface as capacitance gap increases. The measurements also showcased the impact of fabrication processes and effect of thick films on the TLS losses. It was seen that the etched samples had large TLS losses. Furthermore, the TLS loss in thick films showed smaller dependence on the capacitance gap compared to thin films due to the reduced electric field concentration on the substrate surface.

A comparative study of ground plane losses using Aluminum and Cooper waveguide

showed that metallic ground planes are lossier than superconducting ground planes. This was observed to be due to finite resistvity of metallic ground planes even at a low temperature of $25mK$.
Even though resonators are best device to study losses, a topologically protected qubit would be less sensitive to losses. The state of the art superconducting qubit during the start of the research project was 3D Fluxonium, which is still true during the writing of this thesis. Hence seven Fluxonium samples were studied in a 2D architecture to quantify the losses in such qubits.
From the modelling of the qubit, it was observed that the larger the inductance in the qubit loop or larger the ratio of Josephson energy to capacitive energy, larger is the relaxation time of the qubit. Therefore, Fluxonium qubit with large inductance was fabricated using a series of Josephson junction.
The dissipation in the qubit was known to originate from the losses in the circuit elements. At the sweet spot of the qubit, the dielectric loss of the small main junction and loss in chain of Josephson junctions were found to be responsible for relaxation. The parameters for dielectric loss and quasiparticle density in this work were one to two orders of magnitude larger than the current state of the art Fluxoniums. The reason was not identified clearly but it could be speculated to be resist residues and chamber environment while evaporation of junction that determines the capacitive and quasiparticle loss respectively. In order to improve the relaxation time further, the capacitive loss needs to be reduced. Two of the seven samples measured were aged for five months. The aged samples show higher quasiparticle and chain loss than unaged samples. More data would be necessary to make a definite conclusion on such comparison.
Another loss channel resulting in relaxation was identified in this work. This was achieved by modelling the qubit with the real circuit as accurately as possible. The additional loss was originating from the chain modes which increase the relaxation process away from the sweetspot.
The fluctuations of energy levels responsible for decoherence in the qubits at sweet spot were also measured in this work. The most likely cause for decoherence at present are speculated to be the thermal photons in the chain mode and the resonators. Away from the sweet spot the main source of noise is the flux noise which depends on the slope of the transition frequency with respect to magnetic flux. And lastly, qubits which aged, show high frequency noise responsible for decoherence which in this case could come from phase slips in the chain. More detailed study is necessary to quantitatively describe the noise in the Fluxonium qubit.

Perspectives

Few ideas that could follow immediately for the resonator study are given below:

- Resonators with simple structures can be studied to obtain the quantitative estimates of the participation ratios with simulation software as a function of thickness

and capacitance gaps. This helps in quantifiable study of TLS loss.

- With this work as a stepping stone, high kinetic inductance materials in the BCS limit can be studied and used in applications such as superinductance and MKIDs.

Few ideas that could follow immediately for the Fluxonium qubit study are given below:

- The future directions of the research on qubit could be to reduce losses further in Fluxonium by using Sapphire substrate to realize the qubit and to improve on the design to avoid chain loss.
- Addition of a fast flux line to the qubit to Floquet engineer the Fluxonium and improve qubit lifetimes [125].
- At the end of the PhD, I have contributed to the improvement of the temperature of the fridge from $25mK$ to $10mK$. Therefore next set of samples measured could show better initialization of qubit in the ground state.

Appendix A

Quality factor of LC resonator

Schematic of LC resonator with losses is shown below: For simplicity, one can drop the

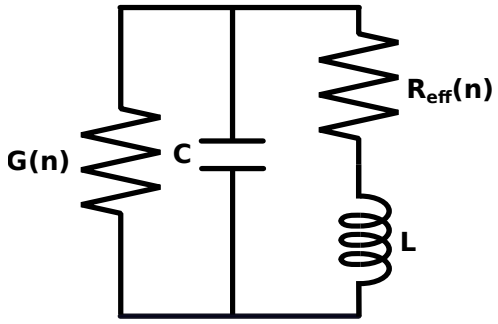

Figure A.1: The LC resonator with losses given by resistance $R_{eff}(n)$ and conductance G(n).

photon dependence and the impedance of the resonator is given as:

$$\begin{gathered} Z = Z_1 \parallel Z_2 \\ \text{where } Z_1 = R_{\text{eff}} + j\omega L \text{ and } Z_2 = \frac{1}{G + j\omega C} \\ \text{Therefore } Z = \frac{R_{\text{eff}} + j\omega L}{1 + (R_{\text{eff}} + j\omega L)(G + j\omega C)} \end{gathered} \tag{A.1}$$

When $Z = 0$ the above equation reduces to

$$1 + (R_{\text{eff}} - j\omega L)(G - j\omega C) = 0 \tag{A.2}$$

By solving the quadratic equation for the ω, the eigen frequency of the resonator is given as:

$$\omega = \pm\sqrt{\frac{1 + \mathrm{R_{eff}G}}{LC} - \left(\frac{\mathrm{G}}{2C} + \frac{\mathrm{R_{eff}}}{2L}\right)^2} + j\left(\frac{\mathrm{G}}{2C} + \frac{\mathrm{R_{eff}}}{2L}\right) \tag{A.3}$$

The quality factor of the resonator is defined as:

$$Q = \frac{Re[\omega]}{2Im[\omega]} \tag{A.4}$$

This results in the quality factor expressed in Equation 2.8.

Appendix B

Data extracted from resonators

Sample	C gap [μm]	f_0 [GHz]	Q_{0TLS}	Q_{other}	β	n_c
A (11nm)	30	4.352	444572	8175504	0.44	1.46
	60	4.632	538494	10643829	0.44	4.01
	90	4.788	592671	8785461	0.40	6.81
	140	4.955	644758	3489176	0.41	3.83
	210	5.099	809755	2493960	0.40	24.87
B (39nm)	30	4.517	434938	54216211	0.46	2.73
	60	4.804	551687	37270803	0.45	17.78
	90	4.962	578797	18984536	0.41	10
	140	5.134	652545	4037923	0.48	23.71
	210	5.290	652548	4758071	0.41	16.94
	300	5.418	819535	2919193	0.52	22.60
C (44nm)	30	4.506	310881	35101613	2872	0.63
	60	4.795	558343	28033081	68.12	0.66
	90	4.954	461153	313270	14.96	0.54
	140	5.134	538556	984342	6.80	0.39
	210	5.287	343502	1579275	769.4	0.45
	300	5.402	312548	616898	1194.6	0.43
D (47nm)	30	4.612	550034	7444576	0.59	865.9
	60	4.865	580161	20363034	0.51	1615
	90	5.039	610354	4019898	0.31	106.9
	140	5.215	501745	2951876	0.34	22.60
	300	5.492	687819	752225	0.27	161.5
E (232nm)	30	4.675	585780	2434853	0.46	34.80
	60	4.992	643289	660294	0.38	43.57
	90	5.154	621076	1497369	0.34	16.46
	140	5.326	771681	1080986	0.29	0.02
	210	5.496	728197	488481	0.27	0.01
	300	5.612	730129	1173328	0.33	24.75
F (536nm)	30	4.661	551920	2854368	0.49	4.33
	60	4.872	468748	2798669	0.46	1.12
	90	5.029	779024	1785244	0.49	12.28
	140	5.154	644188	1919820	0.48	8.10
	300	5.470	773830	608778	0.5	44.48

Table B.1: Table summarizing the parameters from TLS model fitting of quality factor

Bibliography

[1] Morten Kjaergaard, Mollie E. Schwartz, Jochen Braumüller, Philip Krantz, Joel I.-J. Wang, Simon Gustavsson, and William D. Oliver. Superconducting qubits: Current state of play. *Annual Review of Condensed Matter Physics*, 11(1):369–395, 2020.

[2] E. D. Herbschleb, H. Kato, Y. Maruyama, T. Danjo, T. Makino, S. Yamasaki, I. Ohki, K. Hayashi, H. Morishita, M. Fujiwara, and N. Mizuochi. Ultra-long coherence times amongst room-temperature solid-state spins. *Nature Communications*, 10(1):3766, Aug 2019.

[3] Pengfei Wang, Chun-Yang Luan, Mu Qiao, Mark Um, Junhua Zhang, Ye Wang, Xiao Yuan, Mile Gu, Jingning Zhang, and Kihwan Kim. Single ion qubit with estimated coherence time exceeding one hour. *Nature Communications*, 12(1):233, Jan 2021.

[4] J. E. Austermann, J. A. Beall, S. A. Bryan, B. Dober, J. Gao, G. Hilton, J. Hubmayr, P. Mauskopf, C. M. McKenney, S. M. Simon, J. N. Ullom, M. R. Vissers, and G. W. Wilson. Millimeter-wave polarimeters using kinetic inductance detectors for toltec and beyond. *Journal of Low Temperature Physics*, 193(3):120–127, Nov 2018.

[5] McCarrick, H., Jones, G., Johnson, B. R., Abitbol, M. H., Ade, P. A. R., Bryan, S., Day, P., Essinger-Hileman, T., Flanigan, D., Leduc, H. G., Limon, M., Mauskopf, P., Miller, A., and Tucker, C. Design and performance of dual-polarization lumped-element kinetic inductance detectors for millimeter-wave polarimetry. *A&A*, 610:A45, 2018.

[6] S. Shu, M. Calvo, J. Goupy, S. Leclercq, A. Catalano, A. Bideaud, A. Monfardini, and E.F.C. Driessen. Understanding and minimizing resonance frequency deviations on a 4-inch kilo-pixel kinetic inductance detector array. working paper or preprint, June 2021.

[7] Matthew Reagor, Wolfgang Pfaff, Christopher Axline, Reinier W. Heeres, Nissim Ofek, Katrina Sliwa, Eric Holland, Chen Wang, Jacob Blumoff, Kevin Chou, Michael J. Hatridge, Luigi Frunzio, Michel H. Devoret, Liang Jiang, and Robert J. Schoelkopf. Quantum memory with millisecond coherence in circuit qed. *Phys. Rev. B*, 94:014506, Jul 2016.

[8] A Grassellino, A Romanenko, Y Trenikhina, M Checchin, M Martinello, O S Melnychuk, S Chandrasekaran, D A Sergatskov, S Posen, A C Crawford, S Aderhold, and D Bice. Unprecedented quality factors at accelerating gradients up to 45 MVm-1in niobium superconducting resonators via low temperature nitrogen infusion. *Superconductor Science and Technology*, 30(9):094004, aug 2017.

[9] Helin Zhang, Srivatsan Chakram, Tanay Roy, Nathan Earnest, Yao Lu, Ziwen Huang, D. K. Weiss, Jens Koch, and David I. Schuster. Universal fast-flux control of a coherent, low-frequency qubit. *Phys. Rev. X*, 11:011010, Jan 2021.

[10] Alexander P. M. Place, Lila V. H. Rodgers, Pranav Mundada, Basil M. Smitham, Mattias Fitzpatrick, Zhaoqi Leng, Anjali Premkumar, Jacob Bryon, Andrei Vrajitoarea, Sara Sussman, Guangming Cheng, Trisha Madhavan, Harshvardhan K. Babla, Xuan Hoang Le, Youqi Gang, Berthold Jäck, András Gyenis, Nan Yao, Robert J. Cava, Nathalie P. de Leon, and Andrew A. Houck. New material platform for superconducting transmon qubits with coherence times exceeding 0.3 milliseconds. *Nature Communications*, 12(1):1779, Mar 2021.

[11] Johannes Heinsoo, Christian Kraglund Andersen, Ants Remm, Sebastian Krinner, Theodore Walter, Yves Salathé, Simone Gasparinetti, Jean-Claude Besse, Anton Potočnik, Andreas Wallraff, and Christopher Eichler. Rapid high-fidelity multiplexed readout of superconducting qubits. *Phys. Rev. Applied*, 10:034040, Sep 2018.

[12] Sumedh Mahashabde, Ernst Otto, Domenico Montemurro, Sebastian de Graaf, Sergey Kubatkin, and Andrey Danilov. Fast tunable high-q-factor superconducting microwave resonators. *Phys. Rev. Applied*, 14:044040, Oct 2020.

[13] Luca Planat, Arpit Ranadive, Rémy Dassonneville, Javier Puertas Martínez, Sébastien Léger, Cécile Naud, Olivier Buisson, Wiebke Hasch-Guichard, Denis M. Basko, and Nicolas Roch. Photonic-crystal josephson traveling-wave parametric amplifier. *Phys. Rev. X*, 10:021021, Apr 2020.

[14] Samuel Goldstein, Naftali Kirsh, Elisha Svetitsky, Yuval Zamir, Ori Hachmo, Clovis Eduardo Mazzotti de Oliveira, and Nadav Katz. Four wave-mixing in a microstrip kinetic inductance travelling wave parametric amplifier. *Applied Physics Letters*, 116(15):152602, 2020.

[15] F. London, H. London, and Frederick Alexander Lindemann. The electromagnetic equations of the supraconductor. *Proceedings of the Royal Society of London. Series A - Mathematical and Physical Sciences*, 149(866):71–88, 1935.

[16] 73 - on the theory of superconductivity. In D. TER HAAR, editor, *Collected Papers of L.D. Landau*, pages 546–568. Pergamon, 1965.

[17] J. Bardeen, L. N. Cooper, and J. R. Schrieffer. Theory of superconductivity. *Phys. Rev.*, 108:1175–1204, Dec 1957.

[18] D. C. Mattis and J. Bardeen. Theory of the anomalous skin effect in normal and superconducting metals. *Phys. Rev.*, 111:412–417, Jul 1958.

[19] B.D. Josephson. Possible new effects in superconductive tunnelling. *Physics Letters*, 1(7):251–253, 1962.

[20] P. W. Anderson and J. M. Rowell. Probable observation of the josephson superconducting tunneling effect. *Phys. Rev. Lett.*, 10:230–232, Mar 1963.

[21] Y. Nakamura, Yu. A. Pashkin, and J. S. Tsai. Coherent control of macroscopic quantum states in a single-cooper-pair box. *Nature*, 398(6730):786–788, Apr 1999.

[22] K. B. Cooper, Matthias Steffen, R. McDermott, R. W. Simmonds, Seongshik Oh, D. A. Hite, D. P. Pappas, and John M. Martinis. Observation of quantum oscillations between a josephson phase qubit and a microscopic resonator using fast readout. *Phys. Rev. Lett.*, 93:180401, Oct 2004.

[23] J. Claudon, F. Balestro, F. W. J. Hekking, and O. Buisson. Coherent oscillations in a superconducting multilevel quantum system. *Phys. Rev. Lett.*, 93:187003, Oct 2004.

[24] Jens Koch, Terri M. Yu, Jay Gambetta, A. A. Houck, D. I. Schuster, J. Majer, Alexandre Blais, M. H. Devoret, S. M. Girvin, and R. J. Schoelkopf. Charge-insensitive qubit design derived from the cooper pair box. *Phys. Rev. A*, 76:042319, Oct 2007.

[25] J E Mooij and C J P M Harmans. Phase-slip flux qubits. *New Journal of Physics*, 7:219–219, oct 2005.

[26] Vladimir E. Manucharyan, Jens Koch, Leonid I. Glazman, and Michel H. Devoret. Fluxonium: Single cooper-pair circuit free of charge offsets. *Science*, 326(5949):113–116, 2009.

[27] F. Bloch. Nuclear induction. *Phys. Rev.*, 70:460–474, Oct 1946.

[28] A. Carrington and A. D. Mclachlan. *Introduction to magnetic resonance : with applications to chemistry and chemical physics*. Chapman and Hall, London, 1967.

[29] A. O. Caldeira and A. J. Leggett. Influence of dissipation on quantum tunneling in macroscopic systems. *Phys. Rev. Lett.*, 46:211–214, Jan 1981.

[30] Herbert B. Callen and Theodore A. Welton. Irreversibility and generalized noise. *Phys. Rev.*, 83:34–40, Jul 1951.

[31] David J. Griffiths and Darrell F. Schroeter. *Time-Independent Schrödinger Equation*, page 25–90. Cambridge University Press, 3 edition, 2018.

[32] Salman Shahid, J. Ball, C. G. Wells, and P. Wen. Reflection type q-factor measurement using standard least squares methods. *Iet Microwaves Antennas & Propagation*, 5:426–432, 2011.

[33] S. Probst, F. B. Song, P. A. Bushev, A. V. Ustinov, and M. Weides. Efficient and robust analysis of complex scattering data under noise in microwave resonators. *Review of Scientific Instruments*, 86(2):024706, 2015.

[34] Sergey Belomestnykh. *Superconducting Radio-Frequency Systems for High-ß Particle Accelerators*, pages 147–184.

[35] Michael Tinkham. *Introduction to Superconductivity*. Dover Publications, 2 edition, June 2004.

[36] Jonathan Burnett, Andreas Bengtsson, David Niepce, and Jonas Bylander. Noise and loss of superconducting aluminium resonators at single photon energies. *Journal of Physics: Conference Series*, 969:012131, mar 2018.

[37] N. Maleeva, L. Grünhaupt, T. Klein, F. Levy-Bertrand, O. Dupre, M. Calvo, F. Valenti, P. Winkel, F. Friedrich, W. Wernsdorfer, A. V. Ustinov, H. Rotzinger, A. Monfardini, M. V. Fistul, and I. M. Pop. Circuit quantum electrodynamics of granular aluminum resonators. *Nature Communications*, 9(1):3889, Sep 2018.

[38] Faustin W. Carter, Trupti Khaire, Clarence Chang, and Valentyn Novosad. Low-loss single-photon nbn microwave resonators on si. *Applied Physics Letters*, 115(9):092602, 2019.

[39] A. Bruno, G. de Lange, S. Asaad, K. L. van der Enden, N. K. Langford, and L. DiCarlo. Reducing intrinsic loss in superconducting resonators by surface treatment and deep etching of silicon substrates. *Applied Physics Letters*, 106(18):182601, 2015.

[40] P. M. Tedrow, G. Faraci, and R. Meservey. Measurement of the surface inductance and penetration depth of superconducting aluminum. *Phys. Rev. B*, 4:74–82, Jul 1971.

[41] B. L. Brandt, R. D. Parks, and R. D. Chaudhari. Intermediate state of thin superconductors. *Journal of Low Temperature Physics*, 4(1):41–63, Jan 1971.

[42] R G Chambers. The kinetic formulation of conduction problems. *Proceedings of the Physical Society. Section A*, 65(6):458–459, jun 1952.

[43] R. Pöpel. Surface impedance and reflectivity of superconductors. *Journal of Applied Physics*, 66(12):5950–5957, 1989.

[44] Jiansong Gao. The physics of superconducting microwave resonators. 2008.

[45] R. E. Glover and M. Tinkham. Conductivity of superconducting films for photon energies between 0.3 and $40kT_c$. *Phys. Rev.*, 108:243–256, Oct 1957.

[46] A. B. Pippard and William Lawrence Bragg. The surface impedance of superconductors and normal metals at high frequencies i. resistance of superconducting tin and mercury at 1200 mcyc. /sec. *Proceedings of the Royal Society of London. Series A. Mathematical and Physical Sciences*, 191(1026):370–384, 1947.

[47] Alfred Brian Pippard and William Lawrence Bragg. An experimental and theoretical study of the relation between magnetic field and current in a superconductor. *Proceedings of the Royal Society of London. Series A. Mathematical and Physical Sciences*, 216(1127):547–568, 1953.

[48] G. E. H. REUTER and E. H. SONDHEIMER. Theory of the anomalous skin effect in metals. *Nature*, 161(4089):394–395, Mar 1948.

[49] Nicola Pompeo, Kostiantyn Torokhtii, and Enrico Silva. Surface impedance measurements in thin conducting films: Substrate and finite-thickness-induced uncertainties. In *2017 IEEE International Instrumentation and Measurement Technology Conference (I2MTC)*, pages 1–5, 2017.

[50] Richard E. Matick. *Superconducting Transmission Lines*, pages 211–267. 1995.

[51] V.B. Braginsky, M.L. Gorodetsky, and V.S. Ilchenko. Quality-factor and nonlinear properties of optical whispering-gallery modes. *Physics Letters A*, 137(7):393–397, 1989.

[52] Clemens Müller, Jared H Cole, and Jürgen Lisenfeld. Towards understanding two-level-systems in amorphous solids: insights from quantum circuits. *Reports on Progress in Physics*, 82(12):124501, oct 2019.

[53] David P. Pappas, Michael R. Vissers, David S. Wisbey, Jeffrey S. Kline, and Jiansong Gao. Two level system loss in superconducting microwave resonators. *IEEE Transactions on Applied Superconductivity*, 21(3):871–874, 2011.

[54] Jeremy M. Sage, Vladimir Bolkhovsky, William D. Oliver, Benjamin Turek, and Paul B. Welander. Study of loss in superconducting coplanar waveguide resonators. *Journal of Applied Physics*, 109(6):063915, 2011.

[55] Alex Gurevich. Superconducting radio-frequency fundamentals for particle accelerators. *Reviews of Accelerator Science and Technology*, 05:119–146, 2012.

[56] R. C. Dynes, V. Narayanamurti, and J. P. Garno. Direct measurement of quasiparticle-lifetime broadening in a strong-coupled superconductor. *Phys. Rev. Lett.*, 41:1509–1512, Nov 1978.

[57] Božidar Mitrović and Lee A Rozema. On the correct formula for the lifetime broadened superconducting density of states. *Journal of Physics: Condensed Matter*, 20(1):015215, dec 2007.

[58] Takashi Noguchi, Masato Naruse, Masakazu Sekine, Kenichi Karatsu, and Yutaro Sekimoto. Effect of quasiparticles in the intragap states on the superconducting surface resistance. *IEEE Transactions on Applied Superconductivity*, 26(3):1–4, 2016.

[59] S. E. de Graaf, L. Faoro, L. B. Ioffe, S. Mahashabde, J. J. Burnett, T. Lindström, S. E. Kubatkin, A. V. Danilov, and A. Ya. Tzalenchuk. Two-level systems in superconducting quantum devices due to trapped quasiparticles. *Science Advances*, 6(51), 2020.

[60] L. Cardani, F. Valenti, N. Casali, G. Catelani, T. Charpentier, M. Clemenza, I. Colantoni, A. Cruciani, G. D'Imperio, L. Gironi, L. Grünhaupt, D. Gusenkova, F. Henriques, M. Lagoin, M. Martinez, G. Pettinari, C. Rusconi, O. Sander, C. Tomei, A. V. Ustinov, M. Weber, W. Wernsdorfer, M. Vignati, S. Pirro, and I. M. Pop. Reducing the impact of radioactivity on quantum circuits in a deep-underground facility. *Nature Communications*, 12(1):2733, May 2021.

[61] Hasan S. Padamsee. Superconducting radio-frequency cavities. *Annual Review of Nuclear and Particle Science*, 64(1):175–196, 2014.

[62] A. Romanenko and A. Grassellino. Dependence of the microwave surface resistance of superconducting niobium on the magnitude of the rf field. *Applied Physics Letters*, 102(25):252603, 2013.

[63] Sydeny Chapman and T. G. Cowling. *The mathematical theory of non-uniform gases. an account of the kinetic theory of viscosity, thermal conduction and diffusion in gases*. 1970.

[64] Daniel Gall. Electron mean free path in elemental metals. *Journal of Applied Physics*, 119(8):085101, 2016.

[65] E. P. Harris and D. E. Mapother. Critical field of superconducting aluminum as a function of pressure and temperature above 0.3k. *Phys. Rev.*, 165:522–532, Jan 1968.

[66] Charles Kittel. *Introduction to Solid State Physics*. Wiley, 8 edition, 2004.

[67] M. David Maloney, Francisco de la Cruz, and Manuel Cardona. Superconducting parameters and size effects of aluminum films and foils. *Phys. Rev. B*, 5:3558–3572, May 1972.

[68] Lukas Grünhaupt, Uwe von Lüpke, Daria Gusenkova, Sebastian T. Skacel, Nataliya Maleeva, Steffen Schlör, Alexander Bilmes, Hannes Rotzinger, Alexey V. Ustinov, Martin Weides, and Ioan M. Pop. An argon ion beam milling process for native alox layers enabling coherent superconducting contacts. *Applied Physics Letters*, 111(7):072601, 2017.

[69] G. K. White. The thermal and electrical conductivity of copper at low temperatures. *Australian Journal of Physics*, 6(4):397–404, 1953.

[70] P. W. ANDERSON and Y. B. KIM. Hard superconductivity: Theory of the motion of abrikosov flux lines. *Rev. Mod. Phys.*, 36:39–43, Jan 1964.

[71] C. Song, T. W. Heitmann, M. P. DeFeo, K. Yu, R. McDermott, M. Neeley, John M. Martinis, and B. L. T. Plourde. Microwave response of vortices in superconducting thin films of re and al. *Phys. Rev. B*, 79:174512, May 2009.

[72] M. Kudra, J. Biznárová, A. Fadavi Roudsari, J. J. Burnett, D. Niepce, S. Gasparinetti, B. Wickman, and P. Delsing. High quality three-dimensional aluminum microwave cavities. *Applied Physics Letters*, 117(7):070601, 2020.

[73] A Grassellino, A Romanenko, D Sergatskov, O Melnychuk, Y Trenikhina, A Crawford, A Rowe, M Wong, T Khabiboulline, and F Barkov. Nitrogen and argon doping of niobium for superconducting radio frequency cavities: a pathway to highly efficient accelerating structures. *Superconductor Science and Technology*, 26(10):102001, aug 2013.

[74] M. Bertucci, A. Bignami, A. Bosotti, P. Michelato, L. Monaco, C. Pagani, R. Paparella, D. Sertore, C. Maiano, P. Pierini, and J. Chen. Performance analysis of the european x-ray free electron laser 3.9 ghz superconducting cavities. *Phys. Rev. Accel. Beams*, 22:082002, Aug 2019.

[75] P. J. de Visser, D. J. Goldie, P. Diener, S. Withington, J. J. A. Baselmans, and T. M. Klapwijk. Evidence of a nonequilibrium distribution of quasiparticles in the

microwave response of a superconducting aluminum resonator. *Phys. Rev. Lett.*, 112:047004, Jan 2014.

[76] W. Woods, G. Calusine, A. Melville, A. Sevi, E. Golden, D.K. Kim, D. Rosenberg, J.L. Yoder, and W.D. Oliver. Determining interface dielectric losses in superconducting coplanar-waveguide resonators. *Phys. Rev. Applied*, 12:014012, Jul 2019.

[77] C. Wang, C. Axline, Y. Y. Gao, T. Brecht, Y. Chu, L. Frunzio, M. H. Devoret, and R. J. Schoelkopf. Surface participation and dielectric loss in superconducting qubits. *Applied Physics Letters*, 107(16):162601, 2015.

[78] M. H. Devoret. *Quantum fluctuations in electrical circuits.* Edition de Physique, France, 1997.

[79] Ramamurti Shankar. *Principles of quantum mechanics.* Plenum, New York, NY, 1980.

[80] I. S. Gradshteyn and I. M. Ryzhik. *Table of Integrals, Series, and Products.* 2007.

[81] Joydip Ghosh, Austin G. Fowler, John M. Martinis, and Michael R. Geller. Understanding the effects of leakage in superconducting quantum-error-detection circuits. *Phys. Rev. A*, 88:062329, Dec 2013.

[82] Lukas Grünhaupt, Martin Spiecker, Daria Gusenkova, Nataliya Maleeva, Sebastian T. Skacel, Ivan Takmakov, Francesco Valenti, Patrick Winkel, Hannes Rotzinger, Wolfgang Wernsdorfer, Alexey V. Ustinov, and Ioan M. Pop. Granular aluminium as a superconducting material for high-impedance quantum circuits. *Nature Materials*, 18(8):816–819, Aug 2019.

[83] David Niepce, Jonathan Burnett, and Jonas Bylander. High kinetic inductance NbN nanowire superinductors. *Phys. Rev. Applied*, 11:044014, Apr 2019.

[84] A. Belkin, M. Belkin, V. Vakaryuk, S. Khlebnikov, and A. Bezryadin. Formation of quantum phase slip pairs in superconducting nanowires. *Phys. Rev. X*, 5:021023, Jun 2015.

[85] Jan Nicolas Voss, Yannick Schön, Micha Wildermuth, Dominik Dorer, Jared H. Cole, Hannes Rotzinger, and Alexey V. Ustinov. Eliminating quantum phase slips in superconducting nanowires. *ACS Nano*, 0(0):null, 0. PMID: 33596045.

[86] Vladimir E. Manucharyan, Nicholas A. Masluk, Archana Kamal, Jens Koch, Leonid I. Glazman, and Michel H. Devoret. Evidence for coherent quantum phase slips across a josephson junction array. *Phys. Rev. B*, 85:024521, Jan 2012.

[87] Carsten Hutter, Erik A. Tholén, Kai Stannigel, Jack Lidmar, and David B. Haviland. Josephson junction transmission lines as tunable artificial crystals. *Phys. Rev. B*, 83:014511, Jan 2011.

[88] Javier Puertas. *Probing light-matter interaction in the many-body regime of superconducting quantum circuits*. Theses, Université Grenoble Alpes, June 2018.

[89] Ioan Mihai Pop. *Sauts quantiques de phase dans des chaînes de jonctions Josephson*. Theses, Université de Grenoble, February 2011.

[90] Yu Chen, Yen-Hsiang Lin, Stephen D. Snyder, Allen M. Goldman, and Alex Kamenev. Dissipative superconducting state of non-equilibrium nanowires. *Nature Physics*, 10(8):567–571, Aug 2014.

[91] H. P. Büchler, V. B. Geshkenbein, and G. Blatter. Quantum fluctuations in thin superconducting wires of finite length. *Phys. Rev. Lett.*, 92:067007, Feb 2004.

[92] K. K. Likharev and A. B. Zorin. Theory of the bloch-wave oscillations in small josephson junctions. *Journal of Low Temperature Physics*, 59(3):347–382, May 1985.

[93] W. Guichard and F. W. J. Hekking. Phase-charge duality in josephson junction circuits: Role of inertia and effect of microwave irradiation. *Phys. Rev. B*, 81:064508, Feb 2010.

[94] Long B. Nguyen, Yen-Hsiang Lin, Aaron Somoroff, Raymond Mencia, Nicholas Grabon, and Vladimir E. Manucharyan. High-coherence fluxonium qubit. *Phys. Rev. X*, 9:041041, Nov 2019.

[95] Etienne Dumur. *A V-shape superconducting artificial atom for circuit quantum electrodynamics*. PhD thesis, 2015. Thèse de doctorat dirigée par Buisson, Olivier Physique de la matière condensée et du rayonnement Université Grenoble Alpes (ComUE) 2015.

[96] G. J. Dolan. Offset masks for lift-off photoprocessing. *Applied Physics Letters*, 31(5):337–339, 1977.

[97] Florent Lecocq, Ioan M Pop, Zhihui Peng, Iulian Matei, Thierry Crozes, Thierry Fournier, Cécile Naud, Wiebke Guichard, and Olivier Buisson. Junction fabrication by shadow evaporation without a suspended bridge. *Nanotechnology*, 22(31):315302, jul 2011.

[98] Vinay Ambegaokar and Alexis Baratoff. Tunneling between superconductors. *Phys. Rev. Lett.*, 10:486–489, Jun 1963.

[99] Maxime Boissonneault, J. M. Gambetta, and Alexandre Blais. Dispersive regime of circuit qed: Photon-dependent qubit dephasing and relaxation rates. *Phys. Rev. A*, 79:013819, Jan 2009.

[100] David M. Pozar. *Microwave engineering.* Fourth edition. Hoboken, NJ : Wiley,©2012, [2012].

[101] Terman Frederick Emmons. *Radio engineers' handbook / by Frederick Emmons Terman,...* McGraw-Hill handbooks. McGraw-Hill, New York London, 1943, cp. 1943.

[102] I. I. Rabi. Space quantization in a gyrating magnetic field. *Phys. Rev.*, 51:652–654, Apr 1937.

[103] I. Chiorescu, P. Bertet, K. Semba, Y. Nakamura, C. J. P. M. Harmans, and J. E. Mooij. Coherent dynamics of a flux qubit coupled to a harmonic oscillator. *Nature*, 431(7005):159–162, Sep 2004.

[104] Norman F. Ramsey. A molecular beam resonance method with separated oscillating fields. *Phys. Rev.*, 78:695–699, Jun 1950.

[105] E. L. Hahn. Spin echoes. *Phys. Rev.*, 80:580–594, Nov 1950.

[106] N. Bar-Gill, L. M. Pham, A. Jarmola, D. Budker, and R. L. Walsworth. Solid-state electronic spin coherence time approaching one second. *Nature Communications*, 4(1):1743, Apr 2013.

[107] Purcell E.M. Spontaneous emission probabilities at radio frequencies. *Phys. Rev.*, 69:681, Jun 1946.

[108] K. Gupta, R. Garg, and I. Bahl. Microstrip lines and slotlines. 1979.

[109] Ioan M. Pop, Kurtis Geerlings, Gianluigi Catelani, Robert J. Schoelkopf, Leonid I. Glazman, and Michel H. Devoret. Coherent suppression of electromagnetic dissipation due to superconducting quasiparticles. *Nature*, 508(7496):369–372, Apr 2014.

[110] G. Catelani, J. Koch, L. Frunzio, R. J. Schoelkopf, M. H. Devoret, and L. I. Glazman. Quasiparticle relaxation of superconducting qubits in the presence of flux. *Phys. Rev. Lett.*, 106:077002, Feb 2011.

[111] Oliver Dial, Douglas T McClure, Stefano Poletto, G A Keefe, Mary Beth Rothwell, Jay M Gambetta, David W Abraham, Jerry M Chow, and Matthias Steffen. Bulk and surface loss in superconducting transmon qubits. *Superconductor Science and Technology*, 29(4):044001, mar 2016.

[112] S. Yanai and G. Steele. Observation of enhanced coherence in josephson squid cavities using a hybrid fabrication approach. *arXiv: Superconductivity*, 2019.

[113] W. Oliver and P. Welander. Materials in superconducting quantum bits. *Mrs Bulletin*, 38:816–825, 2013.

[114] Jonas Bylander, Simon Gustavsson, Fei Yan, Fumiki Yoshihara, Khalil Harrabi, George Fitch, David G. Cory, Yasunobu Nakamura, Jaw-Shen Tsai, and William D. Oliver. Noise spectroscopy through dynamical decoupling with a superconducting flux qubit. *Nature Physics*, 7(7):565–570, Jul 2011.

[115] G. Ithier, E. Collin, P. Joyez, P. J. Meeson, D. Vion, D. Esteve, F. Chiarello, A. Shnirman, Y. Makhlin, J. Schriefl, and G. Schön. Decoherence in a superconducting quantum bit circuit. *Phys. Rev. B*, 72:134519, Oct 2005.

[116] H. Y. Carr and E. M. Purcell. Effects of diffusion on free precession in nuclear magnetic resonance experiments. *Phys. Rev.*, 94:630–638, May 1954.

[117] S. Meiboom and D. Gill. Modified spin-echo method for measuring nuclear relaxation times. *Review of Scientific Instruments*, 29:688–691, 1958.

[118] Roger H. Koch, David P. DiVincenzo, and John Clarke. Model for $1/f$ flux noise in squids and qubits. *Phys. Rev. Lett.*, 98:267003, Jun 2007.

[119] S. E. de Graaf, A. A. Adamyan, T. Lindström, D. Erts, S. E. Kubatkin, A. Ya. Tzalenchuk, and A. V. Danilov. Direct identification of dilute surface spins on al_2o_3: Origin of flux noise in quantum circuits. *Phys. Rev. Lett.*, 118:057703, Jan 2017.

[120] F. Yoshihara, K. Harrabi, A. O. Niskanen, Y. Nakamura, and J. S. Tsai. Decoherence of flux qubits due to $1/f$ flux noise. *Phys. Rev. Lett.*, 97:167001, Oct 2006.

[121] C. Granata, A. Vettoliere, R. Russo, M. Russo, and B. Ruggiero. Critical current noise investigations in underdamped josephson devices. *Phys. Rev. B*, 83:092504, Mar 2011.

[122] Fei Yan, Dan Campbell, Philip Krantz, Morten Kjaergaard, David Kim, Jonilyn L. Yoder, David Hover, Adam Sears, Andrew J. Kerman, Terry P. Orlando, Simon Gustavsson, and William D. Oliver. Distinguishing coherent and thermal photon noise in a circuit quantum electrodynamical system. *Phys. Rev. Lett.*, 120:260504, Jun 2018.

[123] Nicholas Adam Masluk. *Reducing the losses of the fluxonium artificial atom.* PhD thesis, Yale University, January 2013.

[124] P. Kumar, S. Sendelbach, M. A. Beck, J. W. Freeland, Zhe Wang, Hui Wang, Clare C. Yu, R. Q. Wu, D. P. Pappas, and R. McDermott. Origin and reduction of $1/f$ magnetic flux noise in superconducting devices. *Phys. Rev. Applied*, 6:041001, Oct 2016.

[125] Pranav S. Mundada, András Gyenis, Ziwen Huang, Jens Koch, and Andrew A. Houck. Floquet-engineered enhancement of coherence times in a driven fluxonium qubit. *Phys. Rev. Applied*, 14:054033, Nov 2020.